Dissertation
submitted to the
Combined Faculties for the Natural Sciences and for Mathematics
of the Ruperto-Carola University of Heidelberg, Germany
for the degree of
Doctor of Natural Sciences

Put forward by

Dipl.Phys. Matteo Bocchi

born in Biella, Italy

oral examination: 27.5.2009

Magnetohydrodynamic instabilities of astrophysical jets

Referees:

Prof. Dr. Max Camenzind

Dr. Hubert Baty

Zusammenfassung:

Die bemerkenswerte Stabilität, die in astrophysikalischen Jets beobachtet wird, ist noch nicht endgültig verstanden und bedarf weiterer Erforschung. Um die Auswirkungen einer antiparallelen Magnetfeldtopologie auf die lineare Phase sowie die nicht-lineare Entwicklung der Kelvin-Helmholtz-Instabilität zu untersuchen, haben wir direkte numerische Simulationen durchgeführt, die die Gleichungen der idealen Magnetohydrodynamik für verschiedene Anfangsbedingungen lösen. In einzelnen Scherflächen zeigte die Instabilität höhere Wachstumsraten als im homogenen (parallelen) Fall und eine Oszillation mit einem typischen Wellenvektor $Ka \simeq 0.4$. Wirbelartige Strukturen wurden für Alfvén-Machzahlen $M_a > 2$ beobachtet. Das Vorhandensein von isolierten magnetischen Inseln, die durch die KH-Instabilität entstehen, behindert die Verstärkung der Magnetfelder im Umkreis der KH-Wirbel und dadurch auch die magnetische Sättigungsenergie verglichen mit dem homogenen Fall. Die Simulationen mit größerem Integrationsbereich zeigten eine inverse Energiekaskade zu größeren Strukturen, die turbulenter sind als im homogenen Fall. Die niedrigere magnetische Verstärkung wegen der isolierten Inseln verringerten den Schwelle für die drei-dimensionale (3D) Reorganisation zu einem laminaren Fluss von $M_a \lesssim 50$ (homogen) zu $M_a \lesssim 20$ (antiparallel). Zwei-dimensionale (2D) Großsimulationen des Jet-Querschnittes zeigten episodische Unterbrechungen und Wiederherstellung des Flusses durch einen magnetischen Verstärkungsprozess, dessen Existenz vorher nur in subsonischen Flüssen angenommen wurde. Diese Ergebnis ist für homogene und antiparallele Magnetfelder gültig, was durch 3D-Simulationen bestätigt wurde.

Abstract:

The remarkable stability of astrophysical jets is not yet fully understood and requires further investigation. In order to study the effects of an antiparallel magnetic field topology on the linear stage and non-linear evolution of the Kelvin Helmholtz (KH) instability, we performed direct numerical simulations to solve the ideal magnetohydrodynamic equations in a variety of initial configurations. Single shear layers presented growth rates of the instability higher than in the uniform (parallel) case, and a typical oscillation wave vector $Ka \simeq 0.4$. Vortical motions were observed for Alfvén Mach numbers $M_a > 2$. The presence of tearing type magnetic islands, driven by the KH instability, reduced the magnetic field enhancement around the perimeter of the KH vortices proper of the KH instability and, subsequently, reduced the value of the magnetic saturation energy as compared to the uniform field case. The extended domain simulations showed an inverse cascade to bigger scales, more turbulent than in the uniform case. The lower magnetic amplification, due to the islands, moved the threshold for three-dimensional (3D) reorganization to a laminar flow from $M_a \lesssim 50$ (uniform) to $M_a \lesssim 20$ (antiparallel). Two-dimensional (2D) spatial slab-jet simulations showed episodic disruption and revival of the flow due to a magnetic field amplification process, previously believed to be present only in subsonic flows. This result, retrieved also in 3D simulations, is the same for uniform and antiparallel magnetic fields.

Contents

Preface

The night sky has always fascinated me. Not only because of the stars, blinking like diamonds on the darkest velvet, but also for the details that a patient observer can notice: the phases of the moon, the milky way, the occasional falling star. The sky holds a lot of surprises as well. The use of telescopes reveals a huge variety of celestial bodies, impossible to perceive with human eyes only. And not just because they appear too tiny or faint, but also because they are visible in wavelengths of the light spectrum precluded to our wonderful, but limited, sight. And so we discover planets, stars of different colors and sizes, clouds of gas with a variety of shapes, galaxies and quasars. The universe slowly unveils itself before our eyes as uniquely beautiful.

On my side, such a variety stimulates my natural curiosity and led me to scientific studies. This path is characterized by analytic thinking and rigorous investigation of all the small details and pieces of evidence to reach the ultimate goal of understanding. How is it possible? How does it work? What am I really seeing through this ingenious system of lenses? Some may say that studying the sky in such detail, rips it off its beauty. As I agree that knowledge does not directly contribute to the beauty of the sky, I think it adds to the sense of size and greatness I feel when looking up at the stars. In one blink I am reminded of our tiny size in the universe, of the limits of our knowledge but at the same time of the incredible level of comprehension human beings have achieved. Yet, there are several aspects of our beloved home-universe that we do not understand. Among the various objects in the sky, a group strikes me for the puzzles it sill poses to astronomers and physicists: astrophysical jets. This work is about them and their understanding.

Chapter 1

Introduction

This chapter is meant to give an overview of jets, our uncertainties about the models, and their origin. We will focus also on the problem of jet stability, the central topic of this thesis, and we will introduce the numerical calculations we performed to carry out our study.

1.1 Jets

Astrophysical jets are believed to be powerful outflows generated by an amazing variety of objects, from protostars to radio galaxies and quasars. These filament-like structures appear to have similar characteristics, like high degree of collimation, length that greatly exceeds the dimensions of the source object and supersonic speeds. The material of the jet is propelled through an external medium, and the subsequent interaction is responsible for the production of shock waves and energy exchange between beam and ambient. The properties of the central source, and consequently of the ambient medium, affect heavily the characteristics of the jets, so it is useful to classify them in two broad categories: jets from young stars, and extragalactic jets.

1.2 Jets from young stars

First of all, a clarification about terminology. By young stars we mean protostars in the process of forming, so objects that have not yet reached the main sequence on the Hertzsprung-Russell(HR) diagram. We will also refer to them as Young Stellar Objects (YSOs). The fact that YSOs are relatively close to the Earth, together with the high number of stars in our galaxy, allows astronomers to observe YSOs and star forming regions in a variety of environments and at different evolutionary stages. It is useful therefore to give an overview on star formation. The observations of star forming regions have revealed the presence of small nebulae characterized by an emission line spectrum, called Herbig-Haro (HH) objects by the name of the first astronomers who discovered them: Herbig (1950, 1951), and Haro (1952, 1953). Today HH objects are recognized as the optical signature of collimated outflows emanating from young stars (Dopita et al., 1982, Mundt & Fried, 1983 and subsequent papers. See review by Reipurth & Bally, 2001). Following Reipurth & Bally (2001), we will describe these objects and the properties of related outflows.

1.2.1 Star formation and protostar classification

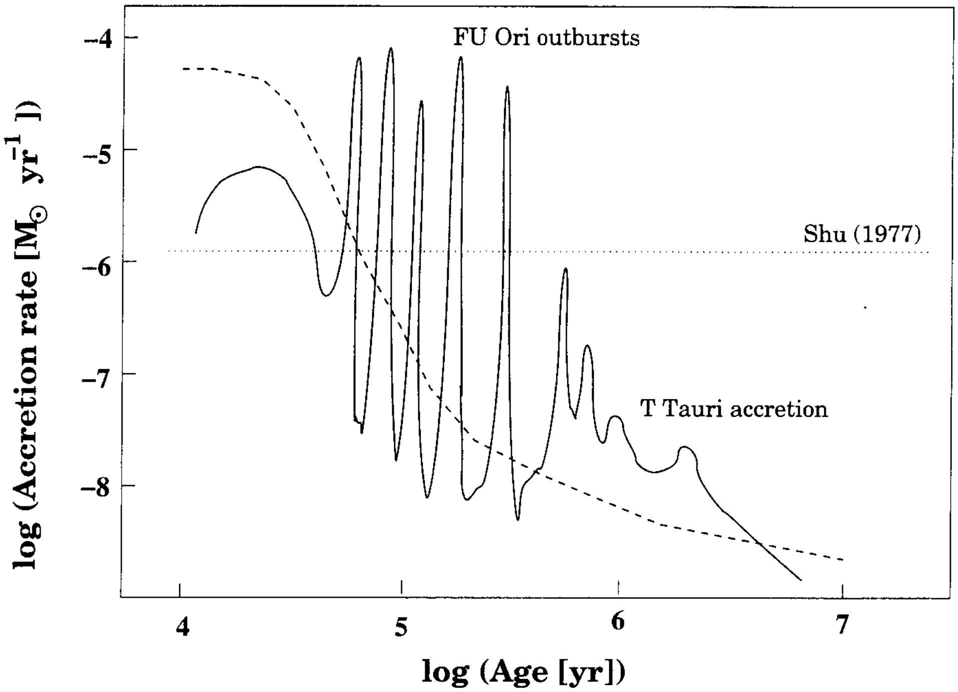

Figure 1.1. Schematic evolution in time of accretion rates as calculated with models and in relation to observed phenomena. *Dotted line*: Constant accretion rate, from the model by Shu (1977). *Dashed line*: adaptation of results from various more realistic models. *Solid line*: Accretion rate adapted from Hartmann (2000), taking into account outbursts of FU Ori type protostars and T Tauri disk accretion. Diagram take from Schulz (2005).

The process of star formation takes place in the interstellar medium (ISM) of a galaxy. Indeed, diffuse gas and dust fill in the volume between stars in spiral galaxies. The composition of the ISM is dominated by hydrogen (roughly 70%), and helium (basically all the rest). Traces of heavier elements, called generally metals, are present and important, but they account for less than 1% of the mass. In the ISM particular structures are found: molecular clouds. It is here that stars are born.

By far the most common molecule in the clouds is H_2. The biggest molecular clouds, called giant molecular clouds, have a diameter of roughly 100 light years, density of 100 particles per cubic centimeter and masses up to 10^6 $M_\odot$. If the cloud has sufficient mass, the gas pressure is not enough to sustain it and the cloud starts a gravitational collapse. This is possible if the

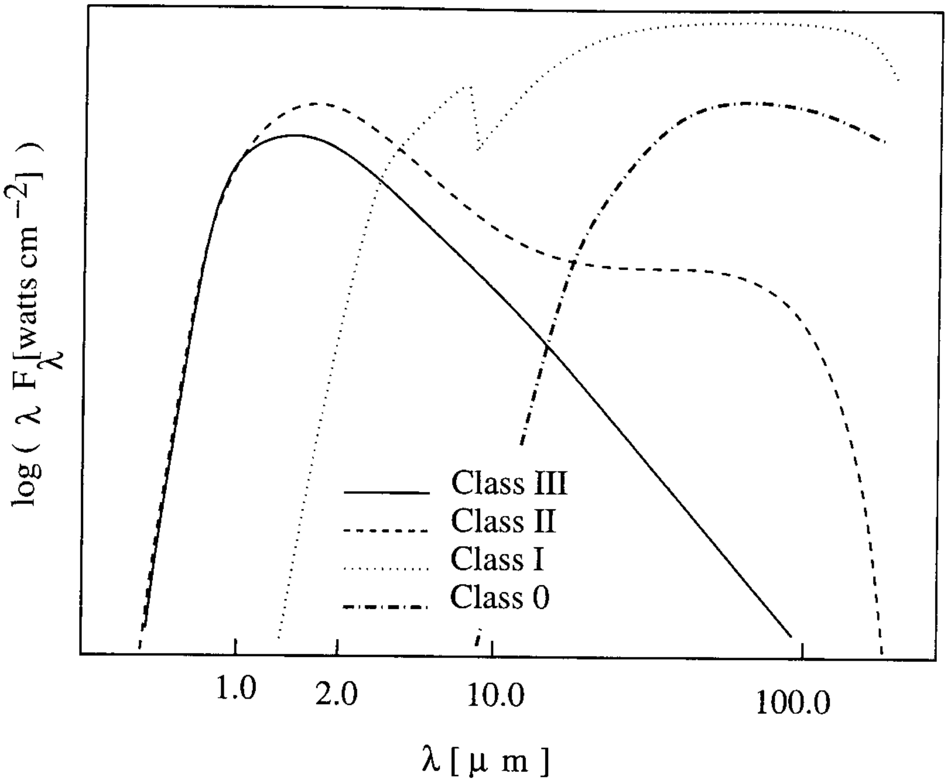

Figure 1.2. Proposed classification of Pre main sequence stars based on the spectral energy distribution in the range 1 − 100 μm. Taken from Schulz (2005).

mass of the cloud is bigger than the Jeans mass:

$$M_j = \left(\frac{4\pi}{3}\right)\rho\left(\frac{R_j}{2}\right)^3 = \left(\frac{\pi}{6}\right)\frac{c_s^3}{G^{3/2}\rho^{1/2}} \simeq (2M_\odot)\left(\frac{c_s}{0.2\ \mathrm{Kms}^{-1}}\right)^3\left(\frac{n}{10^3\ \mathrm{cm}^{-3}}\right)^{-1/2}, \quad (1.1)$$

where $R_j = c_s/\sqrt{G\rho}$ is the Jeans radius, c_s is the sound speed, ρ is the density and n is the number density. The collapse can be triggered by external events which compress the giant cloud. First, clouds can collide with each other. Second, supernova explosions produce shock waves affecting the surrounding medium. Finally, galaxy collision/merging causes starburst phenomena, since all the gas in the galaxies is then subject to tidal forces. A collapsing giant cloud usually fragments in smaller clouds, big clumps and finally small molecular cloud cores.

Typically these cores have masses of order $1M_\odot$, radius of ≈ 0.1 pc, temperature of 10 K, mean density 10^{-19} g cm^{-3} and ionization fraction $\approx 10^{-7}$. Note that this kind of cloud cores will form a low mass star, but bigger cores exists, with up to 50 $M_\odot$ over a radius of ≈ 0.3 pc. These objects are unstable against gravitational collapse. As long as the inner temperature is of the order of the external one, the energy gained by compression is radiated away by dust particles, so it cannot contribute to the pressure. As a consequence, the collapse takes place on a free fall time scale. One of the first models in spherical symmetry, with a profile for the

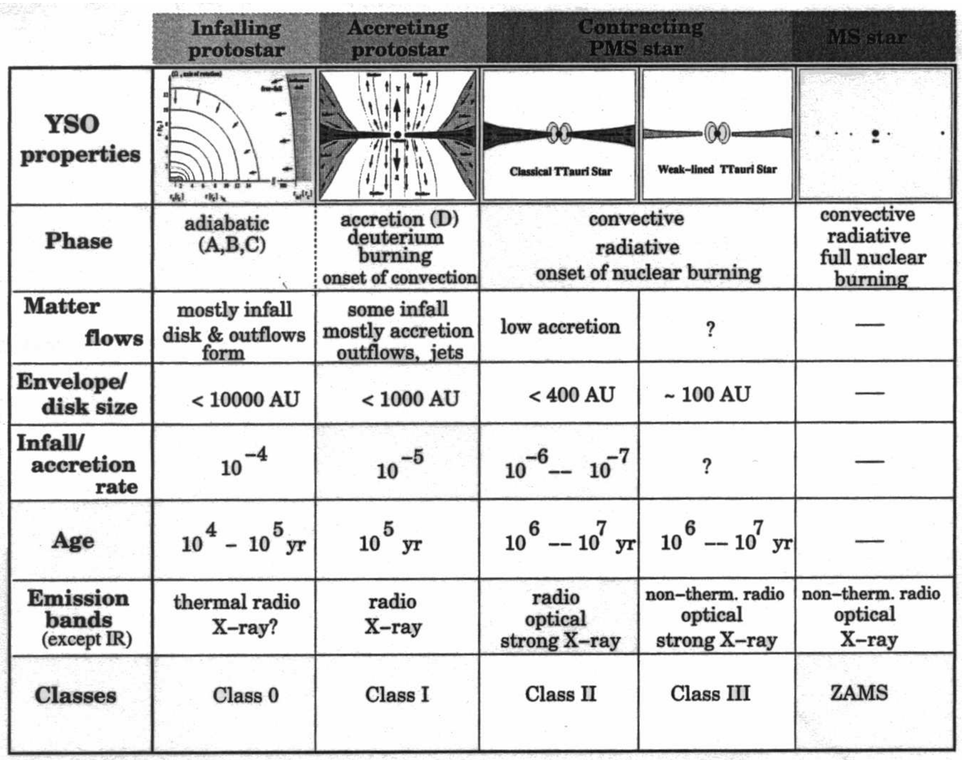

	Infalling protostar	Accreting protostar	Contracting PMS star		MS star
YSO properties			Classical TTauri Star	Weak-lined TTauri Star	
Phase	adiabatic (A,B,C)	accretion (D) deuterium burning onset of convection	convective radiative onset of nuclear burning		convective radiative full nuclear burning
Matter flows	mostly infall disk & outflows form	some infall mostly accretion outflows, jets	low accretion	?	—
Envelope/ disk size	< 10000 AU	< 1000 AU	< 400 AU	~ 100 AU	—
Infall/ accretion rate	10^{-4}	10^{-5}	10^{-6} -- 10^{-7}	?	—
Age	10^{4} - 10^{5} yr	10^{5} yr	10^{6} -- 10^{7} yr	10^{6} -- 10^{7} yr	—
Emission bands (except IR)	thermal radio X-ray?	radio X-ray	radio optical strong X-ray	non-therm. radio optical strong X-ray	non-therm. radio optical X-ray
Classes	Class 0	Class I	Class II	Class III	ZAMS

Figure 1.3. Summary of protostar classification in the framework of evolutionary interpretation. Taken from Schulz (2005).

density proportional to r^{-2}, was developed by Shu (1977), which introduced the concept of "inside-out collapse". It happens, in fact, that the inner part of the core collapses much faster than the outer part. As a consequence, the outer parts start collapsing only when reached by an expansion wave propagating outwards at sound speed.

Since then, several new models have been developed. In the collapse coming before the formation of a proper protostar, four different phases have been recognized:

A) *Free-fall phase* The collapse is fairly isothermal and proceeds on a free fall time scale. The central density rises faster than in the outer part. Cooling is done by hydrogen molecules and dust grains. Unless the temperature rises above 200 K, most hydrogen molecules are still in the rotational ground state.

B) *First core phase* Once the central density reaches 10^{-13} g cm^{-3}, some layers of the core become optically thick. Therefore radiation cannot escape and the collapse is not isothermal anymore. Internal temperature and pressure increases. Reaching 1000 K, most dust grains evaporates and hydrogen molecules are in the vibrational and rotational excited states.

C) *Opacity phase* At temperature higher than 2000 K, hydrogen molecules start to dissociate.

The adiabatic exponent Γ drops below 4/3, which is the critical value for stability. This means that the internal pressure gradient is not steep enough to balance the gravitational force. A new collapse takes place, until density reaches the value 10^{-2} g cm^{-3}. In these conditions the ionization fraction is sufficient to bring back the adiabatic exponent above 4/3. As the temperature increases, Helium and higher Z species become ionized. Each time, the adiabatic exponent drops below the critical value and a new contraction takes place. The core now has reached ≈ 0.01 M$_\odot$.

D) *Accretion phase* The core becomes optically thick and accretion starts. In this phase, an accretion disk is formed. This phase is usually referred as "zero age" of a star, because it is the first time it is detectable.

From this point on, the protostar accretes matter until it reaches its final mass. Note that low mass stars end the accretion phase before reaching the main sequence, while high mass stars probably continue the accretion process even after hydrogen burning sets in. In the model by Shu (1977), the accretion rate is constant in time with a value of c_s^2/G. Considering an infalling envelope at ≈10 K, the accretion rate is $\approx 1.6 \cdot 10^{-6}$ M$_\odot$ yr^{-1}. In turn this leads to the time needed to form a 1 M$_\odot$ star: $\approx 7 \cdot 10^5$ years. The global time scale is quite accurate, even with the heavy approximation of constant accretion rate. A more realistic scenario contemplate an initial phase of high accretion, lasting roughly 10^4 years, followed by a decline in the accretion rate. See fig.1.1.

Once the internal temperature reaches 10^6 K, deuterium fusion takes place. Stars with mass lower than 1 M$_\odot$ burn a quantity of deuterium of the same order as the one accreted form the disk. This is possible only if there is an efficient mechanism to transport the deuterium from the surface to the interior of the protostar. Indeed, this process is convection, effectively driven by the deuterium burning. Since accretion decreases in time, the period of deuterium burning for theses stars is not long. More massive stars, on the other hand, continue to accrete for longer times. As a consequence deuterium burning continues even after it is depleted in the centre, giving rise to shell type burning.

The HR diagram is very useful for the understanding of stars in general, and can be used to explain the evolution of protostars as well. In the HR diagram there are zone of instability, in which the first adiabatic index is out of the range of stability. Hayashi (1966) calculated the boundary of such zones, corresponding to fully convective protostars. These boundaries correspond with different vertical lines on the HR diagram, depending on the mass of the star. Fully convective protostars would follow such lines from top to bottom. This means that the luminosity decreases, but the temperature remains roughly constant. The beginning of the "Hayashi tracks" corresponds to the previously described phase C. Under these conditions the opacity in the protostar is very high, and the approximation of full convectivity is quite good. When opacity drops, internal temperature rises and a radiative core forms in the protostar. This leads to a horizontal evolutionary line on the HR diagram called “radiative track”.

Protostars are classified based on the characteristics of their spectral energy distribution (SED). The classification is based on the excess of infrared flux with respect to a stellar black body emission (see fig. 1.2). The spectra are divided in four groups, depending on the spectral index defined in the infrared band between 2.2 and 25 μm:

$$\alpha_{IR} = \frac{dlog\,(\lambda F_\lambda)}{dlog\lambda}. \tag{1.2}$$

- **Class 0** Undetected below 25 μm.
- **Class I** $\alpha_{IR} > 0$.
- **Class II** $-2 < \alpha_{IR} < 0$.
- **Class III** $\alpha_{IR} < -2$.

The infrared excess is attributed to thermal emission from dust in the molecular envelope around the protostar. Note that class 0 objects have been discovered, and therefore added to the classification, after the other classes, because of the difficulties in the observations. The properties of the various classes are roughly summarized in fig. 1.3. The scheme suggests a link between class and evolutionary stage of the source. Although this picture is approximately correct, extreme care must be taken in the interpretation, because the circumstellar envelope is not transparent for radiative signatures and does not allow direct observation of the protostar itself. Finally, note that this classification is valid for masses up to 2 $M_\odot$, a range which covers most of the stars in the galaxy.

Class 0 Protostars

These protostars are characterized by high emission in the infrared part of the spectrum above 25 μm, but are invisible below this value. This is a strong indication that the source is deeply embedded into a molecular cloud. The mass of the envelope, as estimated by thermal emission from dust in the circumstellar material, ranges from ~ 0.14 to 2.8 $M_\odot$ and more. The mass of the envelope is generally bigger than the mass of the central source. The age of the system is estimated to be $< 10^4$ years. This class of objects presents outflows, but it is unclear if they are dominated by collimated jets or by wide angle winds.

Class I Protostars

These objects are low mass, highly embedded protostars during accretion. The envelope mass is much smaller than the one in class 0 protostars, with values between ~ 0.015 and ~ 0.15 $M_\odot$. This indicates that the accretion is in the late stages, and the star is almost at the birth line in the HR diagram (end of accretion and beginning of quasi-hydrostatic contraction to reach the main sequence).

Class II Protostars

This class corresponds to the so called classical T Tauri stars (CTTS), because of their similarity with the first discovered star of this type: T Tau in the Taurus cloud. They are low mass pre main sequence stars, with spectral type ranging from F to M, and effective temperatures of 3000 to 7000 K. The circumstellar envelope has been almost completely dispersed, so the stars are visible in optical wavelengths. Their distinctive signature is the strong Hα emission. They have a thick disk of about 0.01 $M_\odot$ and radius $\sim$ 100 AU. The disk contributes to the SED with a moderate infrared excess. Accretion rate is variable, but usually low, with values of roughly 10^{-6} $M_\odot$ yr^{-1}.

To find the origin of the Hα emission, it is necessary to understand more about the accretion mechanism. The rotation of the star, together with the convective motions inside it, produces a dynamo effect, leading to external magnetic fields. The interaction of the stellar magnetosphere with the accretion disk causes the disk to be truncated, and forces matter to flow in defined accretion streams and accretion columns. This is the region of the broad Hα line emission. The material flows basically in free fall, and accretion shocks can heat the plasma up to 10^6 K, producing soft X-ray emission. In addition, the accretion shocks produced at the star surface are the origin of an UV continuum emission at 10^4 K.

Class III Protostars

These stars are found in star forming regions, but they do not present strong Hα emission like class II. For this reasons they are called weak-lined T Tauri stars (WTTS). The IR excess is small or absent. Indeed, it is believed that they do not accrete material. They are, however surrounded by a thin, low mass disk, or by disk debris. It is possible that around these stars a protoplanetary disk is forming. WTTS are considered as an older population of stars with respect to the CTTS.

1.2.2 Herbig-Haro Objects

As introduced before, HH objects are small nebulae ($20 - 30$ arcsec) observed in relation with star forming regions. The shape is heterogeneous, varying from chaotic to bow shape to clear jet-like morphology. HH objects are often represented and associated with the well collimated jets ending with symmetric bow shocks, as shown for example in fig. 1.4. It has to be noted, however, that such morphologies are rare, and generally the observer is faced with a rich variety of shapes and structures. This variety depends on the different characteristics of the environments, on the different stage of evolution of the objects and on the chaotic nature of HH objects, recognized as shock waves in the outflows ejected by young stars.

Figure 1.4. Bipolar Herbig-Haro object HH 47, observed by ESO New technology telescope. *Red*: [SII] emission. *Green*: Hα. *Blue*: [OIII]. The protostar and the jet on the right are not visible because embedded in a dark molecular cloud.

Morphology

The strong shocks at the head of the jets are the result of the collision with the undisturbed ambient medium. This interaction region, called terminal working surface, is actually formed by two separate shock waves. A reverse shock decelerates the supersonic flow material, while a forward shock accelerates the the material in its path (Hartigan 1989). The latter shock can assume a curved shape. Its intensity is maximal just in front of the jet head, where the shock surface is perpendicular to the flow, and decreases as it becomes more bended away from the axis. The particular shape granted it the name bow shock.

The structure of these radiative shocks consists of two regions (Ostriker & McKee 1988). In the front, a very thin layer is responsible for gas heating and ionizations. This layer is normally too thin to be resolved by ground-based telescopes. Behind the first layer, there is a more extended cooling zone. Here, the gas emits forbidden lines of metals and recombination lines of hydrogen, which account for most of the radiation emitted by the shock. The region behind the shock front is stratified, in such a way that lines of species with higher excitation levels dominate the emission near the shock front, while species with lower excitation levels

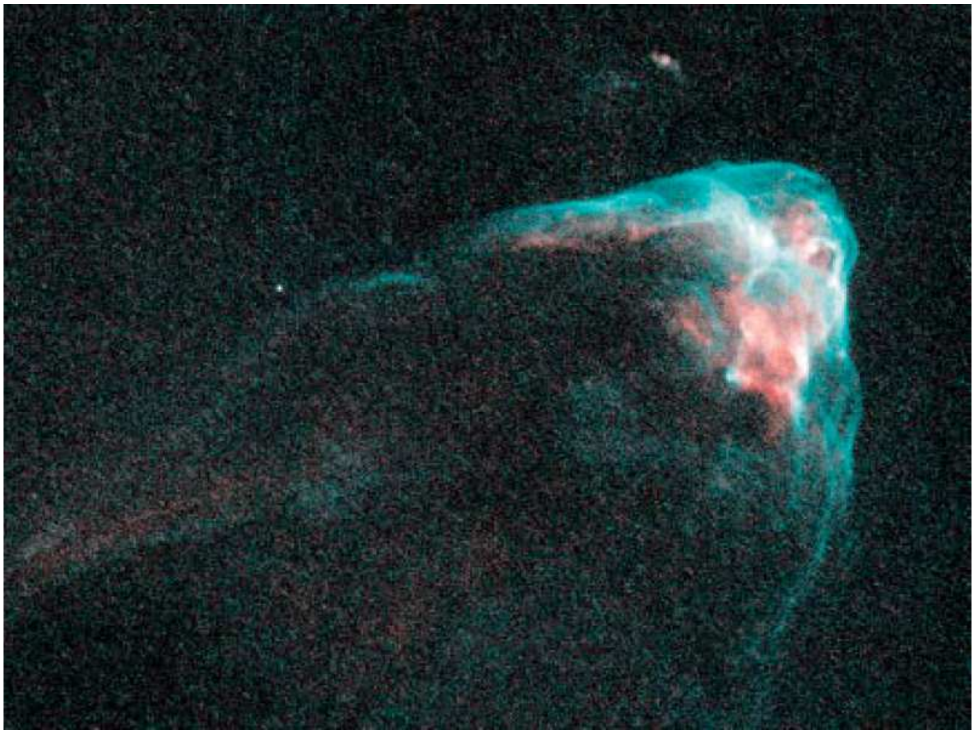

Figure 1.5. Hubble Space Telescope image of the bow shock HH34. *Green*: High excitation region as seen in Hα. *Red*: [SII] emission from the low excitation region.

dominate at increasing distance from the thin ionizing layer. For example, high excitation lines like [OIII] or Hα should peak closer to the front than lower excitation lines like [SII]. This is exactly what is observed in the symmetric, bow-shaped HH objects. In fig. 1.5 we can appreciate the great extension of the cooling zone in HH34, highlighted by the emission of [SII] (red). The bow structure is defined by Hα emission (green), as a consequence of collisional ionization of hydrogen at the shock front.

Observations of jets show a series of knots aligned or slightly wiggling, connected sometimes by fainter emission. Collimation of these objects is high, with a ratio of length over width of order 10 or more. Often, following the direction of the jet, bow shaped HH objects are found, suggesting a bigger scale for the outflow. The low excitation spectrum observed is proper of slow moving shocks, with velocities of the order of few tens of Kilometers per second at most. This fact does not match easily with the bulk velocity of the supersonic flow, usually of order of hundreds of Kilometers per second. The first attempt to explain this problem identified the knots with a series of oblique (therefore weak), stationary recollimation shocks (Falle et al., 1987, Cantó et al., 1989). This hypothesis was not confirmed by the observation of high proper motions of several knots, and a new explanation had to be found. Two theories are considered today. On one hand it is possible that hydrodynamic, magnetic or thermal instabilities are excited and grow in the jet, producing oblique traveling shocks. On the other hand, small variations

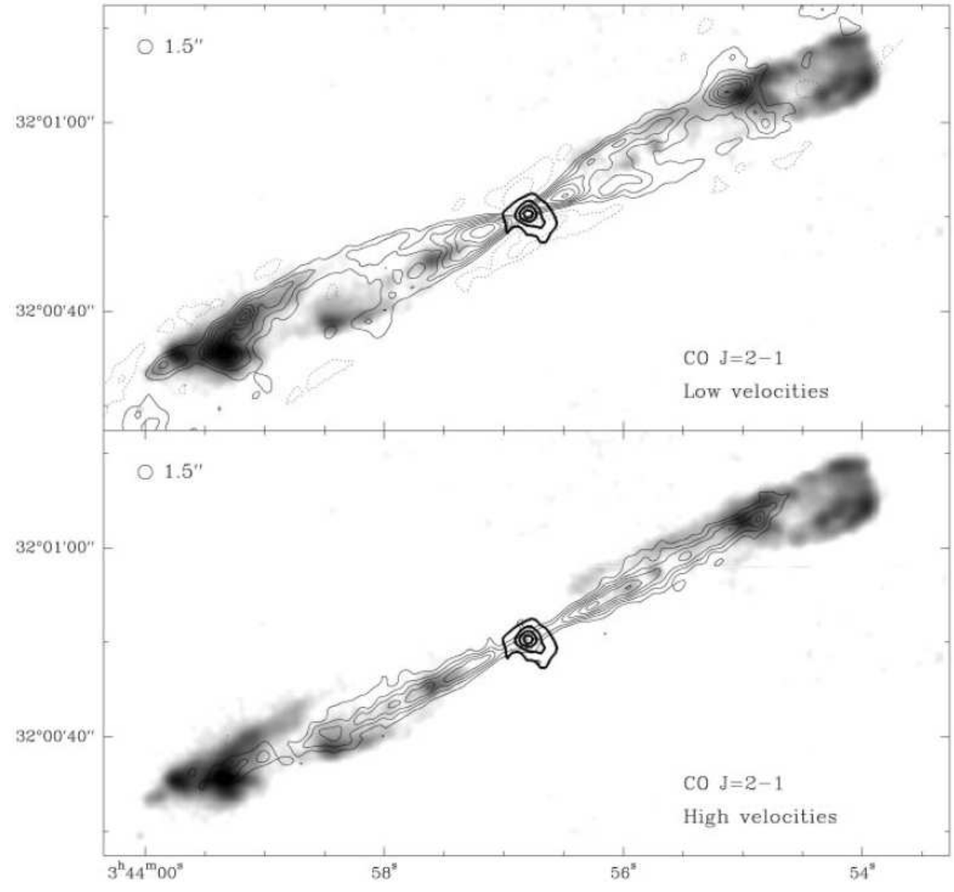

Figure 1.6. Images of HH 211 molecular outflow as seen in the CO J= 2 → 1 line (*thin contours*), superimposed on H_2 emission (*grey scale*) and radio continuum at 230 GHz (*thick contours*). *Upper panel*: Low velocity component. *Lower panel*: High velocity component.

in the ejection velocities would produce internal working surfaces with velocities of the same order of the perturbation producing them. Although it seems that this latter hypothesis is more popular in the community, the former cannot be completely ruled out, and it is possible that the two processes coexist in the same objects.

Kinematics

The proper motion of YSO jets on the plane of the sky can be measured by ground-based telescopes given excellent conditions. Results show velocities of $100 - 200$ Km s^{-1}, with a wide spread. Because of the limited resolution, however, the time interval between observations must be large, from several years to decades. Unfortunately this time is comparable to the cooling time in the post shock regions of interest, therefore errors in the measurements are introduced. This problem has been solved by the increased resolution of the Hubble Space Telescope (HST), with which it is possible to determine the proper motion of jets with images few years apart.

With this newly achieved precision it was possible to observe the following general behaviors.

1. Large velocities with small dispersions are found.
2. The tangential velocity tends to decrease as the distance from the axis increases.
3. in bow shocks, the tip moves faster than the lateral wings
4. in the sources where a reverse shock propagating upstream is found, the downstream shock has high proper motions, while the upstream shock is always slow or stationary.

Proper motions are the most precise method to determine possible candidates for the source of the outflow (see for example Devine et al., 1999). Once the source position is known, it is possible from the bulk velocity to calculate the source dynamical age, independently from the jet inclination with respect to the plane of the sky. Proper motions measurements can also greatly help in the recognition and identification of sources in crowded star forming regions, where several outflows are visible.

The radial velocity component in jets can be measured with long slit spectroscopy, and resulted in a high bulk velocity of the order of $100 - 200$ Km s^{-1}. Solf (1987) reported the first observations of lines splitting near the source. A high velocity component, with a gentle velocity decrease along the outflow axis was observed together with a low velocity component, presenting a steep acceleration. In the interpretation, a fast jet is surrounded by a layer of entrained material. The jet is slightly decelerated because of the interaction, while the external medium is accelerated. This observational signature, found first in HH 24, had been observed in several other objects.

With Fabry-Perot spectrometers and integral field spectrographs it is possible to deduce the kinematic of bow shocks. As expected the highest velocities are found at the tip of the shock, where large lines widths are present. The flow velocity decreases along the bow shock wings, and it is possible to observe the division of the working surface into bow shock and Mach disk (Morse et al., 1992, 1993).

Spectrophotometry

HH objects are broadly divided into high and low excitation objects (Bohm 1983). The flux ratios [OIII]5007/Hβ and [SII](6717+6731)/Hα are commonly used as excitation parameters, and allow the definition of high, intermediate and low excitation categories (Raga et al. 1996). These lines are reasonably close with each other, so the ratio is insensitive to reddening. In general, however, the high extinction of HH objects does not allow a correct interpretation of the lines without corrections for reddening. Possible measures of reddening come from measures of lines coming from the same upper level, for which the ratio is fully determined by theoretical transition probability and frequency (for example [SII]4068/4076 to [SII]10318/10337).

Line emission in HH objects is produced in shocks. The first plane-parallel models could not explain the simultaneous presence of low excitation lines, like [OI] and [SII], and highly ionized species, like [OIII] and [CIV]. Bow shock models, conversely, give rise to different velocities and therefore both high and low excitation lines. Within these models, it is possible to obtain the shock velocity and flow orientation using a single well-resolved profile of a low excitation line (Hartigan et al. 1987). Several authors have successfully fitted spectra from various sources with the models. Unfortunately, some problems still remain. While line ratios are well reproduced for low excitation objects, different line ratios in a single intermediate excitation object show a large spread in shock velocities, ranging from 30 to 100 Km s^{-1}. The shock velocity in high excitation objects is never greater than 100 Km s^{-1}, suggesting the presence of an (unknown) limiting mechanism.

The abundances of heavy elements like Fe and Ca can be measured as well. It is believed that such elements are trapped in dust grains in the interstellar medium, thus producing low abundances. Strong shocks, typical of high excitation regions, should be able to destroy the dust grains and return Fe and Ca in gas phase. Low excitation objects should, however, preserve some of the dust grains, showing lower abundances. Observations show high abundances of Fe and Ca both in high and low excitation regions, suggesting that at some point during their evolution, the material of the jet has passed through strong shocks.

HH objects are mainly emission dominated, but they present a weak blue continuum that rises in the ultraviolet (UV), that is believed to be caused by collisionally enhanced two-photon decay in neutral atomic hydrogen. Strong UV lines can provide significant cooling. In high excitation regions, the energy emitted in the UV can be higher than the optical one, while in low excitation objects, fluorescent lines in the Lyman bands of H_2 can be important. Observations in the UV are complicated by the large extinction of HH objects. In addition, several sources are reported to present considerable variability on short time scales.

Infrared Observations

The infrared (IR) emission from HH objects is mainly due to molecular hydrogen lines, which provide insights on the low velocity shock regions. In addition, several strong [FeII] emission lines are also present in the near IR. Observations with narrow band filters reveal the presence of shock excited near IR emission nebulae, that correspond sometimes to known HH objects. These nebulae are often found near deeply embedded class 0 sources, and are interpreted as parts of HH flows encountering significant extinction. This theory however, cannot be established as a general rule.

Molecular hydrogen lines, arising from the vibrational levels in the H_2 electronic ground state, dominate the spectra of HH objects in the near IR band. Most HH objects are detectable in H_2, the low excitation regions being the brightest. A bright and easy line to observe is the 1-0 S(1) line at 2.122 μ m. H_2 lines are excited in shocks at temperature of the order of few thousands degrees Kelvin. In such a way only the low vibrational levels of the molecule are populated. Two different kind of shocks have been used to explain the IR spectra in HH objects: J-type (jump) and C-type (continuous) molecular shocks (Draine 1980). Both shocks do not dissociate molecular hydrogen, but the conditions are different. C-shocks require a magnetized, low ionized medium, while J-shocks are mainly non-magnetized. J-shocks have a thickness of the order of the mean free path, and for high velocity can dissociate ambient molecules. C-shocks, on the other hand, present a thick heating layer. Indeed, the low ionization level decouples neutral particles from the magnetic field, and ambipolar heating gradually takes place thanks to collisions between neutrals and ions. The often complicated structures of HH flows make it quite difficult to identify which shock type is dominant. In general, considering the various observations, the C-shock seems the most common, but there are some case characterized by j-shocks or both at the same time.

The abundance of H_2 in the HH jets and in the surrounding medium is of great importance for the resulting spectrum. If the jet flows through H_2 material, then the molecular hydrogen cooling is dominant. Without such condition, emission from [FeII] becomes the main source of emission (Reipurth et al. 2000).

In the mid and far IR, the emission of many sources is dominated by the line [OI]63μm. Thermal emission from dust grains has been observed in HH7 (Molinari et al. 1999), suggesting that dust grains can survive effects of shocks (see also Mouri & Taniguchi, 2000).

Giant HH Flows

The time scale for protostars accretion phase is typically of the order of 10^5 years. Assuming outflow velocities of 100 Km s^{-1}, in that time a clump of material with density higher than the surrounding medium can travel roughly 10 pc. It is therefore conceivable to expect outflows on such scales. Nevertheless, before 1994, it was widely believed that HH flows extended for fractions of a parsec at most. The first identification of a flow with dimensions greater than a parsec by Bally & Devine (1994), opened the way to subsequent observations and discoveries that changed our view on jets from young stars. Today, we have observed and identified tens of parsec-scale HH outflows. The dynamical age of these objects approaches the accretion age of their sources, thus providing important informations on protostar evolution.

The structure of most giant HH flows consists in multiple groups of HH objects aligned along the flow axis. There is evidence for variation in ejection velocity and direction, and even degree of collimation. The single HH objects can be interpreted as working surfaces generated when new faster ejecta collide with previously launched but slower clumps (Raga et al. 1990). As we move farther away from the central source, the shocks size increases. The spacing between shocks also increase in the same way. More distant shocks, in addition, are older and their structure appears much more chaotic. Shocks further away from the source are increasingly slow (with slower proper and radial motions). In the models, the ejected material is decelerated by interactions with the ambient medium (Cabrit & Raga 2000). The spatial distribution of shocks, namely an almost continuous jet close to the source, a series of close low excitation shocks farther away and finally isolated and well widely spaced shocks, indicates that the small amplitude velocity variations in the ejection history of the source happen on a short time scale, whereas large amplitude variations are relatively rare.

Usually, the large scale morphology of parsec scale flows is characterized by an S-shape, point-symmetric with respect to the source. Such morphology can arise as a consequence of precession of the source/accretion disk. Another observed morphology is C-shaped symmetry, found in HH 366. Possible causes are deflection by a wind or motion of the source in the surrounding cloud. These effects in turn can be used as a signature of dynamical interactions in multiple star systems.

The size of these giant outflows is roughly one order of magnitude larger than the host molecular cloud. Observations have confirmed that many giant HH flows have reached the rim of their molecular clouds and propagate through the external interstellar medium, injecting mass, energy and angular momentum. Because the complicated morphologies of molecular clouds, it is possible that part of the same cloud, or another cloud lies in the path of such jets. Indeed, we have evidence of few giant HH flows colliding with molecular clouds (for example HH 84 and HH 110).

Most giant outflows are associated with high-velocity CO emission, although the optical outflow is usually one order of magnitude bigger than the CO emission region. This line traces material entrained by the jet from the external medium. Once the jet propagates outside of the molecular cloud, no more CO can be entrained, thus explaining the difference in size of the two emitting regions. Emission from H_2 follows basically the same principle. The entrainment process contributes to to enhance the effects of a giant HH flow on the molecular cloud. Such flows open large cavities in the host clouds, detected in optically thin molecular tracers like ^{13}CO, as a demonstration of the large impact of jets on the surrounding medium. Because of instabilities in radiative shocks and the random orientation of flows, the final result is turbulence injection in the cloud, with possible contribution to the star forming process.

Finally, parsec scale HH flows may be responsible for "chemical rejuvenation" of the molecular clouds. Indeed, the fast bow shocks produced by the jets dissociate the molecules, effectively contributing to the large abundances of atomic and ionic species like CI and CII. In this way, the presence of a strong UV radiation from O or B stars is not required. This kind of process is expected to act efficiently in young clusters characterized by several outflows, like NGC 1333 (Bally et al. 1996).

Physical properties of HH jets

The determination of physical parameters in jets is not easy, even with the rich amount of informations available from observations (see for example Mundt et al., 1987). First of all, the conditions of the observed gas are likely not in equilibrium, since the emission in HH objects traces the cooling in post shock regions. Moreover, any physical parameter derived from line ratios is mainly applicable only in the small emission region, and not for the whole flow. The electron density can be estimated from observed line fluxes, in particular from the ratio of the [SII] 6717 and 6731 lines. The hydrogen density, however, is a function of the ionization fraction, which is uncertain.

Nevertheless, it is possible to obtain rough estimates for the mass loss rates. The electron density ranges from 10 to 10^5 cm^{-3}, with typical values of $10^2 - 10^3$ cm^{-3}. Ionization fraction is very variable, ranging from $< 1\%$ to fully ionized, but it is generally low, staying at few percent. These values can be plugged in the following expression for an order of magnitude of the mass loss rate:

$$\dot{M} \approx 2.6 \cdot 10^{-8} n_3 V_{100} r_{100}^2 / \chi_{0.1} \ \mathrm{M}_\odot \ \mathrm{year}^{-1}, \tag{1.3}$$

where n_3 is the electron density in the jet in units of 10^3 cm^{-3}, V_{100} is the jet velocity in units of 100 Km s^{-1}, r_{100} is the jet radius in units of 100 AU, and $\chi_{0.1}$ is the electron fraction in units of 0.1. Another useful estimation is the mechanical luminosity of the flow, defined as the kinetic energy supplied per second to the flow. It is calculated as the total kinetic energy of the flow divided by its dynamical age. For example, HH 111 presents a mechanical luminosity of 1.5 $\mathrm{L}_\odot$, equal to 6% of the luminosity of the source (see Hartigan et al., 1994).

Magnetic fields could give an important contribution in the post shock regions, because the component parallel to the shock front would inhibit gas compression thanks to the resulting magnetic pressure. Unfortunately, it has been found that line ratios obtained by magnetized shocks are indistinguishable from line rations from slower unmagnetized shocks, for magnetic fields ranging between few and few hundreds microgauss (Hartigan et al. 1994).

Hydrogen density can be estimated in a model independent way, as suggested by Bacciotti et al. (1995). It is assumed that the ionization of O and N is controlled mainly by charge exchange with atomic hydrogen. The assumption, valid unless the ionization fraction is higher than 0.5, defines the relative abundances of various ions. Given the electron density n_e, derived from other methods, any line ratio is just a function of the ionization fraction x_e and the excitation temperature T_e. Combining the data from different lines it is possible to obtain x_e and T_e for the source. For example, for HH 34 a value of $x_e \approx 0.07$ is found, while for HH 111 $x_e \approx 0.11$ (Bacciotti et al. 1995). These values are a factor of 2 higher than those based on shock models. The excitation temperature is found to range between 4500 and 7000 K.

Entrainment and molecular outflows

HH objects, seen in the visual wavelengths, trace only the post shock regions of a flow because of the rapid cooling of the gas. Molecular emission in the millimeter wavelengths, on the other hand, is excited by collisions at temperatures of few kelvins at densities typical of molecular clouds. This means that CO emission is an ideal tracer of all the mass entrained by the outflow, which contains at least some molecules. Only 30% of the HH objects have been associated with molecular outflows. This can be explained by the fact that CO flows can be detected at large distances and in deeply embedded regions. Both cases are not favorable for optical observations. Two types of outflow can be recognized. The first one consists in the classical high velocity CO lobes, with $V < 30$ Km s^{-1}. It is characterized by poor collimation and it contains most of the mass of the outflow. The second one consists in an extremely high velocity (EHV) component, with $V > 30$ Km s^{-1}. This type is usually well collimated and can be observed only in the very young sources. See for example HH211 in fig. 1.6.

Young sources, indeed, are recognized to produce high density molecular jets, with a variety of different molecules. One of the commonly observed ones is SiO. This molecule was observed in a survey by Codella et al. (1999). They found that, for a given luminosity, youngest sources have the most SiO luminosity. The best candidate to observe the EHV CO jets are the very young Class 0 protostars. Because they are highly embedded in the molecular cloud, the shocks are mostly visible in [FeII] and H_2, but are not observable in optical. With age, the flow evolves and creates the cavities in the molecular cloud described before. In such a way, as the extinction decreases, the optical emission is increasingly easier to detect, but at the same time the molecular outflow becomes hard to observe.

In the past years several studies have tried to relate molecular outflows with HH objects (see for example Cabrit et al., 1997), resulting it two competing theories. In the first, collimated jets or winds are thought to entrain gas from the surrounding medium. This process can be observed in molecular emission like CO, which is due to thermal emission coming from the entrained post shock gas. In general, this theory predicts that the poorly collimated, low velocity molecular outflows are driven by the highly collimated jets. In the second theory, conversely, the central protostar drives a wide angle magnetized wind, the density of which converges on the axis. As a consequence the optical emission is peaked along the axis, giving the impression of a collimated flow. In reality much of the mass (roughly 50%) of the outflow is flowing at a large opening angle. This outflow forms a wind-bubble that creates a forward shock wave, thus producing the molecular outflow. Several observations have been carried out in search for indications that could exclude one of the two theories, but so far no answer has been found.

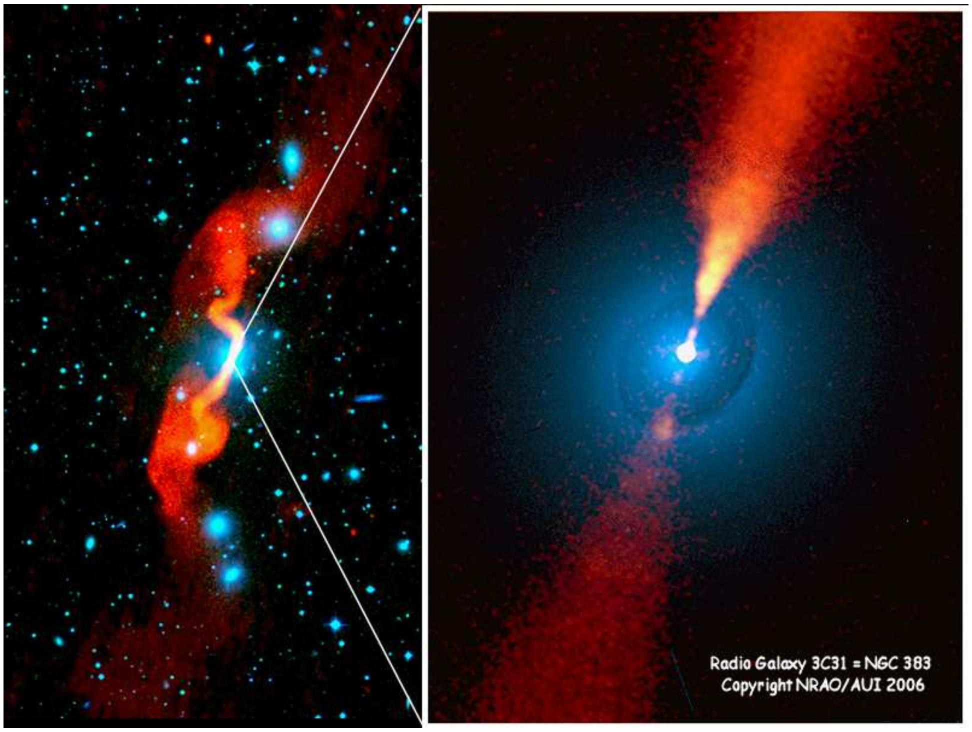

Figure 1.7. FR I galaxy 3C 31. *Red*: VLA radio images. *Blue*: Optical images. *Left*: VLA 21 cm image superposed on Palomar Sky Survey image. *Right*: VLA 3.6 cm image superposed on Hubble Space Telescope WFPC2 image. From Alan Bridle's webpage.

1.3 Extragalactic jets

The first observations of astrophysical jets date back to the early twentieth century, precisely by Curtis (1918). Indeed, he noted “a long, narrow, rather faint line of nebulosity” in the photographic plates of M87. At that time M87 was considered one of the numerous nebulae populating our galaxy, and this idea persisted for many years. Today we recognize in M87 a giant elliptical galaxy. It is relatively near, therefore well studied. The term “jet”, however, did not enter in the astronomical community until the ’50s, when it started to be used to describe structures possibly associated with material ejection from the inner parts of galaxies. Nevertheless, the concept of a continuous flow of plasma was still not taken into consideration.

In that period, a new wave of observations, made possible by the newly employed radio telescopes, hinted that extragalactic jets would be characterized by a strong radio emission. In particular, Bolton et al. (1949) made the first association of a radio source with an optical counterpart (Virgo A and M87).

The history of extragalactic jets has one more key step, when observations of the polarization of the light emitted from M87 suggested that the non-thermal spectrum emitted was due to synchrotron radiation (Baade 1956). This, in turn, stimulated the discussion because the

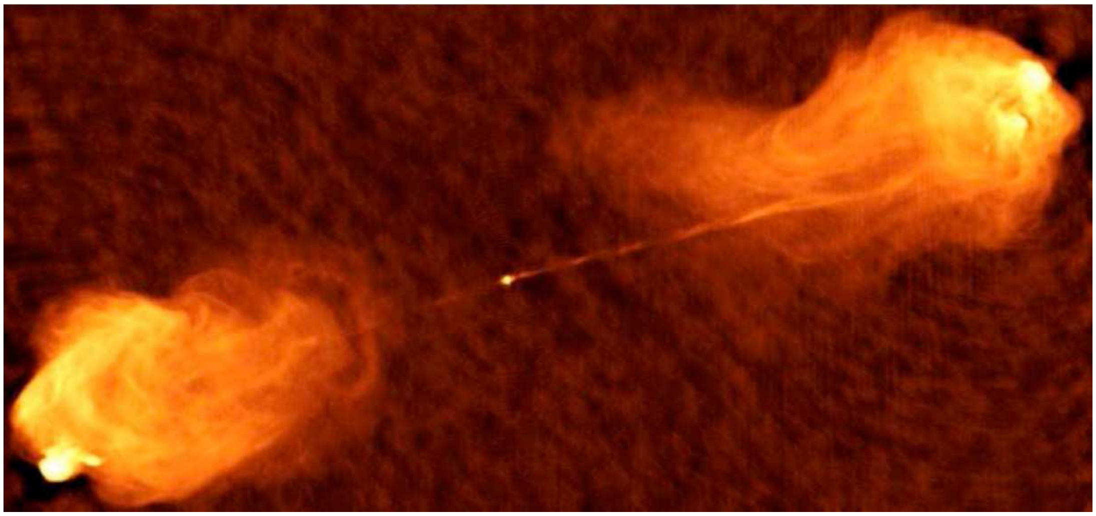

Figure 1.8. Radio image of the FR II galaxy Cygnus A. © NRAO/AUI/NSF.

particles subject to synchrotron losses present a mean path much shorter than the length of the jets, making it impossible for them to be emitted from the center of the galaxy source of the jet. To accommodate this two views, Felten (1968) suggested local acceleration of electrons by plasma processes, a theory which is at the base for the comprehension of extragalactic jets in the present day.

1.3.1 Active Galactic Nuclei

Extragalactic jets are observed in relation to some celestial bodies, called Active Galactic Nuclei (AGN). These objects are characterized by an extremely high emission from the central part, the nucleus. Using estimates for the mass of AGNs it is possible to calculate their energy production per unit mass. The values found, $\sim 10^3$ erg/sec/g, are three orders of magnitude higher than the thermonuclear reactions, recognized as the energy source of stars. Thus it is clear that AGNs are powered by another source of energy. The major accepted theory couples synchrotron radiation with accretion of matter on a supermassive black hole ($M \gtrsim 10^6 M_\odot$), but it is not the subject of this thesis, so we will not go into details.

The high energy production per unit mass is matched by the high power emitted, that can be 10^{47} erg/s or even higher. This places the AGNs among the brightest objects of the universe. The zone responsible for emission is essentially the nucleus, which is generally only few parsecs across. The emitted spectrum is non thermal, extended from radio to X and γ rays.

The definition of AGN is somewhat arbitrary. Indeed, most of the galaxies are believed to host a supermassive black hole in their cores, thus we expect more energy output than the one generated by the stars contained there. However, a galaxy is considered an AGN only when the activity of the nucleus is dominant with respect to the rest of the galaxy. Usually, a galaxy is defined *active* if the nucleus emission, usually in the radio band, is above a threshold.

AGNs are classified in several groups, described briefly here:

1. **Radio Galaxies**

   Galaxies with a strong radio emission, usually with $P_{1.4\mathrm{GHz}} > 2 \cdot 10^{23}\mathrm{WHz}^{-1}$. Usually they are big elliptical galaxies with dimensions up to ~ 1 Mpc. Their morphology allows for division in two classes:

   - **Compact Radio Galaxies**

     The dimensions of the zone of radio emission of these galaxies are smaller or comparable to the dimensions of the optical image of the galaxy. The radio emission zone is usually very small, limited to the nucleus.

   - **Extended Radio Galaxies**

     The dimensions of the zone of radio emission of these galaxies are bigger than the dimensions of the optical image of the galaxy. The structure is mainly bipolar, formed by two big lobes several Mpc away from each other. Because of luminosity and morphology differences, it is possible to define two more sub-classes (Fanaroff & Riley 1974):

     (a) **FR I Galaxies**

     The less luminous of the two classes, with $P_{178\mathrm{MHz}} < 5 \cdot 10^{25}\mathrm{WHz}^{-1}$. The maximum radio emission is close to the centre and it fades gradually with the distance from the core.

     (b) **FR II Galaxies**

     The most luminous of the two classes, with $P_{178\mathrm{MHz}} > 5 \cdot 10^{25}\mathrm{WHz}^{-1}$. The maximum radio emission comes from the end of the lobes.

   The numerous observations of these objects revealed that most of the FR I galaxies have jets, two beams oriented in opposite directions, typically well collimated up to Kpc scales but then decollimate to produce tails gradually more tenuous. A prototype of FR I radio sources is the galaxy 3C 31, shown in fig. 1.7. Jets from FR II sources, on the other hand, remain collimated until the bright edge of the radio lobes. They are typically one sided, because of beaming effects. A remarkable example of such objects is the galaxy Cygnus A (fig. 1.8).

2. **Seyfert Galaxies**

   These are usually spiral galaxies with an unusually high luminosity from the centre and particularly broad emission lines in their spectra. The details of the lines are used to classify them in two groups:

- **Type 1 Seyfert Galaxies**

  This type of galaxies presents very broad "allowed" lines, like the hydrogen Balmer series. Considering the broadening as due to Doppler shift effects, the material emitting the lines is moving at very high speed, of the order 5000 – 10000 Km/s. The "forbidden" lines are also broadened, but the corresponding velocity is smaller, 200 – 400 Km/s.

- **Type 2 Seyfert Galaxies**

  In this type, allowed and forbidden lines present roughly the same broadening, corresponding to velocities up to 1000 Km/s. The lines are anyway much broader than most of the lines in normal galaxies.

In the standard model for Seyfert galaxies, ionizing photons are emitted from a small central source and propagate through two different gas regions. The inner zone is called *broad line region* (BLR), because it is the source of the broad lines in the spectrum. The variability in the lines and in the continuum of the spectrum is observed on timescales of the order of few weeks or months. This gives an upper limit on the dimensions of the BLR of the order of 10^{14} m. The *narrow line region* (NLR) is $10^2 - 10^3$ times bigger than the BLR and is situated outside of it. The different dynamics and density of the two regions determine the particular observed spectra.

3. **Quasars**

   Quasars are similar to radio galaxies in the sense that they both have a strong radio emission compared to normal galaxies. The optical image of quasars, however, appeared to the first observers as an object similar to faint stars (Matthews & Sandage 1962). Hence the name *quasi-stellar object*, or quasar. Like Seyfert galaxies, quasars present broad emission lines, but the main characteristic of these objects is the strong redshift of the spectrum, index of fast recession. Following Hubble's law, we infer that they are at cosmological distances. Among normal quasars, there are peculiar objects, divided in two categories:

   - **Blazars**

     There objects are characterized by strong variability in several wavelength bands, like radio, visible and X. Also the polarization is affected. The variability time scale can be very fast, ranging from few years to few hours and even minutes. We can estimate then that the linear dimension of the source is of the order of 10^{13} m.

   - **Radio-quiet Quasars**

     These quasars present a lower radio luminosity compared to the other ones, typically $P_{5\mathrm{GHz}} < 5 \cdot 10^{24}\mathrm{WHz}^{-1}$. The emission in the X rays is lower as well. These objects are more difficult to detect, but it is believed that they are much more numerous than the radio-quasars.

This rich variety is completed by other types of galaxy cores with peculiar activities, like Liners, Starburst galaxies and luminous infrared galaxies. It is possible, however, to unify some AGN types by thinking that they are actually the same kind of object viewed in a different orientation. In the model, matter is accreting onto a super-massive black hole (the source nucleus), forming a thick torus around it at parsec scales. Accretion converts the potential gravitational energy directly into photons and indirectly into kinetic energy channeled in the collimated jets formed along the accretion disk rotation axis. An ionizing radiation is emitted from the inner part of the system with a continuous spectrum form radio to X rays. Optical emission lines, both narrow and broad, are produced from the recombination of electrons and ions in the gas previously ionized. The type of object observed from the Earth depends on the angle θ between the rotation axis of the disk and the plane of the sky. Three main scenarios can occur:

1. The angle θ is zero or reasonably small, in such a way that the torus obscures the core of the host galaxy.
2. The angle θ has an intermediate value, so that the torus cannot obscure the nucleus.
3. The angle θ is close to 90 degrees, so that the line of sight is almost parallel to the rotation axis of the disk.

In this way, Seyfert galaxies can be unified: For Seyfert 1 galaxies, the observer has a direct view of the nucleus. For Seifert 2 galaxies, the torus obscures the core and the BLR, but not the still visible NLR. Unification can also be made between radio galaxies, radio-loud quasars and blazars. Radio galaxies present long collimated outflows with moderate inclinations with respect to the plane of the sky, so they fall in the first of the three scenarios described above. Quasars do not present any sign of absorption due to a torus. They correspond to the second scenario. When the angle θ approaches 90 degrees, relativistic beaming dominates the emission and Blazars are observed.

1.3.2 Model of extended radio sources

With extended radio sources we refer to objects with a zone of radio emission possibly larger that the optical image of the source. These includes basically radio galaxies, quasars and blazars. Although the sources have different properties, as described above, it is useful to mention the main structures that can be found in most of the sources in various forms and proportions:

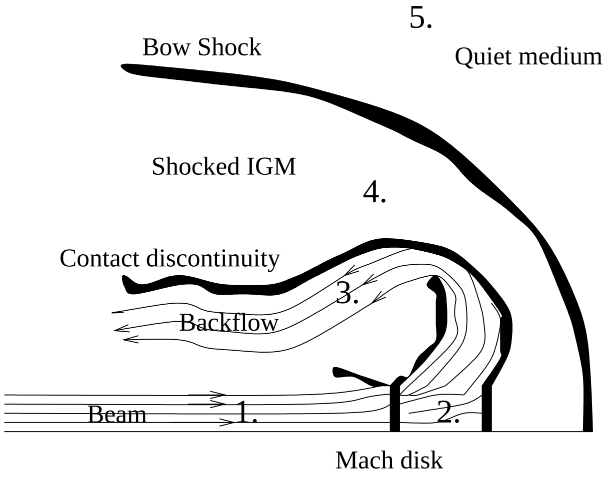

Figure 1.9. General structure of the cocoon. Adapted from Norman et al. (1982).

- the *core* from which the jet is emitted. It coincide usually with the nucleus of the galaxy connected with the radio source.
- the *jets*, collimated beams of particles propagating through the intergalactic medium.
- the *lobes*, extended regions emitting in the radio band.
- the *hot spots*, the zones of intense radio emission in the lobes.

These structures can appear very differently depending on the sources. For example, in FR II sources the jets are somewhat fainter than the lobes, and the hot spots are clearly visible. In FR I sources, conversely, hot spots are weak or absent, and the jets appear more prominently. Jets are in general very well collimated, i.e. their length greatly exceeds the radius. This feature requires a confining mechanism that can be either pressure from the ambient medium, or due to magnetic field, or both.

Phenomenological models predict that two opposite jets are formed and collimated from the core of AGNs, mainly using the gravitational energy released by accretion. The infalling material organizes itself into an accretion disk. The two jets are magnetized, supersonic and superalfvénic, and launched along the angular momentum axis of the disk. The propagation of the jets in the intergalactic medium allows energy and momentum transfer at great distance from the core of the galaxy. The interaction with the ambient medium can excite instabilities in the jet and produce shock waves, which in turn can provide a mechanism of reacceleration of particles to sustain the synchrotron emission along the beam.

The jets end in the extended radio lobes, where they release their energy (in FR II sources, in the form of hot spots). Because jets are supersonic with respect to the surrounding medium, the terminal point of the jet forms a shock wave which propagates through the intergalactic medium.

The intensity of this discontinuity is maximum directly in front of the jet, and decrease as it bends around the sides of the jet. Because of the shape, this structure is called *bow shock*.

The supersonic nature of the jet, together with the characteristic of the intergalactic medium, causes a deceleration of the jet flow to the asymptotic ambient conditions, through a strong planar shock wave called *Mach disk*. This localized region presents high pressure, and is identified with the hot spots at the end of the radio lobes. The propagation of this turbulent region generates a *cocoon*, with pressure higher than the external medium (Begelman & Cioffi 1989). The pressure gradient between Mach disk and bow shock produces a flow which propagates sideways and opposite to the direction of the jet. This structure is often called *back flow*.

Another way to transfer energy from the jet to the external medium is present over the whole surface of the beam. It is clear that the jet is moving faster than the gas immediately adjacent to it, even considering that the gas has been shocked by the bow shock. As a consequence there is a velocity gradient around the jet, which is unstable against the Kelvin Helmholtz instability. This in turn causes internal shock waves and produces a mixing layer in which transfer of energy, momentum and material takes place.

Derive an analytical model for these structures is very hard, because of the presence of such non-linear processes. It was possible, however, to confirm the global scenario described above with numerical simulations. Among the first we cite for example Norman et al. (1982). Following Massaglia et al. (1996), we can identify five different regions, visible in fig. 1.9:

1. The jet itself.
2. The jet material that has passed through the Mach disk, but is still flowing in the direction of the jet.
3. The backflow, formed by the jet gas shocked in the Mach disk and reflected in correspondence with the contact discontinuity between the jet material and the external medium. This region flows in opposite direction with respect to the jet, and forms the cocoon.
4. The external medium, shocked by the bow shock.
5. The external medium not yet influenced by the jet.

In this framework, the hot spots in the radio maps of the extended radio sources are identified with the regions where the jet dissipate its kinetic energy (Mach disk), and the radio lobes with the cocoons. Simulations have demonstrated how cocoons form only when jets are less dense than the ambient medium, and how the pressure in the cocoons formed by highly supersonic jets can maintain alone the collimation of the jet (Loken et al. 1992). The different characteristics of jet and ambient medium can also explain some of the different morphologies of radio sources. Following Bodo et al. (1994) for example, FR I sources should present jets with higher density than the external medium and with moderate Mach numbers. In such a way the jets are turbulent and highly decelerated. Emitting particles, therefore, are spread out over large volumes and produce the diffuse emission observed. FR II sources, on the contrary, should be characterized by fast jets, lighter than the external gas. Jets tend to be more stable and collimated, and maintain a clear separation between their interiors and the ambient medium. The shocks produced by the instabilities are far apart and concentrate the emitting particles in small regions, giving rise to relatively faint jets.

1.4 Hints on jet formation

The most accredited models for jet formation and collimation are based on the concept of magneto-centrifugal acceleration, first proposed by Blandford & Payne (1982). This mechanism is based on two fundamental ingredients: a rotating object and magnetic fields. The starting point is a strong magnetic field anchored on a rotating object, that can be a star, a disk or a falling envelope. In what follows we will describe briefly the case of a rotating accretion disk, because it can be used to explain both stellar and extragalactic jets.

Imagine an accretion disk in keplerian rotation, defined on a cylindrical coordinate system (r, θ, z) in such a way that the keplerian rotation is in the toroidal direction θ. In the inner part of the disk, the kinetic energy associated with the rotation is greater than the corresponding magnetic energy. In the poloidal plane (r, z) however, the poloidal magnetic field is strong enough to be regarded as a rigid guide for the plasma. In other words, close to the disk at the inner part of the disk, the keplerian rotational speed is much greater than the Alfvén speed, and this latter is much greater than the initial poloidal speed of the plasma. A commonly used corresponding mechanical example is beads (charged particles) on rigid wires (poloidal magnetic fields). In this example, the wires are rotating around the z axis with keplerian velocity. Because of centrifugal force, the particles are accelerated outwards along the poloidal magnetic field lines. Simple calculations show that the acceleration process can take place only if the angle ϕ, between the poloidal magnetic field line and the plane of the disk, is smaller than 60 degrees.

Once the plasma has reached the Alfvén surface, it has acquired enough kinetic energy to move independently from the magnetic field and, conversely, to drag it. Because of this and plasma inertia, the plasma is left behind the rotating field lines inside the Alfvén surface, and the magnetic field assume a helical shape building up a strong toroidal component. The resulting magnetic tension is always directed towards the axis of rotation and thus collimates the flow.

This mechanism is very successful and popular for several reasons. First, the resulting outflow is self collimated towards the axis, forming a jet. Second, the fact that the outflow originates in the inner part of the disk close to the source, is confirmed by the measurements of jet velocities, which are found to be close to the escape velocity of the central object. Finally, the magneto-centrifugal acceleration provides an efficient way to remove angular momentum from the disk material. Indeed, without a transfer of angular momentum, the material in the disk could not accrete at all. It is possible to transfer angular momentum from an inner annulus to an external one by means of viscosity. In general, however, the viscosity in accretion disks is extremely small, and the rate of angular momentum transfer is too slow to match with the accretion rates. Another source of angular momentum transport is turbulence, which can be caused by a linear magnetohydrodynamic instability called magnetorotational instability (MRI) (Balbus & Hawley 1991).

Several different competing models, based on the magnetocentrifugal acceleration mechanism, have been developed in the past years. For a review of the stellar case see Ferreira et al. (2006). Theoretical and observational arguments are not yet in favor of a single one to explain jet formation.

In this thesis, we focus on the effect of reversed magnetic fields on the KH instability . This particular configuration is supported by strong theoretical arguments emerging from the original "X-wind" jet launching models by Shu et al. (1988), later generalized to take into account low accretion scenarios (Shu et al. 1994). In these models, the dipolar magnetic field around the central protostar interacts with the accretion disk. As a consequence, the disk is truncated and accretion takes place along funnel flows, while the truncation point becomes a "X-point" that drives the outflow. This model is relevant to our problem because of the resulting topology of the magnetic field above the disk. In the region outside the "X-point", the field lines connecting the star with the disk naturally open up in vertical direction forming a magnetic reversal. Time dependent numerical MHD simulations of the star-disk interaction have also shown similar magnetic field structures (Bessolaz et al. 2008). Another example of a more complicated magnetic topology has been investigated in 3D by Romanova et al. (2008). This type of magnetic topology occurs also in all models with zero net-flux, relevant for extragalactic jet formation. In fact, a closed dipolar configuration in a disk, which undergoes magnetorotational instability, is advected towards the central object and then dragged along by escaping disk winds, resulting in antiparallel magnetic fields (see for example the simulations by Beckwith et al. 2008).

1.5 Jet stability

It should be clear from the previous sections that astrophysical jets are characterized by a remarkable stability, clearly visible in the ratio between the jet length and its radius, observed to be of the order of 100. The opening angle is also very small. This tells us that the jets propagate for very long distances maintaining a considerable fraction of the initial velocity and without expanding sideways in a drastic manner. These properties may appear quite striking by themselves, but when models and calculations about stability are considered, they become an unsolved puzzle.

Indeed, linear stability analysis predicts a complete and fast disruption of the flow on length scales much shorter than the observed jet lengths by roughly one order of magnitude (Ferrari 1998). Among the various possible instabilities affecting a plasma, two appear to be determinant for the survival of plasma beams, the idealized models of astrophysical jets: the Kelvin Helmholtz (KH) instability and the current driven (CD) instability. Sheared flows in general are subject to the KH instability, the physics of which is enriched by the presence of magnetic fields. The presence of strong electric currents is the cause of the CD modes, a kind of instability known to be extremely disruptive in the plasma physics community.

Magnetic fields are sometimes invoked to stabilize the instabilities. It is the case for the KH instability embedded in uniform magnetic fields parallel to the jet axis. It is unlikely, however, that jets are characterized by the very strong magnetic field required for stabilization (see chap. 3). On the other hand, the toroidal component of the magnetic field, used to justify the outflow self collimation, is the primary source of electric current, thus exposing the jet to more unstable modes. Interplay with different instabilities is likely to considerably complicate the picture.

To display such collimation and lengthy propagation, astrophysical jets have found a way to remain sufficiently stable and not undergo disruption. The comprehension of these ways rests in the hands of theory and numerical simulations, which can suggest properties and mechanisms to achieve the needed stabilization, as well as indicate possible explanation for jet features like knots and helical deformation. Such structures could arise as a consequence of the growth of instabilities, but a mechanism to avoid flow disruption is needed. The work in this thesis is set in this framework, and wants to shed a bit more light on the behavior of the KH instability in astrophysical jets.

1.6 Aims and plan

Magnetohydrodynamics (MHD) is the the first approximation model to describe the plasma in astrophysical jets. This system of equations is rich enough so that no general solution is known. Analytical treatment is possible under heavy assumptions like stationarity and/or self similarity, or in the limit of small perturbations around an equilibrium. This last approach, called linear study, is suited to investigate the plasma instabilities, which may disrupt a flow or an equilibrium. Even in this case, though, the analytic treatment is limited to very simplified models. Nevertheless, it is possible to obtain important results for the stability of jets, that we describe in chapter 2, together with the basics of MHD.

To be able to study more complex, albeit still idealized, models of jets, both in the linear and non-linear regime, one must use numerical methods. Computational physics has grown in the past years together with the power of available computers. In this thesis we present the results of numerical simulations both in the linear and non linear regimes, using the numerical codes LEDAFLOW (Nijboer et al. 1997) and PLUTO (Mignone et al. 2007). The aim of the thesis is to investigate the stability of astrophysical jets, and in particular to examine the effects of instabilities on the jet survival and morphology. We concentrated on the study of a particular magnetic topology, antiparallel magnetic fields, to understand if the jet is more or less disrupted than analogous cases with uniform magnetic fields, and to compare the resulting morphologies.

The work done revolved around the study of the KH instability in various configurations. We started examining the KH instability of a single shear layer in two and three dimensions, and continued with the analysis of slab jets: two-dimensional flows delimited by two shear layers. This kind of geometry allows for both varicose and sinuous modes, in contrast with axisymmetric simulations which can only reproduce the varicose mode. More sophisticated, fully three-dimensional simulations of jets have been performed as well.

In summary, chapter 2 contains the basics of MHD and the theory of linear stability analysis, together with some important applications and results for astrophysical jets. In chapter 3 we describe the KH instability of a single shear layer. Then, we present the results relative to the antiparallel magnetic topology as compared to the results of a uniformly magnetized layer, already known in the literature. Both single modes of the instability, and extended domain containing several modes, are discussed in this chapter. Three-dimensional simulations are also examined here. Chapter 4 is dedicated to the simulations of jets, both in two and three dimensions. Chapter 5 contains a summary of the results together with the relevance for astrophysical jets and a discussion on the possible future improvements of the simulations and the models employed in this work. Finally, in appendix A we describe briefly the numerical codes used for the simulations, and in appendix B we included a test for numerical codes prepared for a joint project in the Marie Curie Research Training Network JETSET.

Chapter 2

Theory of jet instabilities

This chapter has the function to introduce the theory of instabilities applied to astrophysical jets. It is divided in two main parts. The first section describes the ideal magnetohydrodynamic equations as the main building block for jet models. The second section introduces the linear theory of instabilities and the first simple applications to astrophysical jets.

2.1 Introduction on Magnetohydrodynamics

Magnetohydrodynamics (MHD) is a single fluid model which describes macroscopic conducting fluids, notably plasmas. It is based on several assumptions and limitations. However, plasmas often do not satisfy the basic assumptions, for example that the plasma should be collisionally dominated. Nevertheless, experience and experiments have shown that the model provides good results in the macroscopic behavior of plasmas. This apparently lucky coincidence has in reality physical ground. Firstly, the parts of the model that are not valid, as a consequence of the violation of the validity conditions, usually do no enter in most phenomena of interest. Moreover, certain sections of the model are not affected by the assumptions used to obtain the other parts, thus opening MHD to a wider range of validity. Therefore, it is useful to consider MHD as an asymptotic model.

MHD is especially suitable to describe the effects of a magnetic geometry on the macroscopic equilibrium and stability of plasmas. The model can be used, for example, to determine how magnetic forces act to keep a particular equilibrium, or to understand why one particular configuration is more stable than others. This is very important because, in nature, only stable equilibria exist. The stability theory, which we discuss in the second section of this chapter (sec. 2.2), predicts often instability for solutions that appear to describe well the observed plasma configurations. This is the case of astrophysical jets for example. They are subject to a wide range of instabilities, from the Kelvin-Helmholtz instability due to velocity shear, to Current Driven modes, caused by the presence of helical magnetic fields. The linear stability analysis has a very solid mathematical base, and provides the ranges of parameters for stability. It also helps greatly in the physical comprehension of the problems, serving as a firm starting point. The stability theory, however, cannot go beyond the linear phases of the instability. In general, rapid growth rates do not guarantee that a large amount of energy will be released. In addition, it is not possible to predict if some small perturbation on a system in equilibrium will evolve into oscillations around the equilibrium, or if the system will relax to another state.

To understand the evolution of a system, it is needed to go further and consider the non-linear dynamics involved. Despite the several approximations and simplifications used to derive the model, the MHD equations are too difficult to solve for most of the geometries of interest. Therefore, numerical computation became a major tool for physical investigation. With numerical simulations, one can find the "exact" solution to the equations, within the controllable discretization errors. A series of simulations for the same physical problem but with different parameters, can provide scaling laws in the parameter range, and ultimately can clarify the physical mechanisms and explain the behavior of a system.

In this section we focus on the meaning of the MHD equations, and on few consequences of the MHD model. We start by deriving the equations, and continue describing the conservation laws and some typical magnetic effects: magnetic pressure and tension, and field "frozen in" condition. We conclude with validity conditions and a discussion on non-ideal dissipative effects.

2.1.1 The ideal MHD equations

The full set of ideal MHD equations can be derived staring from the Maxwell's equations coupled with a kinetic model of the plasma, described by a Boltzmann equation for each species. Such derivation follows a standard procedure: from the kinetic models, the fluid moments are calculated, and the system is closed by appropriate assumptions. Several variations of this derivation can be found in the literature, with different amounts of detail (a very comprehensive work is found in Braginskii (1965)). Here, however, we decided to avoid the introduction of microscopic concepts, so we follow a purely macroscopic heuristic way, as found in Freidberg (1987).

This derivation is valid for any electrically conducting fluid, the properties of which are described by an equation of state. Let's consider a fluid element in a volume δV, with density ρ and mass $\rho\delta V$. We start by deriving the force balance on the fluid element. The inertial term is, by definition,

$$\rho\delta V\frac{d\mathbf{v}}{dt} \equiv \rho\delta V\left(\partial_t\mathbf{v} + \mathbf{v}\cdot\nabla\mathbf{v}\right). \tag{2.1}$$

The total force, which causes the acceleration, comes from three different contributions:

1. The thermal pressure force. If local thermodynamic equilibrium is assumed, the pressure tensor is isotropic, and the force can be written as

$$-\oint p\, d\mathbf{S} = -\delta V\nabla p. \tag{2.2}$$

The integral is over the surface of the volume element. In addition, p is the pressure and $d\mathbf{S} = \mathbf{n}dS$ is the surface element.

2. The magnetic force. The force acting on a single charge q_i is the Lorenz force $q_i(\mathbf{E}+\mathbf{v}\times\mathbf{B})$. The total force applied to the fluid element is, therefore, the sum over the single charges: $\delta q\mathbf{E}+\delta\mathbf{j}\times\mathbf{B}$. Here, δq is the total charge, and $\delta\mathbf{j}$ is the electric current carried by the fluid element. Quasi neutrality of the fluid implies that the net charge is zero. This condition is realized in dense fluids by electrostatic fields. It does not imply, however, that the electrostatic fields are vanishing. With these assumptions we can write the macroscopic Lorenz force:
$$\delta V\mathbf{j}\times\mathbf{B}. \tag{2.3}$$

3. The gravitational force. We can write:
$$\delta V\rho\mathbf{g} = -\delta V\rho\nabla\Phi_g, \tag{2.4}$$
where Φ_g is the gravitational potential.

With the mentioned contributions, the force balance is:

$$\rho\left(\partial_t\mathbf{v}+\mathbf{v}\cdot\nabla\mathbf{v}\right) = -\nabla p+\mathbf{j}\times\mathbf{B}-\rho\nabla\Phi_g, \tag{2.5}$$

also known as Euler's equation. Although gravitational effects may be important for astrophysical plasmas, we will neglect this term in our work. Note also that gravity can usually be neglected for laboratory applications.

Regarding the magnetic field, we neglect the displacement current in Ampére's law, because we consider the limit of non-relativistic velocities:

$$\mu_0\epsilon_0\frac{\partial\mathbf{E}}{\partial t} \ll \mu_0\mathbf{j}. \tag{2.6}$$

Moreover, we set $\mu_0 = 1$ for convenience. Then it follows:

$$\mathbf{j} = \nabla\times\mathbf{B}. \tag{2.7}$$

To follow the dynamics of the magnetic field, we employ Faraday's law:

$$\partial_t\mathbf{B} = -\nabla\times\mathbf{E}. \tag{2.8}$$

If we consider that the fluid in motion with respect to the magnetic field with a velocity $\mathbf{v}$, then we write Ohm's law as follows:

$$\mathbf{j} = \sigma\left(\mathbf{E}+\mathbf{v}\times\mathbf{B}\right), \tag{2.9}$$

where σ is the plasma conductivity. Combining equations 2.7, 2.8 and 2.9, we obtain:

$$\begin{aligned}
\partial_t \mathbf{B} &= -\nabla \times \left(\frac{\mathbf{j}}{\sigma} - \mathbf{v} \times \mathbf{B} \right) \\
&= \nabla \times (\mathbf{v} \times \mathbf{B}) - \frac{1}{\sigma} \nabla \times (\nabla \times \mathbf{B}) \\
&= \nabla \times (\mathbf{v} \times \mathbf{B}) - \frac{1}{\sigma} \left[\nabla (\nabla \mathbf{B}) - \nabla^2 \mathbf{B} \right].
\end{aligned}$$

We finally arrive at the induction equation

$$\partial_t \mathbf{B} = \nabla \times (\mathbf{v} \times \mathbf{B}) + \frac{\nabla^2 \mathbf{B}}{\sigma}, \tag{2.10}$$

which describes the evolution of the magnetic field in a plasma moving at speed $\mathbf{v}$. For the derivation we have used the property of the magnetic field to be solenoidal, $\nabla \mathbf{B} = 0$, and we have assumed that the conductivity is spatially constant, i.e. $\nabla \sigma = 0$. The ideal MHD approximation considers the plasma as a perfect conductor, so that $\sigma \to \infty$. This implies that in a reference frame moving with the plasma, the electric field is zero. Hence, the induction equation can be rewritten as:

$$\partial_t \mathbf{B} = \nabla \times (\mathbf{v} \times \mathbf{B}). \tag{2.11}$$

The plasma density obeys the continuity equation, deduced by mass conservation:

$$\partial_t \rho + \nabla \rho \mathbf{v} = 0. \tag{2.12}$$

Moreover, the plasma follows approximately the ideal gas law $p = (n_i + n_e) k_b T$, where n_i and n_e are the number densities of ions and electrons respectively, and k_b is the Bolzmann's constant. The MHD approximation also considers that the variations of thermodynamic state are sufficiently fast and developed on sufficiently large scales, so that dissipation effects are negligible. As a consequence we can use the adiabatic equation for the changes of state of the plasma:

$$\frac{d}{dt} \left(p \rho^{-\gamma} \right) = 0. \tag{2.13}$$

The closed set of equations 2.5, 2.11, 2.12 and 2.13 describes the ideal MHD.

Usually, in numerical treatments, one uses to solve explicitly the equation of energy conservation, described in the next section. In addition, the system of MHD equations can be written in the following conservative form:

$$\begin{aligned}
\frac{\partial \rho}{\partial t} + \nabla \cdot (\rho \mathbf{v}) &= 0, && (2.14) \\
\frac{\partial \mathbf{m}}{\partial t} + \nabla \cdot (\mathbf{m}\mathbf{v} - \mathbf{B}\mathbf{B}) + \nabla p_t &= 0, && (2.15) \\
\frac{\partial \varepsilon}{\partial t} + \nabla \cdot \left[(\varepsilon + p_t) \mathbf{v} - (\mathbf{v} \cdot \mathbf{B}) \mathbf{B} \right] &= 0, && (2.16) \\
\frac{\partial \mathbf{B}}{\partial t} + \nabla \cdot (\mathbf{v}\mathbf{B} - \mathbf{B}\mathbf{v}) &= 0, && (2.17)
\end{aligned}$$

where ρ is the density, t is the time, $\mathbf{v}$ is the velocity, $\mathbf{m} = (m_1,m_2,m_3) = \rho\mathbf{v}$ is the momentum field and $\mathbf{B}$ is the magnetic field. $\varepsilon = u + \mathbf{m}^2/2\rho + \mathbf{B}^2/2$ represents the total energy density with u being the internal energy density. Finally, $p_t = p + \mathbf{B}^2/2$ is the total plasma pressure. Note that in our units, a factor $1/\sqrt{4\pi}$ is contained in the definition of the magnetic field and the magnetic permeability μ is set to unity. The system of equations is closed by the ideal gas equation of state with constant specific heats ratio $\gamma = 5/3$:

$$u = \frac{p}{\gamma - 1}. \tag{2.18}$$

Attempts to numerically integrate the system in a non conservative form result in failing to strictly conserve total energy.

2.1.2 Magnetic properties and equilibrium

To better understand the effects of magnetic fields on the plasma, it is useful to rewrite the Lorenz force density $\mathbf{f} = \mathbf{j} \times \mathbf{B}$, in the following form:

$$\mathbf{f} = \nabla \times \mathbf{B} \times \mathbf{B} = -\nabla\frac{B^2}{2} + \mathbf{B} \cdot \nabla\mathbf{B}. \tag{2.19}$$

The force density is orthogonal to the field and is split into two contributions. The first term is the gradient of the scalar $B^2/2$, therfore can be added to the pressure in the force balance equation (2.5). This term represents then a magnetic pressure, acting on the plasma in a similar way as the thermal one. The second term represents field line tension. To be able to make this effect evident, we can split it further into two terms using the curvilinear coordinate S along the field line. One component, $\partial_S B^2/2$, pulls along the field line towards the increasing intensity, but it is perfectly balanced by the parallel component of the pressure gradient. The other component, $B^2\partial_s\mathbf{e}_b$, can be rewritten $B^2\mathbf{n}/R$, where $\mathbf{e}_b$ is the unit vector tangent to the field line, $\mathbf{n}$ is the unity vector normal to the field line, and R is the curvature radius. This term pulls towards the curvature centre and tends to make the line straight. The field lines, therefore, act with a restoring force if curvature is applied to them, in a way comparable to the strings of a guitar.

In a jet with toroidal magnetic fields, the magnetic tension becomes:

$$\mathbf{B} \cdot \nabla\mathbf{B} = -\frac{B_\phi^2}{r}\mathbf{n}, \tag{2.20}$$

which point towards the the centre of curvature of the circular line of radius r, thus providing a confining force. In magnetocentrifugal models, the toroidal component of the magnetic field is generated naturally after the Alfvén surface, given rotation. To illustrate this result we start assuming a monopole-type magnetic field $B_r = B_0/R^2$, where B_0 is the magnetic field at the base and R is the radial coordinate in a spherical coordinate system (R, θ, ϕ). The magnetic field lines are radial, and we assume the plasma flows along them with a constant velocity V_0. The Alfvén Mach number of the flow is:

$$M_a^2(R) = \frac{V_0^2}{V_a^2} = \frac{\rho V_0^2}{B_0^2} R^4 = \rho_a \frac{V_0^2}{B_0^2}\frac{R^2}{R_a^2}, \tag{2.21}$$

where R_a is the Alfvén radial distance, and from mass conservation $\rho = \rho_a(R_a^2/R^2)$. Moreover, at R_a we have $M_a = 1$ and $\rho_a V_0^2 = B_0^2$. Therefore:

$$M_a = \frac{R}{R_a}. \tag{2.22}$$

We assume now that the base of the outflow rotates with angular velocity Ω. We can then derive the induced toroidal magnetic field component B_ϕ from the steady MHD equations:

$$\frac{B_\phi}{B_r} = -\frac{\Omega r_a^2}{r(B_r/\Psi_a)} \frac{r^2/r_a^2 - 1}{M_a^2 - 1}, \tag{2.23}$$

where Ψ_a is the mass flux per unit of magnetic flux, and r is the cylindrical radius. If we assume that the flow remains radial after the rotation starts, then $r = Rsin\theta$, and $M_a = r/r_a$. For distances much larger than the Alfvénic cylindrical distance, $r \gg r_a$, $R \gg R_a$, $M_a^2 \approx r^2/r_a^2$, so that:

$$\frac{B_\phi}{B_r} \approx -\frac{\Omega r_a^2}{r}\frac{\Psi_a}{B_r} = -\frac{\Omega r_a^2}{r}\frac{\Psi_a^2}{\rho}\frac{\rho}{\Psi_a B_r} = -\frac{\Omega r_a^2}{r}\frac{\Psi_a^2}{\rho}\frac{1}{V_0}. \tag{2.24}$$

Using

$$\frac{\Psi_a^2}{\rho} = \frac{\rho V_0^2}{B_r^2} = M_a^2 \approx \frac{r^2}{r_a^2}, \tag{2.25}$$

we finally derive:

$$\frac{B_\phi}{B_r} \approx -\frac{\Omega}{V_0} r. \tag{2.26}$$

So, the toroidal magnetic field grows with the cylindrical distance in relation to the poloidal field, and will eventually dominate, thus providing a confining force for the outflow. Note also that the centrifugal force is negligible, as well as pressure gradients (both magnetic and thermal). As a consequence, the outflow is collimated on axis. Finally, note that the toroidal magnetic field and the rotational velocity have opposite signs. As a consequence, their field lines describe helices wound up in opposite directions.

Looking at equation 2.5, one can immediately see that an MHD equilibrium is described by:

$$\nabla p = \mathbf{j} \times \mathbf{B} + \rho \mathbf{g}. \tag{2.27}$$

We can introduce here an important parameter for the plasma: $\beta = p/p_m$, is the ratio between thermal and magnetic pressure ($p_m = B^2/2$). On one hand, if β is smaller than 1, the plasma is magnetically dominated. In these condition, if the plasma is in equilibrium without gravity, a force free approximation can be assumed, so that $\mathbf{j} \times \mathbf{B} = 0$, thus $\mathbf{j} = \lambda \mathbf{B}$. In this case the magnetic pressure and tension effects are in equilibrium. On the other hand, if β is much greater than 1, the plasma is pressure dominated. This, however, does not allow to neglect the magnetic fields entirely: we will show in the next chapters how an apparently initially low magnetic field can dynamically affect the plasma.

2.1.3 Conservation laws and Alfvén theorems

The MHD equations imply a series of conservation laws. We spoke briefly about the conservation of mass, but we return on that for additional considerations. To compute the time derivative of the mass contained in a fixed volume V, we use the continuity equation (2.12):

$$\frac{d}{dt}\int_V \rho\ d^3x = \int_V \partial_t\rho\ d^3x = -\int_V \nabla\rho\mathbf{v}\ d^3x = -\int_S \rho\mathbf{v}\cdot d\mathbf{S}. \tag{2.28}$$

The meaning is clear: the mass in the volume V is constant unless the velocity v_n, normal to the surface enclosing the volume, is not zero. We can show that the mass M contained in a volume $V(t)$ moving with the fluid is conserved:

$$\frac{dM}{dt} = \int_V \partial_t\rho\ d^3x + \int_{\partial_t V} \rho\ d^3x = 0, \tag{2.29}$$

using eq. 2.28 and

$$\int_{dV} \partial_t\rho\ d^3x = \int \rho\mathbf{v}\cdot d\mathbf{S}\ dt. \tag{2.30}$$

The conservation of momentum, for constant volume, comes directly from the equation of motion (2.5):

$$\frac{d}{dt}\int_V \rho\mathbf{v}\ d^3x = -\int_S \left[\rho\mathbf{v}\mathbf{v} + \left(p + \frac{B^2}{2}\right)\mathbf{I} - \mathbf{B}\mathbf{B}\right]\cdot d\mathbf{S}, \tag{2.31}$$

where $\mathbf{I}$ is the identity matrix. In the notation used, if we consider a vector $\mathbf{u}$, then $\mathbf{uu}$ is a tensor $\mathcal{U}$ so that $\mathcal{U}^{ij} = u^i u^j$. The momentum of the plasma in a volume V is conserved when $v_n = B_n = 0$ and $p + B^2/2$ is constant on the boundary. Introducing the stress tensor

$$\mathcal{T} = \left(p + \frac{B^2}{2}\right)\mathbf{I} - \mathbf{B}\mathbf{B}, \tag{2.32}$$

the variation of momentum $\mathbf{P}$ in a volume $V(t)$ moving with the fluid is due to the stresses exerted of its surface:

$$\frac{d\mathbf{P}}{dt} = -\int_S \mathcal{T}\cdot d\mathbf{S}. \tag{2.33}$$

Relation 2.30 has been used for the derivation.

From the combined set of MHD equations, one can derive also the conservation law of total energy:

$$\frac{d}{dt}\int_V \left(\rho\frac{v^2}{2} + \frac{B^2}{2} + \frac{p}{\gamma-1}\right)\ d^3x = -\int_S \left[\left(\rho\frac{v^2}{2} + \frac{p}{\gamma-1}\right)\mathbf{v} + p\mathbf{v} + \mathbf{E}\times\mathbf{B}\right]\cdot d\mathbf{S}. \tag{2.34}$$

The different contribution to the energy are shown in the right hand side of the equation: kinetic and thermal energy flux, work done by the pressure force and Pointing flux. It follows that energy is conserved if either $v_n = B_n = 0$ or $\mathbf{v} = 0$ at the boundary. Finally, from eq. 2.34, we can derive the variation of total energy W in a volume $V(t)$ co-moving with the fluid:

$$\frac{dW}{dt} = -\int_S (\mathcal{T}\cdot\mathbf{v})\cdot d\mathbf{S}. \tag{2.35}$$

The ideal MHD is characterized by the so called “frozen in” condition. The magnetic field is frozen in the plasma flow. This property has been firstly explained by Alfvén, and is based on two important theorems.

Theorem 1. *In ideal MHD, the magnetic field lines or, more precisely, the field* $\boldsymbol{B}/\rho$*, are transported by the flow.*

In other words, the transformation generated by the flow maps the field $\mathbf{B}/\rho$ and its lines at time t_0 to the field $\mathbf{B}/\rho$ at time t. Such transformation is a map $\Psi_{t't}$ of the physical space onto itself, which links any point $M(x)$ at every time t with a point $M'(x')$ at time $t' : x' = \Psi_{t't}(x)$. Let’s consider now a vector field $V(x,t)$. On one hand, the definition of vector field allows to find $V(x',t')$, defined on M' at t'. On the other hand, using the transformation $\Psi_{t't}$, one can construct the vector $V'(x',t')$, also defined on M' at t'. If $V = V'$ for any given point and at any given time, then the vector field V is transported by the flow.

The implications of this theorem are mainly twofold. First, the magnetic topology is preserved. Imagine to define a magnetic surface. Usually this kind of surface is related to a particular symmetry in the problem. For example, in a vertical axially symmetric flow, one can naturally define surfaces preserved by rotation around the axis, and label each surface by the value of magnetic flux through the surface defined by an horizontal cut at a certain height h. These surfaces, in general, have a distinct topology: so, for example, they may be isomorphic to a sphere, or to a torus, or to other kind of surfaces, and they keep the same isomorphism in time. In nature, however, changes in topology are allowed and observed. The magnetic field lines are stretched, teared apart, and reconnected to form new surfaces. It is important to notice that these phenomena, called reconnection events, are not following ideal MHD.

Second, when the magnetic field is weak, the field lines are basically dragged by the flow, so they are easily deformed . Conversely, when the magnetic field is strong, the flow tends to follow the field lines without affecting their shape heavily.

Theorem 2. *In ideal MHD, the magnetic flux across a surface delimited by a closed contour is constant when the contour is deformed by the flow transformation.*

Consider a closed contour γ. After a time dt, the flow transformed it in γ'. The two contours, together, form a closed surface, similar to a tube. The variation in time of the flux is due to the modification in time of the magnetic field, and to the flux across the band generated by the displacement. The surface element of this band is therefore $\mathbf{v}dt \cdot d\mathbf{l}$, where $d\mathbf{l}$ is the infinitesimal line element on γ. It follows that the time derivative of the flux is:

$$\frac{d\Phi}{dt} = \int \partial_t \mathbf{B} \cdot d\mathbf{S} + \int \mathbf{B} \cdot (\mathbf{v} \times d\mathbf{l}) \,. \tag{2.36}$$

The first term on the right hand side can be rewritten if we take the surface integral of the induction equation (2.11):

$$\int_S \partial_t \mathbf{B} \cdot d\mathbf{S} = \int (\mathbf{v} \times \mathbf{B}) \cdot d\mathbf{l} = -\int \mathbf{B} \cdot (\mathbf{v} \times d\mathbf{l}) \,. \tag{2.37}$$

Substituting eq. 2.37 into eq. 2.36, one finds:

$$\frac{d\Phi}{dt} = 0. \tag{2.38}$$

The conservation of magnetic flux further explains the fact that magnetic field lines are frozen to the fluid, because they can be considered as flux tubes of infinitesimal diameter.

2.1.4 Validity limits and non ideal effects

The MHD equations are valid under the assumption that the particles in the plasma can be treated collectively as a fluid. This translates in the requirement that electrons and ions must be collisionally dominated. Indeed, with a sufficient number of collisions, each particle remains reasonably close to its neighboring particles during the timescale of interest. Therefore, the plasma can be divided into small fluid elements and the physics of the system is described correctly.

One important consequence of considering collisional plasmas regards the pressure tensor $\mathcal{P}$. If the collisions happen on a time scale smaller than any other time of interest in the system, then the distribution functions are rapidly randomized, producing an isotropic scalar pressure. It is interesting to note that, in general, the description of the evolution of $\mathcal{P}$ in problems involving equilibrium and stability is not crucial for the physics. This feature explains why ideal MHD can be used to obtain very good predictions even outside its regimes of validity.

To obtain the conditions of validity for ideal MHD it is useful to define some quantities related to the plasma. Since in this treatment the point of interest is the macroscopic behavior of the fluid, the relevant length scale corresponds to the physical extent of the plasma, denoted by a. The plasma time scale corresponds to the ion thermal transit time across a, and is defined by a/v_{T_i}, with $v_{T_i} = (2T_i/m_i)^{1/2}$. In addition, a characteristic plasma frequency ω and wave number k can be defined: $\omega \sim v_{T_i}/a$ and $k \sim 1/a$. Note, then, that $v_{T_i} = \omega/k$.

The plasma must fulfill two conditions for the validity of the fluid approximation. The first requires that enough collisions take place so that the particles distribution function approaches a Maxwellian. For ions, the dominant collision mechanism is the ion-ion interaction, with a collision time τ_{ii}. For electrons, however, collisions with both ions and electrons are important. Nevertheless the two collision times are similar. The requirement is that the plasma time scale is much bigger than the collision times. For the second condition, the plasma length scale (or the typical gradient scales) must be much bigger than the mean free path λ_c of the particles. The two conditions are basically equivalent and can be summarized as:

$$\frac{v_{T_i}\tau_{ii}}{a} \sim \frac{v_{T_i}\tau_{ee}}{a} \ll 1. \tag{2.39}$$

The mean free path for hot plasmas can become very long, since $\lambda_c \propto T^2$, where T is the temperature. It is therefore possible for astrophysical plasmas to violate this condition. A notable example is the solar wind. It has to be noted, however, that magnetized plamas have usually a shorter effective mean free path. In the direction perpendicular to the field lines, the movement of the particles is limited by the gyroradius, usually very small. In addition, the gradients in the direction parallel to the field are weaker than in the perpendicular direction, softening the requirements to apply the fluid approximation.

Deviations from the ideal MHD approximation take the form of dissipative effects and are represented by different kind of diffusion processes. In the equation of motion (2.5), for example, the ion viscous force must be considered. This can be done through the divergence of the stress tensor, which is usually strongly anisotropic. This term is frequently replaced by a scalar kinematic viscosity ν, so that the equation of motion reads:

$$\rho\left(\partial_t \mathbf{v} + \mathbf{v} \cdot \nabla \mathbf{v}\right) = -\nabla p + \mathbf{j} \times \mathbf{B} + \rho \nu \nabla^2 \mathbf{v}. \tag{2.40}$$

In general, this approximation is justified because the results are quite insensitive to the particular form or magnitude of the viscous term. In addition, resistive effects are generally more important (see below). Moreover, condition 2.39 proves to be sufficient in order to neglect viscosity in the momentum equation.

Important dissipation effects involve mainly correction terms to Ohm's law. Assuming that they are dependent on the current density, we can make a Taylor expansion as follows:

$$\mathbf{E} + \mathbf{v} \times \mathbf{B} = \eta_1 \mathbf{j} - \eta_2 \nabla^2 \mathbf{j} + \cdots , \tag{2.41}$$

where we consider only even-order differential operators, since they are the only ones to contribute to dissipation. The coefficient are in general tensors that take into account the anisotropies of the system, but in the case of η_1 the difference between $\eta_\perp$ and $\eta_\|$ is just of order 2. For convenience then, we can assume a scalar resistivity η, uniform in space, considered also in the sense as magnetic diffusivity. The second term, η_2, is often referred to as hyper-resistivity. It is related to perpendicular electron viscosity and is in general quite small. This term, however, can become important in some cases. If only the resistive term in eq. 2.41 is considered, one can obtain the induction equation in the form showed previously in eq. 2.10, where $\eta = 1/\sigma$. Furthermore, if the dissipation effects are dominant, the induction equation reduces to a diffusion equation:

$$\partial_t \mathbf{B} = \eta \Delta \mathbf{B}. \tag{2.42}$$

In this conditions, the magnetic field diffuses into the plasma and smooths itself, tending to become homogeneous as a consequence of current dissipation. To be able to neglect this term, on the other hand, the plasma spatial scale must be large enough so that the diffusion time scale is much greater than the characteristic MHD time scale.

Several dimensionless quantities can be used to quantify the importance of the dissipative effects described above. The ratio of the average of the flow and viscous terms in eq. 2.40 leads to the Reynolds number Re, while the ratio of magnetic advection and diffusion terms in eq. 2.10 gives the magnetic Reynolds number R_m:

$$\frac{\langle|\mathbf{v} \cdot \nabla \mathbf{v}|\rangle}{\langle|\nu \nabla^2 \mathbf{v}|\rangle} \sim \frac{vL}{\nu} = Re, \tag{2.43}$$

$$\frac{\langle|\nabla \times (\mathbf{v} \times \mathbf{B})\,|\rangle}{\langle|\eta \nabla^2 \mathbf{B}|\rangle} \sim \frac{vL}{\eta} = R_m, \tag{2.44}$$

where v is a typical flow velocity and L is a global scale length. In the case of static configurations, and particularly for growth rates of resistive instabilities, one can measure the magnitude of resistive effects using the Lundquist number $S = v_A L/\eta$ instead of the magnetic Reynolds number. Here, v_A is the Alfvén velocity (see next section). Finally, to quantify the relative importance of momentum and magnetic diffusivity, the magnetic Prandtl number is employed:

$$Pr_m = \frac{R_m}{Re} = \frac{\nu}{\eta}. \tag{2.45}$$

Few examples for Pr_m include the base of sun's convection zone ($Pr_m \simeq 10^{-2}$) and planets interior or liquid metal laboratory dynamos ($Pr_m \simeq 10^{-5}$). In astrophysical jets, the Reynolds number is generally high, with values of about 10^7 for YSO jets, and 10^{28} for extragalactic jets.

2.2 Instabilities

Astrophysical jets propagate to large distances, as far as several hundreds of jet radii. Even if their physical state is in equilibrium, a number of plasma instabilities can affect the propagation of the flow. In particular, the KH instability is very dangerous for the jets because it is proper of sheared flows in general, and its effect is a disruptive mixing of jet and ambient material.

In this section we will describe the main theoretical and analytic tools to study the stability of astrophysical jets, namely the linear analysis, and we will present few important applications.

2.2.1 Definition and mathematical approach

In order to study the stability of plasmas, the starting point is the behavior of small perturbations applied to the system. Stability is found when such infinitesimal disturbances relax and decrease in size. More correctly, the system is conditionally stable, because other forms of larger perturbations might grow instead. On the other hand, the system is unstable when the perturbations tend to increase their size and affect the character of the flow.

The plasma can be found in several different states, described well by the mechanical analogous of fig. 2.1. Imagine to apply a small displacement to the ball, initially at rest. In panel *a*, the ball will start to oscillate around the starting point, if we assume that no dissipation effects are present. The ball does not come back to its original position, but is always close to it. The system can be considered stable. In panel *b*, conversely, the ball will move away from the original position indefinitely. The system is clearly unstable. The configuration depicted in panel *c* describes neutral or marginal stability, because the small displacement will not cause the ball to either roll further away or to oscillate around the initial position. Usually, this kind of state changes easily to stable or unstable with a slight variation of the physical parameters describing the system.

We can visualize the effects of dissipation by immersing the ball in a viscous fluid. In panel *d* the oscillations are damped and the ball will eventually return to the equilibrium position. Panel *e* shows that, even if dissipative effects can slow down the motion of the ball, in general they cannot transform an unstable configuration into a stable one. The system in panel *f* is linearly stable, but non-linearly unstable, while the system in panel *g* is linearly unstable, but non-linearly stable.

When a plasma is unstable, therefore, it may undergo two different scenarios. Either the flow is completely disrupted, and a turbulent regime sets in, or a new steady flow condition is reached, if the growth of the instability is limited by non-linear effects. A plasma can pass through a number of intermediate meta-stable states before reaching its final configuration.

Mathematically, the problem of fluid stability is treated with linear stability analysis. In this technique, all the physical quantities Q are expressed by the sum of an unperturbed term Q_0, and a small perturbation Q_1. This expansion is used in the ideal MHD equations. In the subsequent equations, terms of second and higher order in the perturbations are neglected, thus deriving the linearized MHD equations. Then it is assumed that the perturbations can be written in the form

$$Q_1 \approx e^{i(\mathbf{k}\cdot\mathbf{r}-\omega t)}. \tag{2.46}$$

At this point the method requires the derivation of the dispersion relation:

$$\mathcal{D}\left(\omega,\mathbf{k}\right) = 0. \tag{2.47}$$

The stability properties of the flow are determined by the behavior of the complex angular frequency (ω) or wavevector ($\mathbf{k}$) roots of eq. 2.47. Assuming a real ω, then $\mathbf{k}$ is complex. If the imaginary part of $\mathbf{k}$ is negative, the solution represents (spatially) decaying perturbations. Conversely, if the imaginary part of ($\mathbf{k}$) is positive, the solution represents (spatially) growing perturbations with growth length $\lambda_e = -1/\mathrm{Im}(\mathbf{k})$. In this case, the system is characterized by spatial instability. On the other hand, assuming $\mathbf{k}$ to be real, then ω must be complex. Solutions with a negative imaginary part of ω indicate the presence of temporal instability with a growth time $\tau_e = 1/\mathrm{Im}(\omega)$, while solutions with positive $\mathrm{Im}(\omega)$ represent decaying perturbations. In the next sections we will address the question whether to use one approach or the other.

A first classification of instabilities divide them in two groups: micro-instability and macro-instability. The micro-instabilities affect the distribution function of the particle species in the plasma, are confined to small scales, and are not described by the fluid approximation. On the other hand, macro-instability are described by the fluid equations and tend to affect the flow on typical relevant scales of the whole system (the beam radius in a jet, for example). Relevant macro-instabilities for astrophysical plasmas and jets are, among others: the Kelvin Helmholtz instability, the Rayleigh Taylor instability and the current driven instability. The Kelvin Helmholtz instability occurs at the interface between two fluids in relative motion. If a ripple is formed at the interface, the fluid overcoming it flows faster, following Bernoulli's equation, and therefore exerts less pressure. As a consequence the ripple tends to grow. The Rayleigh Taylor instability occurs when plasma is in an accelerated frame or in a gravitational field, and a dense fluid is on top of lower density fluid. The configuration causes "finger like" structures to form from the dense fluid and extend into the lower density one. The current driven instability acts on cylindrical plasma beams to reduce the magnetic energy density, and is normally associated with the presence of toroidal magnetic fields. It can be divided into pinching and kinking modes. The pinch mode deforms the beam with periodic diameter increase and decrease, and is therefore also dubbed as "sausage" mode. The kink mode displaces the beam sideways, giving it a helical shape.

The method described here depends strongly on the assumption of discrete modes with distinguishable eigenfrequencies. This is not true in general, but usually the presence of continua is confined in the stable part of the spectrum, thus allowing a consistent study of the instabilities. Moreover, the perturbations are required to be small compared to the unperturbed quantities, $Q_1 \ll Q_0$. Since, in case of instability, the perturbations grow exponentially in time, this condition limits the validity of the analysis to the growth phase of the instability. Therefore, what can be predicted is at most the scale and type of structures that might develop as the instability saturates. The analysis can be extended in principle to the non-linear stage, but it is often extremely complicated. The accepted common approach then, is to solve numerically the MHD equation.

2.2.2 MHD waves

As a first application of the methods described above, it is useful to describe the waves in a magnetized plasma. We assume that the plasma is initially at rest, $\mathbf{v}_0 = 0$. As stated before, all the physical quantities are expressed as $Q = Q_0 + Q_1$, where Q_0 is defines the equilibrium, and Q_1 is a small perturbation. The MHD equations are then linearized about the equilibrium Q_0:

$$\begin{aligned}
\rho_0 \partial_t \mathbf{v}_1 &= -\nabla p_1 + (\nabla \times \mathbf{B}_1) \times \mathbf{B}_0 + (\nabla \times \mathbf{B}_0) \times \mathbf{B}_1 + \nu \nabla^2 \mathbf{v}_1, && (2.48)\\
\partial_t \mathbf{B}_1 &= \nabla \times (\mathbf{v}_1 \times \mathbf{B}_0) + \eta \nabla^2 \mathbf{B}_1, && (2.49)\\
\partial_t p_1 &= -\mathbf{v}_1 \cdot \nabla p_0 - \gamma p_0 \nabla \cdot \mathbf{v}_1, && (2.50)\\
\partial_t \rho_1 &= -\nabla \cdot (\mathbf{v}_1 \rho_0). && (2.51)
\end{aligned}$$

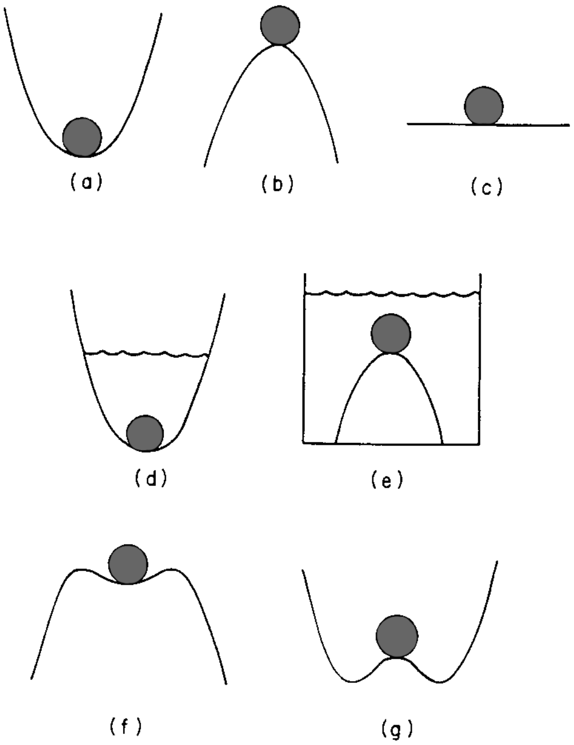

Figure 2.1. Mechanical analogs of various plasma configurations. Taken from Freidberg (1987).

Neglecting non-ideal effects, so that ν, $\eta \rightarrow 0$, eq. 2.48-2.51 are reduced to one equation for the displacement vector ξ, defined by $\mathbf{v}_1 = \partial_t \xi = \dot{\xi}$. $\mathbf{B}_1$, p_1 and ρ_1 can be expressed as a function of ξ after the integration of eq. 2.49, 2.50 and 2.51:

$$\begin{aligned} \mathbf{B}_1 &= \nabla \times (\xi \times \mathbf{B}_0), & (2.52) \\ p_1 &= -\xi \times \nabla p_0 - \gamma p_0 \nabla \cdot \xi, & (2.53) \\ \rho_1 &= -\nabla \cdot (\xi \rho_0), & (2.54) \end{aligned}$$

and can be inserted into eq. 2.48 to obtain:

$$\begin{aligned} \rho \ddot{\xi} &= \mathbf{F}(\xi) \qquad (2.55) \\ &= (\nabla \times \mathbf{B}_1) \times \mathbf{B} + (\nabla \times \mathbf{B}) \times \mathbf{B}_1 + \nabla (\xi \cdot \nabla p + \gamma p \nabla \cdot \xi), \end{aligned}$$

where we dropped the subscript zero for the equilibrium quantities. Equation 2.55 represents the evolution in time of the perturbation. It is an initial value problem, which requires $\xi(x,0)$ and $\dot{\xi}(x,0)$ as initial conditions, and must be coupled with appropriate boundary conditions. Instead of solving the problem in this formulation, it is more practical to determine the normal modes of the system. Using the fact that the equation is linear and the equilibrium is stationary, we are allowed to express the displacement vector as $\xi \propto \exp(-i\omega t)$. Equation 2.55 then becomes:

$$-\rho\omega^2\xi = \mathbf{F}\left(\xi\right). \tag{2.56}$$

In general, it is not possible to always find a solution for any arbitrary value of ω^2, because of the imposition of the boundary conditions. Therefore, eq. 2.56 has to be considered as an eigenvalue problem, with eigenvalues ω^2 and eigenfunctions ξ. The equilibrium and the boundary conditions determine the spectrum, that is the set of allowed values of ω^2. Once both the spectrum and the relative eigenfunctions are known, the solutions to the initial value problem can be retrieved by an expansion of the perturbations with the eigenfunctions.

For the calculation of the MHD waves, we consider the simplest possible equilibrium: a uniform plasma. The quantities p, ρ and B are constant, and the magnetic field is directed along the z direction. We can assume $\xi = \xi_0\ \exp(i\mathbf{k}\cdot\mathbf{x})$. The choice of an opportune coordinate system allows us to consider the wave vector $\mathbf{k}$ laying on the $(x$,$y)$ plane:

$$\mathbf{k} = k_\perp\mathbf{e}_y + k_\parallel\mathbf{e}_z, \tag{2.57}$$

where the subscripts $\perp$ and $\parallel$ refer to the equilibrium magnetic field. With these conditions, eq. 2.55 can be rewritten in components as follows:

$$\begin{aligned} \left(\omega^2 - k_\parallel^2V_A^2\right)\xi_x &= 0, & (2.58)\\ \left(\omega^2 - k_\perp^2V_S^2 - k^2V_A^2\right)\xi_y - k_\perp k_\parallel V_S^2\xi_z &= 0, & (2.59)\\ -k_\perp k_\parallel V_S^2\xi_y + \left(\omega^2 - k_\parallel^2V_S^2\right)\xi_z &= 0. & (2.60) \end{aligned}$$

Here, $V_A = B_0/\sqrt{\rho}$ is the Alfvén speed, $V_S = \sqrt{\gamma p/\rho}$ is the sound speed, and $k^2 = k_\perp^2 + k_\parallel^2$. This homogeneous system of equations has solutions only if the determinant vanishes, which allows us to derive the dispersion relations:

$$\begin{aligned} \omega^2 &= k_\parallel^2V_A^2, & (2.61)\\ \omega^2 &= \frac{k^2}{2}\left(V_A^2 + V_S^2\right)\left[1 \pm \sqrt{1-\alpha^2}\right], & (2.62) \end{aligned}$$

where

$$\alpha = 4\frac{k_\parallel^2}{k^2}\frac{V_A^2V_S^2}{\left(V_A^2 + V_S^2\right)^2}. \tag{2.63}$$

The dispersion relation has three branches. Since $0 \leq \alpha^2 \leq 1$, the imaginary part of ω is zero and all the modes are stable, representing pure oscillations. The equilibrium does not have any source of free energy to feed instabilities, so this result is not surprising. In the dispersion relation, the angular frequency ω appears only squared, so each branch represents two waves propagating in opposite directions.

The first branch, $\omega_A^2 = k_\parallel^2V_A^2$, defines the so called shear Alfvén wave. Since ω does not depend on $k_\perp$, the wave can be strongly localized to certain field lines. The mode is polarized in such a way that the perturbations in velocity and magnetic field are perpendicular to the equilibrium magnetic field and **k**. As a result, the wave is purely transverse and produces bending of the field lines. The other physical quantities are unperturbed, ρ_1, $p_1 = 0$, and the mode is incompressible ($\nabla \cdot \mathbf{v}_1 = 0$). In final analysis, the wave represents an oscillation between perpendicular kinetic energy and perpendicular "line bending" magnetic energy, therefore a balance between inertia and field line tension.

The second branch corresponds to the + sign in eq. 2.62, and is called fast magnetosonic wave, ω_f^2. The mode is compressible, so in general both $\nabla \cdot \mathbf{v}_1$ and p_1 are not zero, and the magnetic field perturbation has both a parallel and perpendicular component. The term "fast" is used because it can be shown that $\omega_f^2 \geq \omega_A^2$. More rigorously, $V_A^2 + V_S^2 \geq \omega_f^2/k^2 \geq \max(V_A^2,V_S^2)$. The first equality sign is achieved when $k_{\parallel=0}$, while the second when $k_\perp = 0$. The first case represents a longitudinal wave, $\xi \parallel \mathbf{k}$, characterized by magnetic compression, since the magnetic perturbation is parallel to the equilibrium field. The second case, valid for parallel propagation, is described by

$$\omega_f^2 = \frac{k^2}{2}\left(V_A^2 + V_S^2 + |V_A^2 - V_S^2|\right), \tag{2.64}$$

and is subsequently divided into two cases. If $V_A^2 < V_S^2$, then $\omega_f^2 = k^2 V_S^2$, and the mode reduces to the longitudinal non-magnetic sound wave. Conversely, if $V_A^2 > V_S^2$, the mode coincide with the shear Alfvén wave. In general, though, the wave vector forms an angle θ with the equilibrium field, therefore the polarization is mixed. In the limit of strong magnetic fields, $\beta \ll 1$, the wave becomes a compressional Alfvén wave, with $\omega_f^2 \approx (k_\perp^2 + k_\parallel^2)V_A^2$, and it can be shown that the compression is mainly present in the magnetic field.

The third branch, finally, corresponds to the − sign in eq. 2.62, and is called slow magnetosonic wave, ω_s^2. This mode is characterized by $\omega_s^2 \leq \omega_A^2$, and is compressible like the fast magnetosonic wave. For $k_\parallel = 0$, ω_s^2 vanishes, and the mode is purely longitudinal, although there is no restoring force. When $k_\perp = 0$, for parallel propagation, the dispersion relation becomes:

$$\omega_f^2 = \frac{k^2}{2}\left(V_A^2 + V_S^2 - |V_A^2 - V_S^2|\right). \tag{2.65}$$

Therefore, in the case $V_A^2 > V_S^2$, we have longitudinal polarization and $\omega_f^2 = k^2 V_A^2$, while in the case $V_A^2 < V_S^2$, we have transverse polarization and $\omega_f^2 = k^2 V_S^2$. This behavior is exactly the opposite as the fast magnetosonic wave. In the limit of strong magnetic fields, the mode is essentially parallel to the field and the dispersion relation becomes independent from $k_\perp$: $\omega_s^2 = k_\parallel^2 V_A^2$. For weak magnetic fields, corresponding to high β, the plasma motion is incompressible and the dispersion relation $\omega_s^2 = k_\parallel^2 V_S^2$ is again independent from $k_\perp$. In these limiting cases the slow magnetosonic wave is similar to the shear Alfvén wave, because it can be localized to specific field lines.

2.2.3 The energy principle

As mentioned before, eq. 2.56 represents the normal mode formulation of the linearized MHD stability problem, and it can be solved as an eigenvalue problem for the eigenvalue ω^2. When the initial equilibrium is static, the force operator $\mathbf{F}$ is self adjoint, any eigenvalue ω^2 is real, and the problem has a useful and simple formulation to test linear stability known as energy principle. Indeed, it can be found that

$$\omega^2 = \frac{\delta W(\xi^*, \xi)}{K(\xi^*, \xi)}, \tag{2.66}$$

where δW represents the change in potential energy associated with the perturbation, therefore the work done against the force $\mathbf{F}(\xi)$ to displace the plasma by ξ, and K is proportional to the kinetic energy. Because of total energy conservation, it can be derived that an equilibrium is stable if and only if:

$$\delta W(\xi^*, \xi) \geq 0 \tag{2.67}$$

for all the possible displacements ξ (compatible with the boundary conditions of the problem). The potential energy can be cast in an intuitive form containing five terms. Three of them are always positive, therefore stabilizing, and represent the source of potential energy for the shear and compressional Alfvén waves, and for the sonic wave. The remaining two can be destabilizing. One is proportional to pressure gradients, while the other is proportional to the current parallel to the unperturbed magnetic field. This is the origin of pressure and current driven instabilities.

The most unstable pressure driven instabilities are internal modes with very short wavelengths perpendicular to the initial magnetic field, but long wavelengths parallel to the field. They are generally divided into interchange and ballooning modes. The interchange modes are special modes which tend to minimize the line bending terms in the potential energy δW, and are excited by interchange of two flux tubes in a zone of unfavorable curvature (where curvature and pressure gradients have the same sign). Ballooning modes are present in plasmas with alternated zones of favorable and unfavorable magnetic line curvature. They are excited by perturbation varying in such a way that the mode is concentrated in the unfavorable curvature region. Therefore they can be more unstable than the interchange modes.

In general, current driven modes have long parallel wavelengths, typically with azimuthal wave number $n = 1$, thus producing a kink deformation (see below). The modes tend to minimize the line bending. They are divided into external and internal kink, depending on the location of the singular surface. Generally the external modes are stronger and determined more by the total current itself rather than by the particular current profile.

2.2.4 Kelvin Helmholtz instability of plasma beams

The linear study of stability in a plasma, as described in sec. 2.2.1 and 2.2.2, starts from the definition of an unperturbed state in equilibrium, which satisfies the MHD equations. This task is not always trivial, since no general solution for the system of MHD equations is known. Particular care has to be put in the choice of the model of plasma beams, in order to give it as much flexibility as possible, but keeping it at the same time simple enough so that the calculation of the dispersion relation is feasible.

Jets are in general conical, but the very small opening angle allows us to to consider them as cylinders. The choice of cylindrical coordinates (r,θ,z) seems then appropriate. A simple configuration that satisfies the MHD equation is a steady, non rotating, cylindrical beam, defined by:

$$\rho_0 = \rho(r), \tag{2.68}$$

$$\mathbf{v}_0 = (0,\, 0,\, v_z(r))\,, \tag{2.69}$$

$$\mathbf{B}_0 = (0,\, B_\theta(r),\, B_z(r))\,. \tag{2.70}$$

The quantities $\rho(r)$, $v_z(r)$, $B_\theta(r)$ and $B_z(r)$ are arbitrary functions of the distance r from the jet axis. The pressure is computed from the force balance in the direction perpendicular to the jet axis (r):

$$\frac{dp_0}{dr} = -\frac{B_\theta}{r}\frac{d}{dr}\left(rB_\theta\right) - B_z\frac{dB_z}{dr}. \tag{2.71}$$

Formally, the model of beam defined by eq. 2.68, 2.69, and 2.70 assumes that a single function can describe the radial behavior of the physical quantities. In practice, it is very useful to make a further simplification and assume three different regions in the domain: the external medium, the sheared flow, and the beam core. The physical quantities are uniform in the beam core and in the external medium. The values are matched by the sheared flow region, which is the only one to contain gradients of the variables. It is required that the physical quantities are continuous at the interface of these three zones: position R_a, at the interface between ambient medium and sheared flow, and R_b, at the interface between beam core and sheared flow.

In analogy to the discussion done in sec. 2.2.1 and 2.2.2, we can proceed to the linearization of the MHD equations, using the properties of the beam model examined. Again, the resulting equations are homogeneous in the perturbations, but they result too complex to be solved as they are. In this case, the analysis must rely on assumptions that simplify the functions $\rho(r)$, $v_z(r)$, $B_\theta(r)$ and $B_z(r)$ describing the model.

The next step in the analysis consists in decomposing the perturbations into wave-like eigenfunctions, that in cylindrical coordinates can be written as follows:

$$Q_1 = Q_1(r)e^{i(kz+n\theta-\omega t)}. \tag{2.72}$$

The meaning is that the modes of the instability are wavelike in z with wave number k, wavelike in time with angular frequency ω, and "wavelike" in θ, because they produce $|n|$ oscillations around the circumference of the beam. The radial part of the perturbation describes the localization of these waves in the domain. The dispersion relation depends on n and can be solved either in a spatial (real ω) or in a temporal (real k) approach. The choice largely depends on the type of instability one wants to study. For absolute instabilities, which grow at fixed points in space, the temporal approach is preferable. On the other hand, convective instabilities, which grow in the rest frame of the flow, but decrease at fixed points because are advected by the flow, are better described by a spatial approach. The KH instability is advected at half of the flow speed, in the case of subsonic or transonic flows, with no density gradient between the two fluids. Since the stability of a plasma beam is heavily affected by the KH modes, a spatial approach to solve the dispersion relation is used here. For each value of n, the dispersion relation yields a solution, or a family of solutions, $k(\omega)$ with similar azimuthal characteristics.

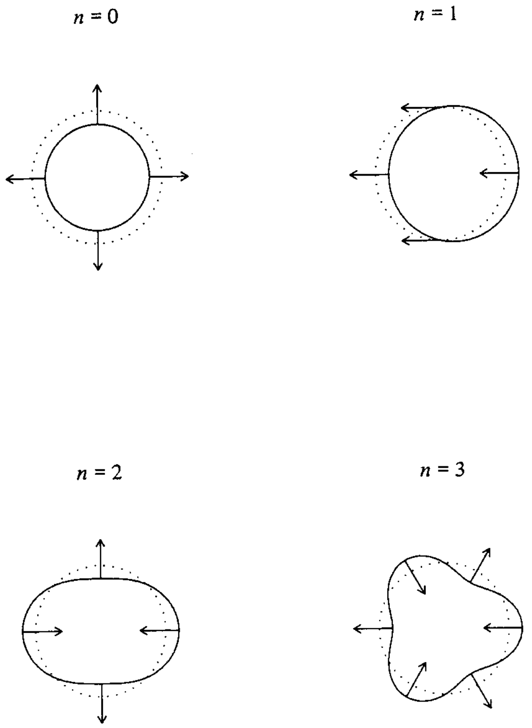

Figure 2.2. Section of the beam in the (r, θ) plane as deformed by the KH instability with azimuthal mode number $n = 0$, 1, 2, and 3. The dotted line represents the unperturbed beam boundary, while the solid line represents the deformation of the boundary due the instability. Taken from Birkinshaw (1991a).

The section of the beam is shown in fig. 2.2 for the cases $n = 0$, 1, 2, 3. The mode with azimuthal mode number $n = 0$ is called "pinch" mode. The effect on the beam is a coherent contraction or expansion of the beam radius at any z. Note that this is the only mode that changes the area of the beam section. In the case $n = \pm 1$, the whole beam is displaced sideways and assumes a helical shape along z. This mode is therefore known as "helical" or "kink", and it is the only mode able to displace the beam axis. Finally, modes with $|n| \geq 2$ are called "fluting" or "filamentation" modes. The distortion produces surface oscillations around the circumference of the beam. The azimuthal mode number n represents the number of nodes on the beam surface. The angular frequencies ω of the modes with positive and negative n are degenerate, if the beam is non-rotating and the magnetic field is purely axial.

As stated before, attempts to derive an analytic dispersion relation for the problem is heavily dependent on the choice of initial equilibrium. Most of the configurations for which it is possible to obtain a dispersion relation, are based on the assumption that there are no gradients in the ambient medium or in the beam core regions, and that there is no sheared flow region. In other words $R_a \equiv R_b \equiv R$. This rather idealized configuration allows for an analytical treatment in cases like non-rotating relativistic beams (Ferrari et al. 1981), or non-relativistic uniformly rotating beams (Bodo et al. 1989), both with uniform axial magnetic field. Introducing a toroidal component of the magnetic field, resulting in a helical magnetic topology, often prevents the possibility to derive the dispersion relation, with notable exceptions (beams with zero total net current, as discussed by Appl & Camenzind, 1992). When analytical results are not reachable, one has to rely on numerical calculations.

One example of analytic dispersion relation is found in Birkinshaw (1991b), for magnetized beams without any radial gradient, so that $R_a \equiv R_b \equiv R$:

$$\mathcal{D}\left(\omega,\mathbf{k}\right) = \frac{H_n^{(1)\prime}(\alpha_a R)}{H_n^{(1)}(\alpha_a R)} \cdot \frac{\alpha_a}{\rho_a} \cdot \frac{1}{\omega^2 - K^2 V_{Aa}^2} - \frac{J_n^{\prime}(\alpha_b R)}{J_n(\alpha_b R)} \cdot \frac{\alpha_b}{\rho_b} \cdot \frac{1}{(\omega - k v_b)^2 - k^2 V_{Ab}^2} = 0. \tag{2.73}$$

Here, $H_n^{(1)}(z)$ is a Hankel function of the first kind with order n, $J_n(z)$ is a Bessel function of the first kind with order n, the primes ($'$) denote differentiation with respect to the argument, the subscripts a and b refer to the ambient and the beam respectively, and α are the radial wavenumbers, given by:

$$\alpha = k \left[\frac{\left(1 - \left(\frac{\omega - k v_z}{k V_S}\right)^2\right)\left(\left(\frac{\omega - k v_z}{k V_A}\right)^2 - 1\right)}{1 - \left(\frac{\omega - k v_z}{k V_A}\right)^2 \left(1 + \frac{V_A^2}{V_S^2}\right)} \right], \tag{2.74}$$

with $V_S = V_{Sa}$ or V_{Sb}, $V_A = V_{Aa}$ or V_{Ab} and $v_z = 0$ or v_b for the ambient medium and beam wavenumbers, α_a and α_b respectively. It results that the KH modes are magnetosonic waves partially trapped in the beam cavity.

With an analytical dispersion relation, the analysis proceeds by using some meaningful parameters which describe the unstable modes. Each mode is characterized by a wavelength λ_0, by a growth time τ_e, corresponding to the time needed by the perturbation to grow by a factor e, and by a growth length λ_e, corresponding to the distance traveled along the beam by the mode until it grows by a factor e. While it is useful to refer the growth time in the frame of the beam, where the growth rate of the instability can be the relevant time scale for energy release, λ_0 and λ_e are usually referred to the ambient medium (observer) frame, because they describe the large scale effects of the instability on the beam. This analysis follows the spatial approach in which ω is real and k is complex. As a consequence, the wavelength and growth length of the instabilities are

$$\begin{aligned}
\lambda_0 &= \frac{2\pi}{\mathrm{Re}(k)}, &(2.75)\\
\lambda_e &= -\frac{1}{\mathrm{Im}(k)}, &(2.76)
\end{aligned}$$

so that the perturbations grow with the distance along the beam:

$$|Q_1| \propto e^{z/\lambda_e}. \qquad (2.77)$$

Generally, because of exponential growth, among all the possible unstable modes, the fastest growing mode with λ_0^* and λ_e^* dominates the flow after a short time corresponding to few growth lengths. The aim of the analysis is, therefore, to find in the dispersion relation the values of ω and n for which λ_e is minimum. This value is taken as the fastest growing mode and the properties of the system are then described by n, λ_0^* and λ_e^*.

In general it can be possible that for each value of the azimuthal number n, several branches are present. These branches have been labeled by N, the radial mode number, which represents the number of nulls in the pressure perturbation in $0 < r < R$. The modes with $N = 0$ are called ordinary (or surface) modes. They are a consequence of the presence of a boundary between the beam and the external medium. The modes with $N > 0$ are called reflected (or body) modes. They require more than one planar surface in the beam, and are stronger in the regions of the fluid where there are cavities or regions with walls which can vibrate. Then, sound waves propagate from one surface and are reflected by the other, possibly with a phase delay, and can then interact constructively. These modes appear only for slightly fast beams with $v_b > V_{Sa} + V_{Sb}$.

The results of the spatial analysis by Birkinshaw (1991b), showed that the stability of beams with higher densities is greater than the stability of lower density beams with the same velocity. In addition, the overall stability of a beam is augmented when the Mach number is increased. However, the growth length of the mode $n = 0$ grows faster then theone of the mode $n = 1$. This suggests that kink deformations dominate in very fast jets, while a pinch deformation dominates in low Mach number jets.

Chapter 3

Numerical simulations of a single shear layer

In this chapter we describe the KH instability of a single velocity shear layer. This is the first approximation of the boundary between a jet and the ambient medium. Astrophysical jets are generally regarded as weakly magnetized, therefore we will concentrate on magnetized flows. The orientation and topology of the magnetic field is very important for the behavior of the instability. Our original contribution to the field is the study of the effects of an anti-parallel magnetic field on the KH instability (Bocchi et al., *in prep.*).

A few notes are necessary here. First, in this chapter we limited my calculations to flow Mach numbers fixed to unity. The reason is that single layers are known to be stable for greater Mach numbers (see, for example, Baty et al. (2003)). Second, the study is mainly two-dimensional. I will present some 3D results in the next sections, mainly to confirm the result obtained in 2D and to have a more realistic view of the instability. Finally, all the results described in this chapter are obtained with a temporal approach, suitable to follow and describe the evolution in time of the instability (see Chap. 2). A spatial approach, conversely, is used in the next chapter about jet simulations.

Although a description of the numerical codes we used for my calculations is presented in App. A, it is appropriate to shortly describe here the general ideas behind MHD numerical simulations. First of all, it is important to remember that the MHD equations do not have a general analitic solution, except in cases, where several assumptions are made to simplify the problem. Among such assumptions, two are widely used: self similarity and stationarity. There are now several different methods to solve In a MHD simulation, the computer solves the MHD equation over a volume called domain, spatially discretized into small subvolumes called grid cells or simply grid points. It is an initial value problem, so suitable initial conditions must be provided. Then, the solution is updated for small time intervals called time steps. The size of the time step depends on the CFL condition, that assures numerical stability of the algorithm used for the solution.

3.1 The interface model: Reversed magnetic field configuration

What follows is taken and slightly modified from the scientific paper "Kelvin Helmholtz instability of a magnetized shear flow layer: Effects of a reversed magntic field", Bocchi, M., Baty, H., Camenzind, M., in preparation.

Table 3.1. Summary of parameters and domain type

Domain[a]	M_a	Resistivity	Resolution
SD	2.5	-	200x400, 400x800
SD	3	-	200x400
SD	3.5	-	200x400, 400x800
SD	4, 4.5	-	200x400
SD	5	-	200x400, 400x800
SD	6	-	200x400
SD	7	-	200x400, 400x800
SD	7	-	100x200, 150x300, 250x500, 300x600
SD	7	10^{-4}, 10^{-5}, 10^{-6}	200x400
SD	8, 9	-	200x400
SD	10	-	200x400, 400x800
SD	12, 14, 16, 18	-	200x400
SD	20	-	200x400, 400x800
SD	25, 30, 40, 50, 60, 100	-	200x400
LD	2.5, 7, 20	-	2000x2000
3D	2.5, 7, 20	-	128x256x128

[a] SD, LD and 3D labels refer to "Small Domain", "Long Domain", and "Three-dimensional" respectively.

In all the non-uniform magnetic field simulations, the interface between the jet and the external medium is modelled using a simple hyperbolic tangent profile for the velocity

$$v_x(y) = \frac{V_0}{2} \tanh\left(\frac{y}{a}\right), \tag{3.1}$$

a being the half width of the shear layer. We assume the velocity is embedded in a magnetic field reversing with a similar hyperbolic tangent profile, chosen for the sake of semplification:

$$B_x(y) = -B_0 \tanh\left(\frac{y}{a}\right). \tag{3.2}$$

Both v_y and B_y were initially set to zero. The layer is assumed to be in pressure equilibrium according to the following profile:

$$p(y) = p_1 - \frac{B_x^2(y)}{2} \tag{3.3}$$

where $p_1 = p_0 + B_0^2/2$ is the maximum value of the total pressure (located at the y boundary), and p_0 is the minimum thermal pressure in the domain. In order to have a constant speed of sound $c_s = \sqrt{\gamma p/\rho}$, we impose the following density profile:

$$\rho(y) = \gamma p(y). \tag{3.4}$$

This simplifies the comparison with the uniform magnetic field case. In fact, for selected cases, we additionally performed simulations of individual modes with uniform field, to have direct comparison of the results. In addition, in the 3D simulations we allow variations in the z direction. We keep the same profiles as described above, so initially, the third components of both the velocity and the magnetic fields are set to zero.

Regarding the normalisation, we set both c_s and ρ_0 to unity, and we fix $p_0 = 1/\gamma$. Our velocities are conveniently normalized to the sound speed c_s, and the densities to ρ_0. As length unit we chose the horizontal length of the domain of individual mode simulations (see below). Finally, the time unit is the time required for a sound wave to travel across the domain along the x direction.

In all of our simulations we fix two parameters: the initial Mach number, defined as $M = V_0/c_s$, is set to unity, and the value of the half width of the shear layer is $a = 0.05$. To study the effects of the magnetic fields, we vary the Alfvén Mach number $M_a = V_0/V_a$ in the range [2.5,100]. The magnetic field strength, in fact, is controlled by the Alfvén Mach number, since $V_a = \sqrt{B_0^2/\rho_0}$. Exact values are reported in Table 3.1.

The MHD numerical codes solve the MHD equations inside a spatial domain that has to be determined before the start of the simulations. In 3D cartesian coordinates, a typical domain is defined by the length of its three edges: L_x, L_y and L_z. Generally, the domain is chosen big enough to be able to observe the physical process in question, but for the KH instability one must take extra care for the following reasons. First, the domain along the y direction should be greater than the shear layer and extend far from it. This is done to avoid unwanted effects from the boundary conditions applied. Second, the choice of L_x determines the maximum wavelength of the instability that can be observed in the simulation, that is, the biggest wavelength that can fit in the simulation box. In this way it is possible either to focus on a single mode of the instability , or to study several modes and their interaction.

Keeping this in mind, in the 2D simulations we choose two different computational domains with $0 \leq x \leq L_x$ and $-L_y \leq y \leq L_y$: a short one (called SD in what follows) to study the evolution of one single mode of the instability, and a long one (LD) to observe the pairing mechanism of the KH instability. For the SD we fix $L_x = 1$ and $L_y = 1$, for the LD we have $L_x = 10$ and $L_y = 5$. Regarding the 3D simulations, the 2D domain is extended in the z direction with $0 \leq x \leq L_z$ and is defined by $L_x = 1$, $L_y = 1$ and $L_z = 1$.

3.2 Code and numerical methods

The system of MHD equations is numerically solved with the finite volume code Pluto (Mignone et al. 2007), a software that contains several different algorithms of integration of a system of conservation laws.

The resolution employed in the simulations depends on the domain type. For the SD, we use a resolution of either 200x400 or 400x800 grid cells. The LD has a resolution of 2000x2000 grid cells, and the 3D domain 128x256x128. The different cases are summarized in Table 3.1.

In our study we adopt a temporal approach, reflected in the choice of the boundary conditions. In all the simulations the boundaries are set to periodic in the x direction, and in the y direction the plasma is allowed to flow out of the domain by the usual zero-gradient conditions. The size of the domain in the y direction is chosen large enough in order to avoid unwanted influences on the dynamic of the plasma in the centre of the domain. In addition, in the 3D simulations periodic boundary conditions are also applied in the z direction.

The velocity flow is perturbed by adding different forms of small amplitude transverse velocity. To excite the instability in the case of the individual mode simulations, we used a sinusoidal perturbation in the transverse velocity, decaying with a gaussian profile as the distance from the shear layer increases:

$$v_y(x,y) = \epsilon \cdot \sin(2\pi x) \cdot e^{-y^2/(la)^2}, \tag{3.5}$$

where ϵ is the amplitude of the perturbation and l is its extension in the y direction. Typically we use an amplitude $\epsilon = 0.001$ small compared to the equilibrium flow, and $l = 4$. In the case of the extended domain we used instead a random noise perturbation

$$v_y(x,y) = \epsilon \cdot \mathrm{Rand}(x,y) \cdot e^{-y^2/(la)^2}. \tag{3.6}$$

Here Rand(x,y) is a function that generates random numbers uniformly distributed in the range $[-0.5,0.5]$. This kind of perturbation excites all the possible modes of the instability, and is well suited to reproduce the coalescence mechanism of the KH instability (see Baty et al. 2003). In the 3D simulations, we use for $v_y(x,y,z)$ the same formulation as given in eq. 3.5. In addition, we prescribe a random perturbation for $v_z(x,y,z)$, similar to eq. 3.6, where we substitute Rand(x,y) with Rand(x,y,z).

3.3 Results: 2D individual modes

The simulations of a single mode of the KH instability are best realized fixing the longitudinal extent of the domain, L_x, equal to the wavelenght of the mode in interest, and exciting the instability with a perturbation of the same wavelength. The fastest growing mode of the instability dominates over the others in a realistic plasma configuration (see Chap. 2), therefore it is important to use a L_x as close as possible to this mode wavelength. However, we do not know the wavelength of the most unstable mode in the antiparallel magnetic configuration. Therefore, in order to prepare the MHD numerical simulations, we have computed the linear growth rates of the KH instability for a wide range of magnetic field values.

3.3.1 Stability study

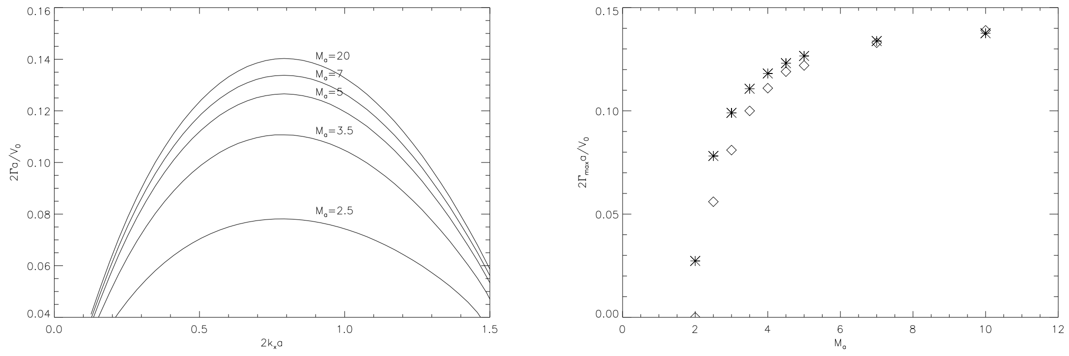

Figure 3.1. *Left panel*: normalized growth rates versus the normalized wave number for different values of the Alfvén Mach number M_a. The sound Mach number M_s is fixed at unity. The results are obtained from the stability study performed with the linear code Ledaflow. *Right Panel*: maximum growth rate versus the Alfvén Mach number M_a. Stars represent data obtained from the stability study performed with the linear code Ledaflow. Diamonds represent results taken from Fig. 5 of Miura & Pritchett (1982). The sound Mach number M_s is fixed at unity.

The calculations have been performed using a stability code, Ledaflow, which is designed to integrate the linearized MHD equations in ideal or resistive form.

The results obtained for our non uniform equilibrium are plotted in Fig. 3.1 (left panel) using normalized units, for different magnitudes of the magnetic field. First, when comparing to results for a uniform magnetic field configuration (Miura & Pritchett 1982, Fig. 4), one can clearly see that the global dependence of the linear growth rate as a function of the wavenumber and of the Alfven Mach number is similar. There are however a number of differences as listed below. First, the maximum growth rate in our study occurs for $k_x a \approx 0.4$ for all the curves, independently of the magnetic field strength. This is not the case for a uniform case where the maximum depends on the magnetic field magnitude. Typically, it is found for k_x in the range [0.25,0.4] with corresponding M_a in the range [2.5,∞]. For strong uniform magnetic fields the wave vector of the fastest growing mode is shifted towards smaller values. This result is important for the further non linear simulations, as taking the same longitudinal periodic length for different magnetic field amplitudes, guaranties that we study the linearly fastest unstable mode in all cases. Second, the growth rates obtained for the non uniform cases are always higher than their uniform counterparts (the magnetic field being given). This is mostly evident from the results plotted in Fig. 3.1 (right panel). This can be explained by the fact that the the magnetic field is zero at the interface in our initial set-up. Consequently, the partial stabilization factor due to the magnetic field tension vanishes at the interface, leading to a higher growth rate compared to a uniform configuration. For the same reason, note also that the non-uniform case remains unstable (with a non zero residual growth rate) for $M_a < 2$, while the uniform case is fully stable. Finally, in the opposit limit of a pure hydrodynamic configuration, the classical value of $2\Gamma a/V_0 = 0.134$ is recovered indepently of the equilibrium, as computed by Keppens et al. (1999).

Our results are consistent with the ones obtained by Keppens et al. (1999) for antiparallel magnetic fields. In addition, however, their results were clearly affected by the presence of a tearing mode contribution to the KH instability, due to the initial discontinuous magnetic profile used in the study.

3.3.2 A test for numerical codes

In the framework of the Jetset network, we were assigned the task to prepare a test to compare different numerical codes. The test, included in Appendix B, is designed to prove a numerical code against the known results described previously. In particular, to pass the test, a numerical code should be able to reproduce the growth rates and the general behavior of the instabililty for different magnetic regimes.

A useful tool to follow the dynamics of the instability is the temporal evolution of various global variables, like energy averaged over the volume or the plasma β (defined as the ratio of thermal over magnetic pressure). In particular we will use the transverse kinetic energy $e_{k,y}$ and magnetic energy $e_{m,y}$, as well as the longitudinal kinetic energy $E_{k,x}$, defined as follows:

$$e_{k,y} = \frac{1}{V_b} \int_{V_b} \frac{\rho V_y^2}{2} dx\ dy, \tag{3.7}$$

$$e_{m,y} = \frac{1}{V_b} \int_{V_b} \frac{\rho B_y^2}{2} dx\ dy, \tag{3.8}$$

$$E_{k,x} = \frac{1}{V_b} \int_{V_b} \frac{\rho V_x^2}{2} dx\ dy, \tag{3.9}$$

where V_b is the volume of the domain chosen for the simulation. These quantities allow us to follow the evolution of the instability in its various phases. They are also used to measure the growth rate of the instability from the simulations.

Indeed, the best method to get the growth rates is to use the temporal evolution of the transverse kinetic energy. We expect the transverse velocity perturbation to grow exponentially with growth rate Γ: $v_y \propto exp(\Gamma t)$. As a consequence we can write the expected evolution of the energy:

$$e_{k,y} \propto v_y^2 \propto e^{2\Gamma t} \tag{3.10}$$

It is useful to plot the energy in a logarithmic scale. As an example we use a uniform field simulation with $M_a = 10$ (see fig. 3.2). In this way, $log(e_{k,y}) \propto 2\Gamma t$. It is therefore sufficient

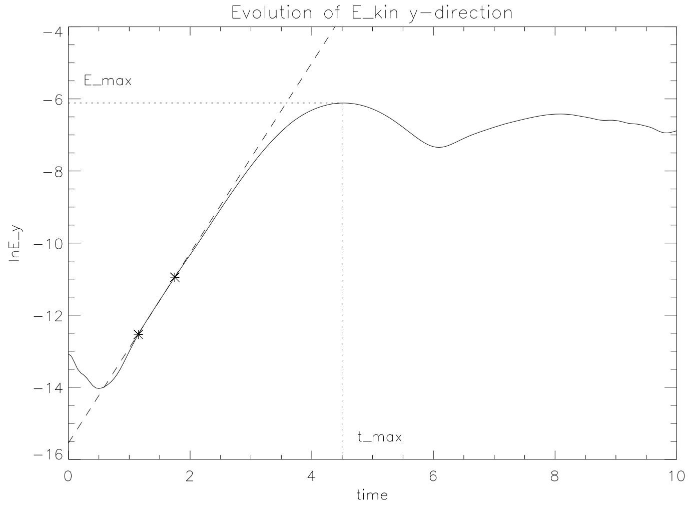

Figure 3.2. Logarithmic plot of the total kinetic energy along the y direction. Also shown are the saturation level E Max and the corresponding time t Max. The growth rate of the instability is obtained from the linear fit in the interval [0.25t Max, 0.4t Max], represented by the dashed line.

to performa linear fit to obtain the wanted growth rate. The only tricky point is to choose a reasonable part of the energy evolution to fit, in order to consider the linear evolution of the instability. Considering the first maximum of the energy E_{max}, which corresponds to the saturation level at time t_{max}, we must stay reasonably far from this point. A good compromise, suggested in Keppens et al. (1999) is to perform the fit in the interval $t \in [0.25t_{max}, 0.4t_{max}]$. The growth rates obtained in this way were in very good agreement with the linear results by Miura & Pritchett (1982).

3.3.3 Linear phase and whole scenario

We now consider the non-linear simulations with the PLUTO code. Because we choose the length of our domain $L_x = 1$ in our units, the wave vector excited by our initial perturbation (eq. 3.5) is $k_x a = 0.314$. As stated in the previous sections, this value is not exactly at the maximum of the dispersion solutions (with a wavevector $k_x a \simeq 0.4$), but it guarantees that the first sub-harmonic that can fit in our box with wave vector $k_x a = 0.628$ has always a lower growth rate than the main excited mode. Moreover, this value is also well suited for simulations in the uniform case, being near the maximum of the growth rates for all the different magnetic field strengths, and allows us to perform easy and direct comparison without the need to change the domain size for each simulation.

As expected by the linear study, we observe an exponential growth of the perturbed quantities (see Fig. 3.3 for the transverse kinetic energy evolution of our representative example $M_a = 7$). The growth rate $2\Gamma a/V_0 \simeq 0.127$ measured in the simulation is in good agreement with the value

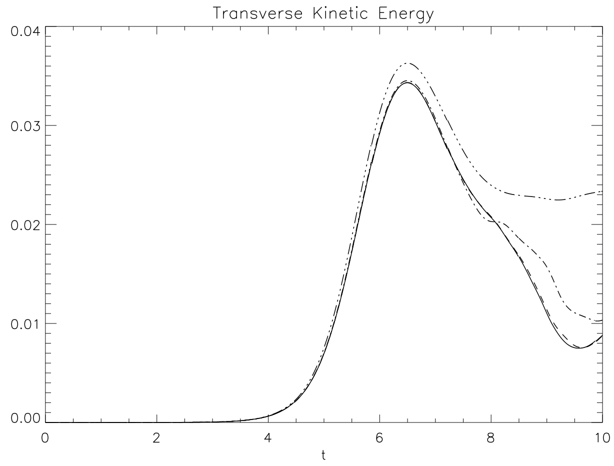

Figure 3.3. Time evolution of the transverse kinetic energy for the case $M_a = 7$, for different values of the explicit resistivity η: 10^{-4} (*upper dash-dotted line*), 10^{-5} (*lower dash-dotted line*), 10^{-6} (*dashed line*), ideal case (*solid line*). Values are normalized over the initial longitudinal kinetc energy.

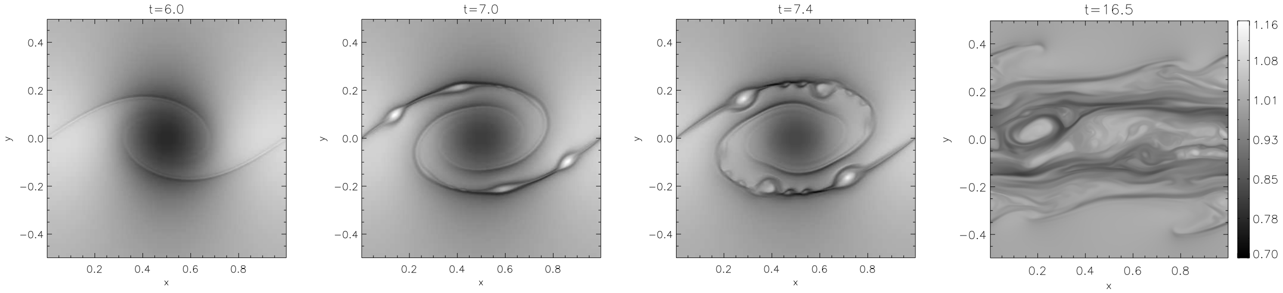

Figure 3.4. Density plots in the case $M_a = 7$ at different stages of the instability. From left to right: 6, 7, 7.4 and 16.5 time units. Only the part of domain with y in the range [−0.5,0.5] is shown.

$2\Gamma a/V_0 = 0.129$ obtained from our linear study (Fig. 3.1). The instability develops into a vortical motion that is able to stretch and compress the field lines around the perimeter of the vortex. The magnetic field is gradually amplified up to the point where the field line tension overcomes the centrifugal force produced by the vortical motion. The transverse kinetic energy reaches its maximum and the instability is saturated. The vortical structure is very similar to the classical Kelvin's cat's eye (see Fig. 3.4, first panel), with the addition of antiparallel magnetic fields and magnetic islands (see Sec. 3.3.4). The transverse magnetic energy (not shown) tends to saturate just after the kinetic energy, when the plasma β reaches a minimum value of order unity (Miura 1984). The flow is subsequently disrupted due to reconnection of field lines (Jones et al. 1997).

The grid resolution used for most of our SD simulations is 200x400 grid cells, which was previously shown to be sufficient to follow the linear and non-linear saturation phases (Keppens et al. 1999, Baty et al. 2003). For $M_a = 7$ we repeated the run with up to 400x800 grid cells in order to check the convergence of our results, in a similar way as shown in Fig. 3 of Baty & Keppens (2006). Moreover, in order to confirm that the resistive effects (see magnetic islands in Fig. 3.4, panels 2 and 3) and the disruption phase are physical features, we have done a resistivity convergence study, using a uniform explicit resistive term η, in the range [10^{-4},10^{-6}]. Fig. 3.3 shows the evolution in time of the transverse kinetic energy for the different values of resistivity. From this plot it is evident that a very good convergence is reached for $\eta = 10^{-5}$, value that we take as our estimation for the numerical resistivity. In addition we confirm the presence of the magnetic islands in the resistive runs.

A very similar scenario also appears in the case of a uniform magnetic field, with few important differences. No magnetic islands are formed around the vortex, and the disruption is characterized by less turbulence. In addition, the final state is very different (a detailed description can be found in Sec. 3.3.6).

3.3.4 Formation of magnetic islands: a driven process

As we described before, the initial phase of the KH instability in our representative non-uniform configuration is apparently very similar to the case of uniform magnetic field with the same M_a. In Fig. 3.4 (first panel), we can see the formation of a sequence of high and low density zones alternated with each other. These patterns are connected by low density filamentary structures. A closer look, however, reveals that these structures are actually formed by two parallel low density stripes in which the magnetic field is slightly enhanced. The direction of the magnetic field in these two stripes is opposite, as a consequence of the initial conditions.

However, in contrast to uniformly magnetized cases (see for example Fig. 3 of Baty et al. 2003), the presence of small magnetic islands along the filamentary vortical structure can be clearly seen in Fig. 3.4, panels 2 and 3. This pattern of 4 initial islands appears at t = 6.6 which is roughly the time at which the transverse magnetic energy reaches a maximum due to the saturation of the instability. Moreover, one must note that even smaller magnetic islands are able to grow in between the previous four ones (see Fig. 3.4, panel 3). Despite the fact that this chain of magnetic islands are short-lived (as they dissapear during the disruption), they probably alter the dynamics of the whole KH development including the evolution of kinetic and magnetic energy, as well as the level of turbulence during the disruption phase. Recall that the magnetic islands are not numerical artifacts, but real physical features, as discussed in Sec. 3.3.3.

A plasma embedded in antiparallel magnetic fields is unstable to natural tearing modes. However we can clearly infer that our observed magnetic islands are formed by a driven process

due to the KH vortical motion. Classical tearing modes are purely resistive instabilities that are expected to grow on a relatively slow time scale. Following Priest & Forbes (2000) and Biskamp (1997), we estimate the linear time τ, and the wavelength of the fastest growing mode

λ_{max} of the tearing instability to be:

$$\tau \simeq \frac{1}{0.6} \cdot (\tau_A \cdot \tau_\alpha)^{1/2}, \tag{3.11}$$

$$\lambda_{max} \simeq \frac{l}{1.4} \cdot \left(\frac{\tau_\alpha}{\tau_A}\right)^{1/4}, \tag{3.12}$$

where l is the shear layer width, $\tau_A = l/v_a$ and $\tau_\alpha = l^2/\eta$ are the Alfvén and resistive diffusion time respectively. Measuring $l \simeq 0.03$ and $v_a \simeq 0.35$ from our simulation at $t = 6$, we find $\tau \simeq 10$ and $\lambda_{max} \simeq 0.2$ in our units. Indeed, the wavelength of the main islands measured directly from the simulation is $\lambda \simeq 0.3$, which is in rather good agreement with λ_{max} for tearing modes. Conversely, the characteristic time scale observed in the simulation is roughly one order of magnitude smaller than the value of τ found previously. This leads us to conclude that the magnetic islands are forced to grow faster than the natural tearing instability. Another argument in favor of the driving mechanism is the saturation of the islands. Indeed, we observe that their measured width is always greater than the local shear layer thickness, in contrast with classical theory which predict a maximum width of order of the layer thickness.

3.3.5 Saturation

During the linear phase, both $e_{k,y}$ and $e_{m,y}$ grow exponentially in time due to the vortical motion of the KH instability (see Fig. 3.5). However, because of magnetic tension effects, the growth of the instability is stopped and both the kinetic and magnetic energies reach a maximum, called saturation level.

Regarding the saturation levels in the case of uniform magnetic fields, we briefly summarize the results of Baty et al. (2003), specifically of their Fig. 2. In the cited paper, the authors explain how the instability changes behavior with the strength of the magnetic field. Four different regimes were found. When $M_a \lesssim 2$ the shear layer is stable due to magnetic tension (stable regime). In the range $2 \lesssim M_a \lesssim 4$ the linear stability analysis predicts instability. The classic KH vortex starts to form but the increase of the magnetic field in the periferic region of it, caused by the vortical motion, prevents the vortex to fully develop. This mechanism thus provides a non-linear stabilization of the layer (non-linear stabilization regime). If $4 \lesssim M_a \lesssim 30$, the vortices are allowed to fully develop and the winding up of the magnetic field lines leads to many reversals in the magnetic fields. After the saturation, the vortices are disrupted by reconnection events (disruptive regime). In this regime the transverse magnetic saturation level as a function of the Alfvén Mach number M_a reaches its maximum (see Fig. 2 of Baty et al. 2003). Finally, for $M_a \gtrsim 30$ the kinetic saturation levels are similar to the hydrodynamic case, and simultaneously the magnetic saturation levels are very low (quasi hydrodynamic regime). After the saturation, the system evolves following a pure resistive-viscous behaviour, which causes slow dissipation.

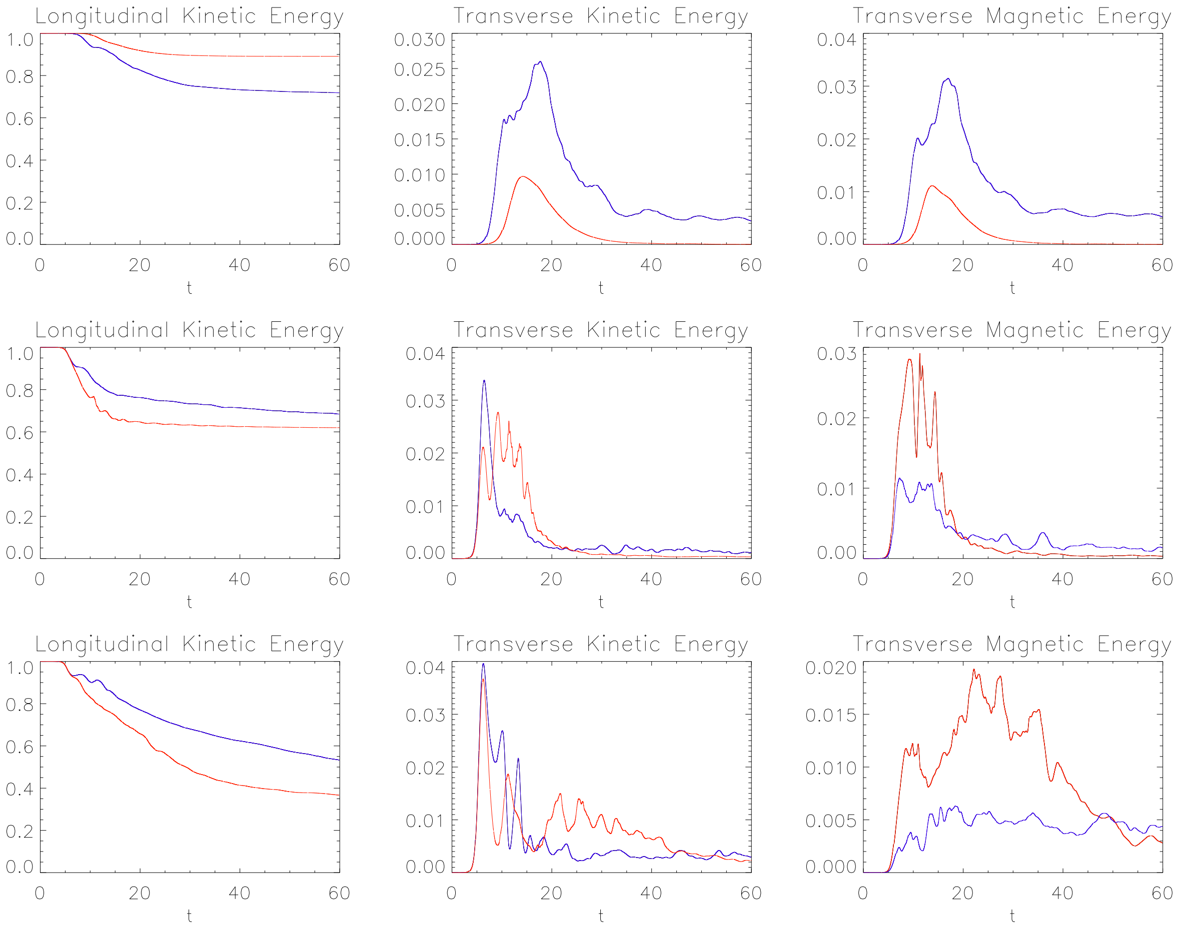

Figure 3.5. Energy evolution in the simulations of the individual mode of the KH instability. From left to right we present the longitudinal kinetic energy $E_{k,x}$, the transverse kinetic energy $e_{k,y}$ and the transverse magnetic energy $e_{m,y}$. The top row refers to the case $M_a = 2.5$, the middle row to the case $M_a = 7$ and the bottom row to the case $M_a = 20$. The blue line represents the reversed magnetic field simulations, while the red line the uniform case. Values are normalized over the initial longitudinal kinetic energy.

In Fig. 3.6 we report our results on the magnetic and kinetic saturation levels. We have found significant differences with the uniform case, which are listed below. First, it is clear that in our case the non-linear stabilization regime has completely disappeared. Indeed, a careful investigation of our simulations shows the formation of vortical motions in the range $2 < M_a < 4$. As a consequence, both the magnetic and kinetic saturation levels are greater than in the uniform case (see, in particular, the peak in Fig. 3.6, lower panel). This lack of nonlinear stabilization is expected from the linear phase, since the growth rates are higher than in the uniform case. Second, the opposit limit (quasi hydrodynamic regime) is reached in our case for $M_a \gtrsim 20$ instead of $M_a \gtrsim 30$ (see plateau in Fig. 3.6, upper panel). Third, in the intermediate regime the kinetic saturation levels are always greater than their counterparts in the uniform case, a result found also by Keppens et al. (1999). The magnetic saturation levels, on the other hand, are sensibly lower. This behaviour is possibly due to the growth of magnetic islands. Indeed, islands

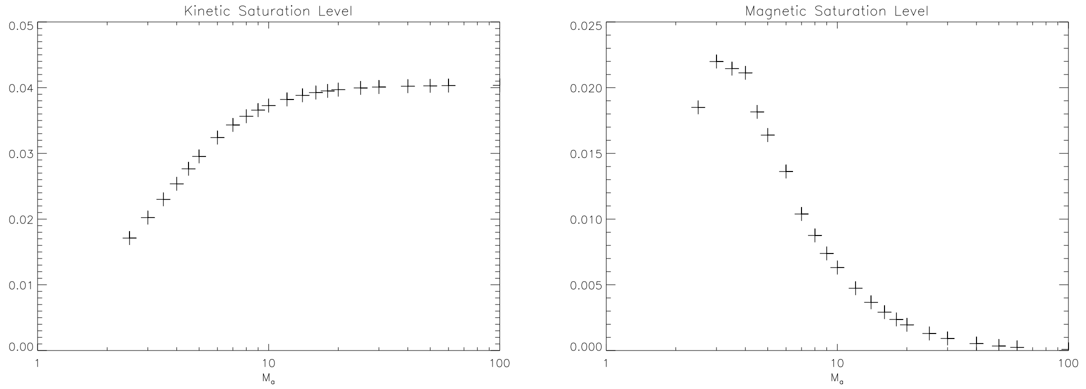

Figure 3.6. Saturation level as a function of the Alfvén Mach number M_a, for the transverse kinetic energy (*left panel*) and transverse magnetic energy (*right panel*) in the sheared magnetic field case. Values are normalized over the initial longitudinal kinetic energy.

appear just before the magnetic saturation and they are fed by the available magnetic energy to grow. As a consequence, there is less magnetic energy left to contribute to the amplification of the field around the KH vortex. The lower magnetic amplification factor is also confirmed by the value of the longitudinal magnetic energy (not shown), lower than in the uniform case at any given time.

Finally, the magnetic islands play also a role in the subsequent energy evolution. Three example cases are shown in Fig. 3.5. In the uniform case, the peaks in the transverse magnetic and kinetic energy indicate the formation of secondary vortices. These features are not present in the reversed case, partially because the islands contribute to a higher degree of turbulence therefore preventing the formation of ordered structures (see Fig. 3.5, second raw, panels two and three, and third raw, panels two and three).

3.3.6 Disruption and final state

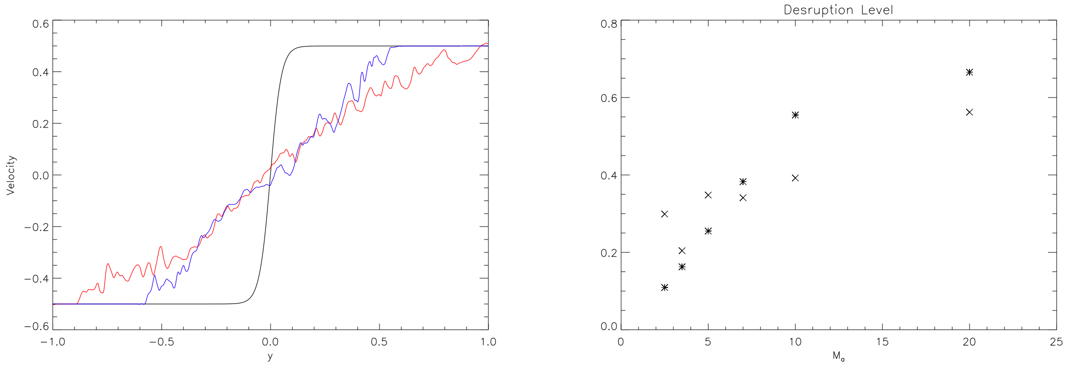

Figure 3.7. *Left panel*: transverse velocity profile along the y direction for the case $M_a = 10$, resolution 400x800. *Black line*: Initial profile. *Blue line*: Reversed field case at 60 time units. *Red line*: Uniform field case at 60 time units. The lines represent the average value along the x axis. *Right panel*: disruption level versus Alfvén Mach number for the uniform magnetic field case (stars) and the sheared magnetic field case (crosses).

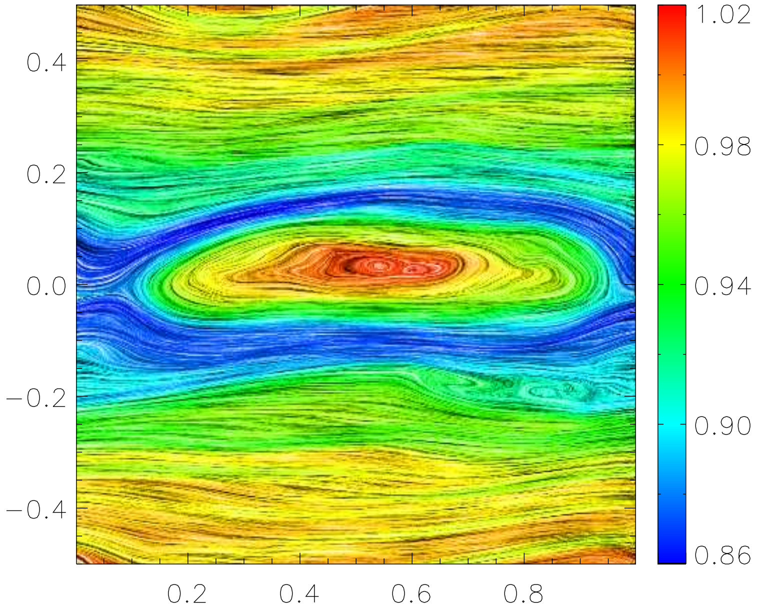

Figure 3.8. Final stage of the simulations with $M_a = 7$. The magnetic field structure, obtained with a line integral convolution method, is superimposed on the density plot. Only the part of domain with y in the range [−0.5,0.5] is shown.

To quantify the importance of the disruption of the flow, we consider the energy reduction of the longitudinal kinetic energy from its initial value. Consider that we stop the simulations at 60 time units because, after that point, diffusive effects start to become important, and the perturbation in few cases starts to affect the boundary layer.

Comparing the various simulations, we observe two different regimes. For relatively high magnetic fields, with $M_a < 5$, the instability in the reversed case is more disruptive. For example, when $M_a = 2.5$, 30% of the initial kinetic energy is released as opposed to only 10% for the uniform case (see Fig. 3.7, right panel, and Fig. 3.5, first raw, first panel). This can be explained recalling that in the range $M_a \lesssim 4$, the KH instability in the uniform case is non-linearly stabilized and the vortical motion cannot fully develop like in the reversed case. For low magnetic fields however, when $M_a > 5$, the final flow is less disrupted than in the uniform case, with a difference of order 10% (see Fig. 3.7, right panel, and Fig. 3.5, first panel of the second and third raws). To understand the behaviour in this low field regime we examine how the longitudinal velocity profile is changed at the end of the simulations. As an example we describe the case $M_a = 10$, plotted in Fig. 3.7 (left panel). The initial shear layer is enlarged by the instability in both uniform and reversed magnetic field, but in the uniform case the affected region is much wider. As a consequence the disruption effect on the flow is higher. Indeed, as shown by the characteristic widths in Fig. 3.7 (left panel), the shear thickness for the reversed field case is $\simeq 1.2$, while for the uniform case it is $\simeq 2$. The evolution towards the observed final configuration is determinant for the disruption level.

The final state in the uniform field case has been discussed in detail by Frank et al. (1996). We summarize here the main points. After the disruption of the vortex, a turbulent phase takes place. The system, then, relaxes to a laminar steady state. The velocity and magnetic fields are alligned, so the flow appears highly organized. As a consequence, the normalized cross-helicity,

$$\langle H \rangle = \frac{\int \hat{\mathbf{u}} \cdot \hat{\mathbf{B}} dx\, dy}{\int dx\, dy}, \tag{3.13}$$

almost reaches its possible extrema, ±1. Except for small variations following the magnetic field, the velocity structure is a simple shear layer with a thickness greater than the initial state. Moreover, magnetic and gas pressure are anti-correlated, and zones of magnetic pressure maxima define two flux tubes which characterize the final state.

In the reversed field case the scenario is very different. After the vortical motion is disrupted, a turbulent phase sets in (Fig. 3.4, panel four). The outcome, represented in Fig. 3.8, is a laminar steady state characterized by a magnetic island: a high density region in the centre of the domain, surrounded by low density plasma and delimited by closed magnetic field lines. Near the lateral boundaries of the island, the velocity and magnetic fields are not alligned. Although the velocity magnitude is small in this region, it is sufficient to produce vertical oscillations of the island. Far from the island, on the other hand, the fields are alligned and resamble the initial antiparallel configuration (see Fig. 3.7 for the velocity profile). Moreover, we observe small variations in the magnetic field, in the form of stripe like structures anti-correlated with gas pressure features, in agreement with the description by Frank et al. (1996). The formation of the magnetic island reduces the vertical extent of the zone interested by the disruption of the flow, especially for high Alfvén Mach numbers. As a consequence the disruption level is reduced. Finally, we note that the time needed to form the final island is longer for lower values of the magnetic field strength. Indeed, at the end of the simulation in the case $M_a = 20$, we observe islands on different spatial scales in the process of merging. This drastic difference in the final plasma configuration, as compared with the final state of the uniform field case, is a natural consequence of the initial antiparallel magnetic field profile.

As a final remark, note than we do not explore the quasi-hydrodynamic regime, corrisponding to $M_a \gtrsim 20$, because we have already observed that it is very similar to the uniform case in the initial phases, so we do not expect significant differences for the later evolution (see growth rates and saturation levels in Sec. 3.3.1 and Sec. 3.3.5).

3.4 Results for two dimensional extended layers

3.4.1 Global scenario

We present here the results of the simulations performed using an extended domain, which is roughly twelve times longer than the wavelength of the fastest growing mode of the instability.

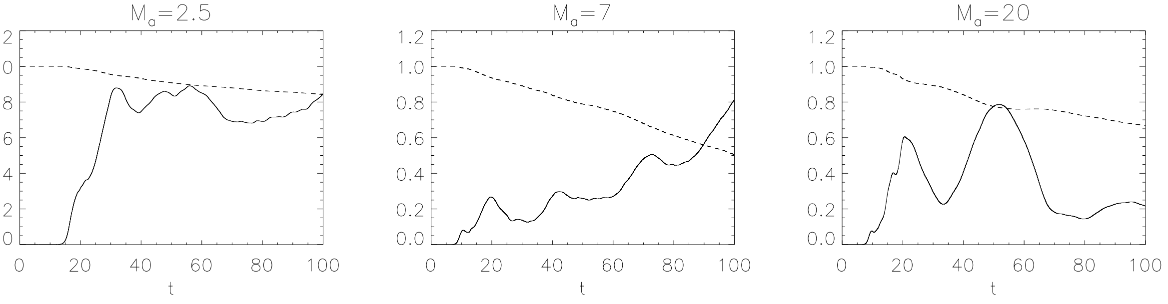

Figure 3.9. Temporal evolution of the longitudinal kinetic energy $E_{k,x}$ (*dashed line*) and of the transversal kinetic energy $e_{k,y}$ (*solid line*), for the following values of the Alfvén Mach number: $M_a = 2.5$ (*left panel*), $M_a = 7$ (*central panel*) and $M_a = 20$ (*right panel*). Values are normalized over the initial longitudinal kinetic energy. The values of the transverse kinetic energies are multiplied by a factor 100 in the case $M_a = 2.5$, and by 20 in both case $M_a = 7$ and $M_a = 20$.

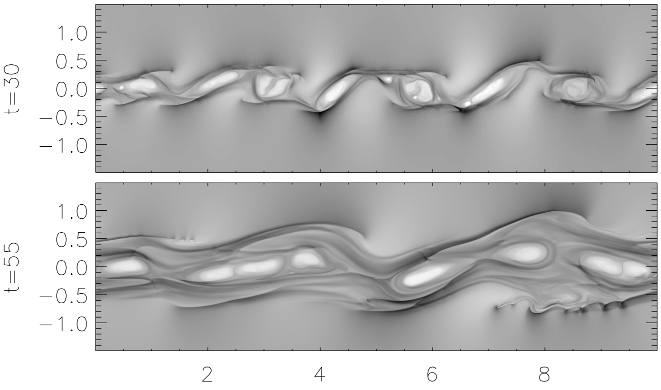

Figure 3.10. Density plot of the extended domain simulation in the case $M_a = 2.5$ at 55 time units. The gray scale represents values uniformly distributed in the interval [0.63,1.20]. Only the part of domain with y in the range [−1.5,1.5] is shown.

It has been proved in Baty et al. (2003) that the KH instability is characterized by a global trend to form large scale structures by merging smaller vortices. This coalescence mechanism greatly enhances the disruption effect on the flow and enlarges the shear layer thickness, and it is therefore of primary importance to understand the behavior of realistic sheared flows.

We have considered an extended domain (LD) in the reversed magnetic field configuration for three different Alfvén Mach numbers: 2.5, 7 and 20. The chosen resolution ensures more than 100 points per vortex, proved to be sufficient to observe the formation of the characteristic small magnetic islands described in Sec. 3.3.4.

Whatever the value of M_a, the global scenario in our simulations is the same as compared to the uniform case. Indeed, we observe an inverse cascade process with the formation of large scale structures. A series of successive pairing/merging events takes place, leading to the formation of a single big structure. However, in our non-uniform simulations the evolution is enriched by new physics due to the presence of magnetic islands. Indeed, the magnetic islands rapidly appear during the saturation of the initial KH vortices. During the KH merging, islands can be destroyed or interact with the adjacent structures, and new islands can form. The complex

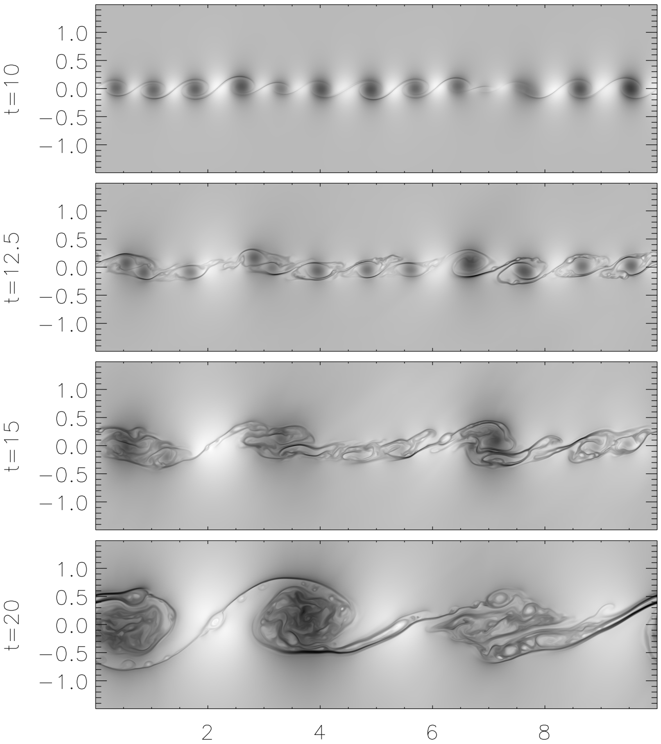

Figure 3.11. Density plots of the extended domain simulation in the case $M_a = 7$ for different times (from top to bottom: 10, 12.5, 15, 20). The gray scale represents values uniformly distributed in the interval [0.66, 1.13]. Only the part of domain with y in the range [−1.5, 1.5] is shown.

dynamics are also characterized by the observed coalescence of magnetic islands (Priest & Forbes 2000). For these reasons the islands are still present at the end of our simulations (see Fig. 3.10, last panel of Fig. 3.12 and second panel of Fig. 3.13).

In Fig. 3.9, we present the time evolution of the transverse and longitudinal kinetic energies, $e_{k,y}$ and $E_{k,x}$. The trend of the transverse kinetic energy is clearly different from the single vortex case and reflects the coalescence mechanism. In general in fact, as described in Baty et al. (2003), after the initial exponential growth the transverse kinetic energy increases roughly linearly with a superimposed oscillation, and the local maxima correspond to merging events.

Regarding the disruption levels (see the longitudinal kinetic energy evolution in Fig. 3.9), a direct comparison with the simulations done by Baty et al. (2003) is very difficult, because of differences in the normalization and domain size, and because of the random initial perturbation employed. Nevertheless, we observe that the coalescence process acts in a similar way and that the desruption level is of the same order. The difference is mainly due to the magnetic islands, which provide additional dissipation and greatly enhance the turbulent nature of the final state of the simulations.

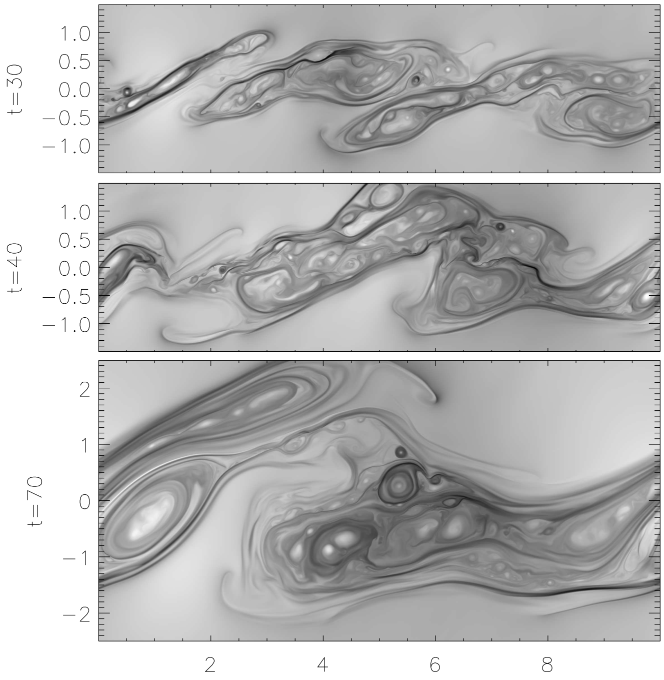

Figure 3.12. Density plots of the extended domain simulation in the case $M_a = 7$ for different times (from top to bottom: 30, 40, 70). The gray scale represents values uniformly distributed in the interval [0.66, 1.13]. Only the part of domain with y in the range [−1.5, 1.5] is shown, except for the last image represented in the domain [−2.5, 2.5].

3.4.2 Details on different regimes

In the case $M_a = 2.5$, for strong magnetic fields, our simulations appear quite different from the uniform case. From the upper panel of Fig. 3.9, we follow the trend of the transverse kinetic energy: after a short exponential increase, the curve reaches the first local maximum at around $t = 20$. Instead of decreasing, it continues to grow up to a level that is more or less maintained for the rest of the simulation except for some oscillations of small amplitude. After the initial saturation, the KH vortices start to merge, but further pairing is slowed by the relatively strong magnetic field. At the same time, the vortices evolve rapidly to become magnetic islands, as discussed in Sec. 3.3.6. In the first panel of Fig. 3.10, we can see how the vortices continue to interact with each other, although they have almost completely formed magnetic islands in their centres. In addition, the interaction seems to follow a definite pattern of alterning round and elongated structures. The outcome is a long structure with limited vertical extension, formed by magnetic islands slowly merging together (see Fig. 3.10). A complete description of such a system would require further study, but is beyond the scope of the present paper.

In contrast, the energy evolution of the case $M_a = 7$ is quite similar to the uniform case. In the lower left panel of Fig. 3.9 one can clearly see the transverse kinetic energy steadily increasing in time, and the presence of episodic peaks. A simultaneous investigation of the energy evolution diagrams and the plots of Fig. 3.11 and Fig. 3.12 confirms that the peaks in energy are indeed related with merging events. The first image represents the saturation of the initial 12 vortices.

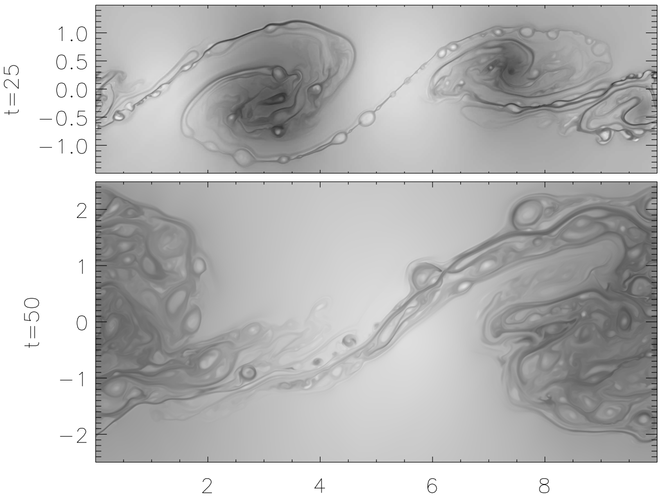

Figure 3.13. Density plots of the extended domain simulation in the case $M_a = 20$ for different times (*upper panel*: $t = 25$, *lower panel*: $t = 50$). The gray scale represents values uniformly distributed in the interval [0.5,1.2]. Only part of the domain is shown: y in the range [−1.5,1.5] (*upper panel*) and y in the range [−2.5,2.5] (*lower panel*).

The second snapshot, taken at $t = 12.5$ in a local minimum of the transverse kinetic energy, is the beginning of several multiple merging events. The most evident ones are at the positions $x = 0.5$, 3, and 7. Note the development of magnetic islands driven by the KH instability, previously visible in the single mode simulations (see Fig. 3.4, panels 2 and 3). The snapshot taken at $t = 15$ shows the intermediate step towards another local maximum of the kinetic energy. The pairing events mentioned above have taken place, but are immediately followed by the capture of another nearby vortex. For example, the density structures at $x = 1$ and 3 are formed by three merging vortices each. The peak in energy at $t = 20$ marks the conclusion of the complicated interaction with the formation of three distinct vortices. The first one on the left and the middle one have been formed by three vortices, while the last one on the right by four. This explains why it appears more turbulent than the other two vortices. Between the middle and the right vortex there is a structure formed by the merging and deformation of two vortices. From this point the evolution appears to be more complicated. The three vortices tend to be disrupted and form a bigger coherent structure. Further evolution leads to the turbulent structure shown in the last snapshot of Fig. 3.12. Its vertical size extends on a large fraction of the total computation domain and increases at later stages. As a consequence it is not a surprise that the final disruption level is much greater than in the single mode case.

The turbulent aspect of our simulations is even more evident in the case $M_a = 20$. As we can see in the two snapshots of Fig. 3.13, this case is characterized by a big number of small magnetic islands and by turbulent structures. The transverse kinetic energy evolution, shown in Fig. 3.9, lower right panel, presents only two well defined peaks at $t = 20$ and $t = 50$. This is the case because the vortex merging process is not happening simultaneously for the different vortices, and as soon as a pairing event occurs, another one sets in. This trend promotes multiple merging events, in which three or four vortices interact simultaneously to form a single structure, and, together with the rich magnetic structure, can explain the augmented turbulence.

3.5 Results for three dimensional layers

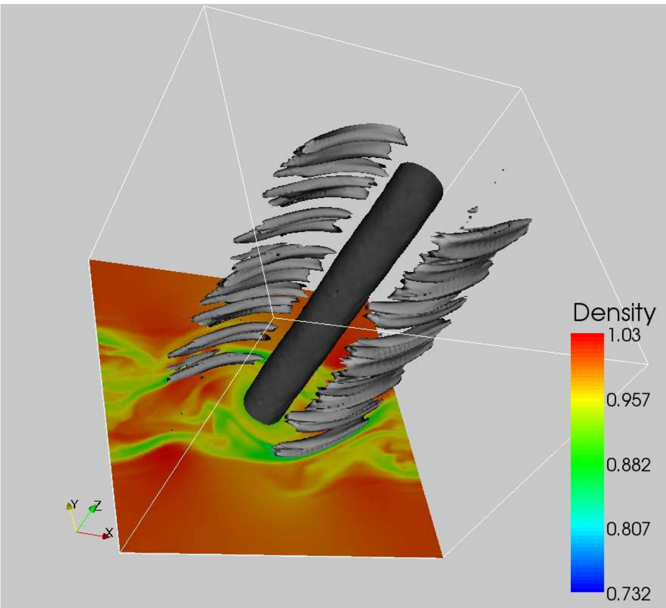

Figure 3.14. *Dark grey surface*: Isosurface of the density at $\rho = 0.92$. *Light grey surfaces*: Isosurface of the magnetic field magnitude at $B = 0.45$. The values are chosen to highlight structures. A cut of the density, parallel to the x-y plane, is also shown.

In this section, we present the results regarding the 3D simulations. The aim is to verify and extend our 2D results in a more realistic plasma configuration. The 3D domain employed is a tri-dimensional version of the SD case. The simulations have been performed for three different magnetic field strengths: $M_a = 2.5$, $M_a = 7$ and $M_a = 20$.

Up to the saturation time, the 3D simulations appear very similar to their SD counterparts. Indeed, a 3D Kelvin's Cat's Eye vortex is formed, with the axis along the z direction. We do not observe the formation of new appreciable tri-dimensional features, and the instability retains essentially a 2D nature. Moreover, both the growth rates and the saturation levels are the same as in the corresponding SD cases. The magnetic islands described in Sec. 3.3.4 are also observed in the 3D runs. They are formed and disappear on the same time scales as in the 2D simulations, and they follow the same evolution described previously.

After the magnetic saturation, however, tri-dimensional effects starts to become evident. We observe, in particular, two different processes, already present in Hydrodynamics. First, filamentary structures can be observed in the magnetic field representation of Fig. 3.14. Such structures are very similar to the ones present in Ryu et al. (2000), and can be interpreted as "rib vortices" (Hussain 1986). Probably, however, they are forced to be parallelto the (x, y)

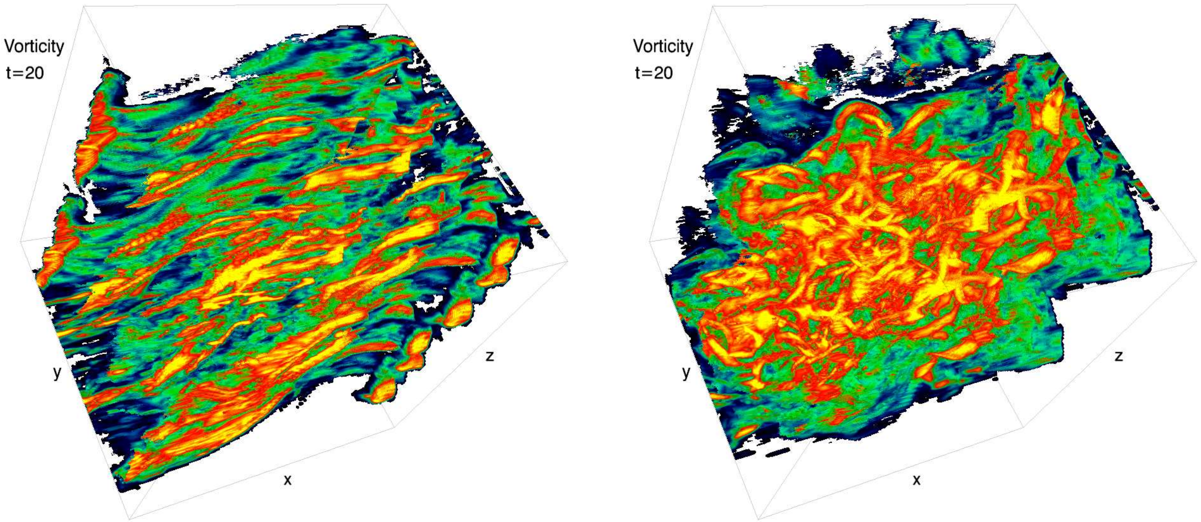

Figure 3.15. Volume rendering of the vorticity magnitude, at 20 time units. *Left Panel*: $M_a = 7$. *Right Panel*: $M_a = 20$. The color scale is set arbitrarily to highlight structures. From lower to higher values: blue, green, red, yellow.

plane because only one vortex is formed in our domain. Moreover, the periodic boundary conditions along z force the KH roll to have the axis along the z direction, thus influencing the "rib" structures. "Rib vortices" are coherent vortex tubes which connect the KH vortex with saddle points in the flow. The consequent vortex stretching plays a major role in the non-axial distortion, and consequently disruption, of the KH vortical structure. Second, the elliptical instability affects the plasma in its rotation, since the KH vortex is not circular, but slightly elliptical (see Kerswell 2002, and references therein). For these reasons, the KH vortex is rapidly disrupted.

The subsequent plasma configuration is very different from the final state we describe in Sec. 3.3.6. First of all, no magnetic island is formed. The explanation lyes in the 3D nature of the KH vortex disruption, which does not allow the formation of coherent structures featuring closed field lines. Moreover, we observe a different final state, depending on the value of the Alfvén Mach number. For $M_a = 2.5$ and 7, the system reorganize itself to a new, enlarged shear layer. The vorticity magnitude, $|\nabla \times \mathbf{v}|$, plotted in the upper panel of Fig. 3.15, shows how the vorticity structures are distributed mainly in the x-y plane, and alligned along the x direction. The magnetic field (not shown) follows a similar pattern. Note, however, that along the shear plane, the magnetic topology is not strictly antiparallel any more. Reconnection events, triggered by the evolution and disruption of the KH vortex, reorganize the field lines into bended and tangled structures (see Fig. 3.16). Conversely, in the case $M_a = 20$, we observe a turbulent state, clearly visible in the chaotic structure of the vorticity (Fig. 3.15, lower panel). The extension in the y direction of the turbulent region, limited roughly to $-0.4 \lesssim y \lesssim 0.4$, increases to a bigger part of the domain in later stages of the simulation. In this region, the

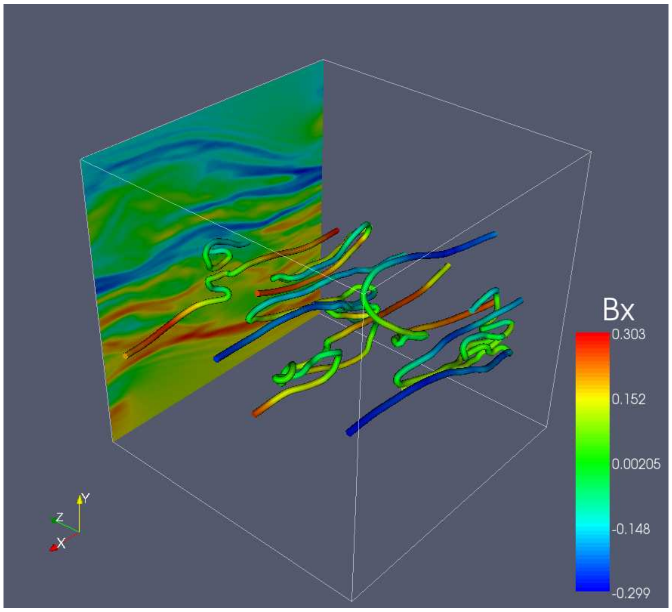

Figure 3.16. Magnetic field lines on the shear plane in the 3D case $M_a = 7$, at 20 time units. A cut of B_x, parallel to the x-y plane, is also shown. For both the lines and the cut, the colour code represents the value of B_x.

magnetic fields are even more tangled than on the shear plane of the previous case $M_a = 7$.

These results correspond well with the ones found in Ryu et al. (2000) for a uniform magnetic field. Indeed, the former authors have investigated the KH instability in 3D with a uniform magnetic field, and they have observed two different regimes in the simulations, characterized by a different final state: a laminar, ordered configuration for high magnetic field strengths, and a turbulent state for low magnetic fields. They have described how the magnetic fields are amplified to higher values than in the analogous 2D cases, by twisting around rib vortices. As a consequence, if the amplification can reduce the Alfvén Mach number to less than unity before the KH vortex is disrupted, the flow is self-organized to a laminar, enlarged shear layer. This mechanism is working in our non-uniform simulations as well, with one important difference: while in the uniform case the turbulent regime is observed for $M_a > 50$, in the anti-parallel case the threshold is shifted to $M_a \simeq 20$. The difference is due to the growth of magnetic islands before the saturation of the KH instability. In Sec. 3.3.5, we discussed how the islands lower the magnetic saturation energy and, in general, slightly oppose to the magnetic amplification. Therefore, the self-organization process takes place only in a range of initial magnetic fields stronger than in the uniform case.

Chapter 4

Numerical simulations of jets

In this chapter we present the results of our simulations of astrophysical jets. We are aware of the fact that the model employed is rather simplified. However, it is important to focus first on the stability properties of jets, to understand the physical mechanisms. Such understanding can then be used as a base to start developing a more sophisticated model. Indeed, when the behavior of a plasma is determined by several simultaneous agents, it is very hard or impossible to have a clear view of the problem. Therefore, we postpone the discussion of more complex models to the final chapter of the thesis.

4.1 Setup

We have chosen a cartesian coordinate system, and we have prescribed a flow in the x direction. In all the simulations shown in this chapter, a "smoothed top hat" profile for the velocity has been employed. For the two-dimensional (2D) simulations:

$$V_x = \frac{V_0}{2}\left[1 - tanh\left(\frac{R_j}{2a}\cdot\left(\frac{y}{R_j} - \frac{R_j}{y}\right)\right)\right], \tag{4.1}$$

where V_0 is the velocity of the beam, measured in units of the sound speed in the jet, R_j is the jet radius, and a is the thickness of the shear layer. We chose the jet diameter as unit length, so $R_j = 0.5$. For the three-dimensional (3D) simulations, the velocity profile is the same as in the previous expression 4.1, but substituting y with r defined as $r = \sqrt{y^2 + z^2}$. The magnetic field is antiparallel, and sheared with the same thickness as the velocity profile, effectively creating a current sheet. This current sheet is located in the same position as the velocity shear (vortex sheet). The analytic expression for 2D simulations is the following:

$$B_x = B_0 tanh\left(\frac{R_j}{2a}\cdot\left(\frac{y}{R_j} - \frac{R_j}{y}\right)\right). \tag{4.2}$$

For 3D simulations, the previous substitution $y \rightarrow r$ is used. V_y, V_z, B_y and B_z are all set to zero initially. The initial density ρ_0 is set to unity. The pressure is computed from the magnetic

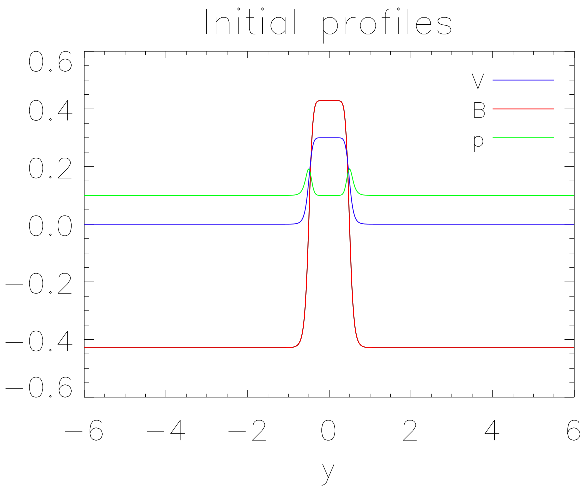

Figure 4.1. Initial profiles for the physical quantities in the jet simulations. *Blue*: Velocity profile. The velocity has been multiplied by 0.1 to fit in the plot. *Red*: Magnetic field profile. *Green*: Pressure profile. A factor 0.5 has been subtracted from the pressure to fit it into the plot.

field profile, in order to have total pressure equilibrium, starting from the value of pressure on the jet axis, set to $1/\gamma$. In this way the sound speed c_s on the jet axis $\sqrt{\gamma p_0/\rho_0}$ is equal to 1. Finally, the time unit used in the simulation is the sonic crossing time $t_0 = 2R_j/c_s$.

The quantities V_0, B_0 and a are the parameters of the model. In practice, since the speed of sound is equal to one, V_0 corresponds to the sonic Mach number of the jet. Regarding the magnetic field, it is useful to introduce the initial Alfvén speed $v_a = B_0\sqrt{\rho_0}$. Since we set the initial density to unity, in our normalization the Alfvén speed corresponds to the initial magnitude of the magnetic field. The properties of the instabilities are often determined by the Alfvénic Mach number $M_a = V_0/v_a$, which will be used as a measure of the magnetic field in what follows. In fig. 4.1, the profiles for the physical quantities are plotted for the case $M = 3$, $M_a = 7$ and $a = 0.2$.

These profiles describe a slab magnetized flow in 2D or a cylindrical magnetized flow in 3D, and they are applied in the whole domain as initial condition. As a consequence, the model prescribes the existence, at the beginning of the simulations, of a beam in equilibrium filling the domain in the x direction. This condition is common for the study of instabilities. The advantage is that the initial condition of the beam is known, and therefore the stability properties can be easily related to the beam parameters. On the other hand, the disadvantage is that no bow shock is formed. To observe such structure, a beam must be injected from a boundary in a plasma at rest (or with the appropriate model for interstellar/intergalactic medium). The study of such structures, however, is beyond the scope of this thesis.

The details of each simulation are left for the related sections. Here we want to describe the difference between a temporal and spatial approach in terms of the domain choice and boundary conditions. The temporal approach allows to follow the time evolution of the instability of a section of the jet. To do so, two assumptions are made. First, the jet must be infinitely long. Second, the initial perturbation that excites the instability is applied at the same time along the whole jet length. Numerically, this is achieved by periodic boundary conditions in the direction of the flow. In our case, whatever amount of matter is outflowing from one side of the domain in the x direction, it is reinjected on the other side, and vice-versa for inflowing matter. This approach has some advantages, the main one being the high resolution achievable, since a big domain is usually not needed. In addition, the periodic boundary conditions are numerically extremely simple to implement, and are always correct. The downside is a complete lack of convective effects (see below), and a small domain size, which limits the maximum wavelength of any possible perturbation inside the domain.

The spatial approach requires the existence of a jet over a long domain. The flow is injected from a boundary of the domain, and it is allowed to flow outwards on the opposite side. It is not numerically trivial to implement the inflow boundary condition, especially in the presence of magnetic fields, because the $\nabla \cdot \mathbf{B} = 0$ condition is not automatically satisfied. In addition, the outflow boundary condition usually implemented in numerical codes, which imposes a null gradient in the considered direction for all the physical quantities, is not always correct. In particular, some waves can be partially reflected by the boundary instead of propagating outwards. Once these difficulties are overcome, however, the spatial approach proves to be better than the temporal approach for jet simulations, because it takes into account the convective nature of the Kelvin Helmholtz instability, which does not grow at a fixed point in space, but is convected along the fluid resulting in a spatially growing pattern. The simulations using a spatial approach are computationally much more expensive than the temporal ones. There are two reasons. One, the domain size must be much bigger, to allow the instabilities to grow and develop *before* they are advected out of the domain. Two, the simulated period of time is longer, in order to appreciate the growth of instabilities and possible non-linear interactions.

4.2 2D Jet simulations

Before describing the results of the 2D simulations it is useful to remind the reader that the slab geometry employed is one of the two main possibilities when simulating jets in two dimensions. In our configuration, the problem is strictly 2D, so all the vectors have only two components. The second possibility, called 2.5D, considers a jet in cylindrical symmetry. The domain, in cylindrical coordinates, extends from the jet axis to a certain distance from the jet boundary. This approach allows to include three components for the vectors, thus easily implementing helical fields and/or jet rotation. The downside is that, due to axisymmetry, only the pinch modes are possible, equivalent in 3D to the modes with azimuthal mode number n equal to zero (see sec.2.2.4). A slab geometry allows for varicose (equivalent in 3D to the modes with $n = 0$) and sinuous modes (equivalent in 3D to the modes with $n = 1$). For instability analysis, the slab geometry is preferred, since it allows a richer physics.

4.2.1 Temporal approach

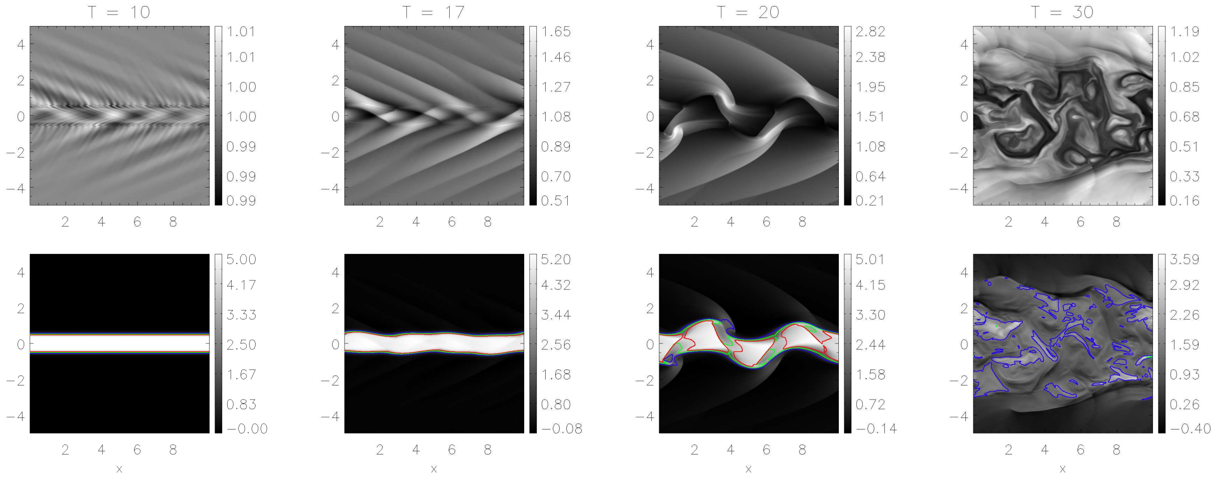

Figure 4.2. Gray scale images of the density (*Top Panels*) and of the velocity parallel to the jet axis (*Bottom Panels*). The color contours represent the local Mach number. *Red*: $M = 3$, it green: $M = 2$, *blue*: $M = 1$. The images are taken form the temporal simulation with $M_a = 10$, at different times. From left to right, at 10, 17, 20 and 30 time units.

The simulations using the temporal approach were performed on a cartesian domain defined by $0 \leq x \leq L_x$ and $-L_y \leq y \leq L_y$, with $L_x = 10$ and $L_y = 5$. The lengths are in unit of jet diameters. The grid is uniform, with resolution 512x512 grid cells. The parameters used in this simulations are $M = 5$ and $a = 0.2$. A variety of magnetic field strengths were employed: $M_a = 3.22$, 4.56, 7, 10 and 25. The velocity shear layers were perturbed initially with a random small perturbation in the velocity perpendicular to the jet flow. These simulations were performed in preparation for the much more expensive spatial simulations described in the next sections.

In the range of magnetic fields considered, the main evolution of the KH instability in these simulations is basically the same. We can recognize four different evolutionary phases (Bodo et al. 1994):

1. **Linear phase**

   The perturbations applied to the system evolve following the linear theory. The most unstable mode then prevails over the others. This phase ends when the perturbations grow enough to produce internal shock waves. During this phase, the energy exchange between the jet and the external medium is low.

2. **Expansion phase**

The perturbations, evolved into shock waves, deform the beam. Energy is transferred to the external medium by sonic waves. The strength of internal and external waves increases in time. The jet undergoes an expansion in the post-shock regions.

3. **Mixing phase**
   The motion becomes highly turbulent, and the the material from the jet and the external medium is mixed. As a consequence, the jet transfers a significant fraction of its kinetic energy to the external medium.

4. **Quasi-stationary phase**
   The velocity of the beam is drastically reduced from the initial conditions, and a quasi-stationary flow much larger than the initial jet is established. This final state depends heavily on the density ratio between the ambient medium and the jet. Heavy jets maintain some structure, while lighter jets appear completely diffused and mixed with the ambient medium.

As an example, in fig. 4.2 we show density and velocity for the first three phases of the simulation with $M_a = 10$. The first panels on the left show the evolution of the initial perturbations in the linear phase. Note in the density plot, outside of the beam, the presence of two superposed wave structures. The first one, with long wavelength, presents a high inclination with respect to the y axis, and is typical of body modes. Inside the beam it produces a series of high and low density regions. The second one presents a very short wavelength and small inclination with respect to the y axis, and is proper of surface modes. In Hydrodynamic simulations, the particular combination of Mach number and density ratio between the jet and the external medium determines whether body modes or surface modes dominate the subsequent behavior (Bodo et al. 1994). Rather slow ($M < 4$) and heavy jets are dominated by surface modes, while fast jets ($M > 4$) are always dominated by body modes.

The second panel of fig. 4.2 shows the beginning of the expansion phase. The body modes have grown to the point that strong shocks are driven both outside and inside the beam, where they assume the characteristic biconical shape. In the third panel, we can see an advanced stage of the expansion stage. The jet is clearly deformed by a sinuous mode, with strong shocks dominating the inner structure of the jet. The last panel shows the mixing phase. The density presents a chaotic structure and what remains of the initial flow has now a very low velocity, with local Mach number $M \sim 0.5$.

The effects of different strengths of initial magnetic fields are evident in the time scale of the whole disruption process, which is longer for stronger magnetic fields, and in the width of the quasi-stationary flow at the end of the simulations, which is narrower for stronger magnetic fields. For example, in the case $M_a = 10$, the quasi-stationary phase is reached at $t \sim 35$, with a residual flow width of about 8 jet diameters. The case $M_a = 3.22$ reaches the quasi-steady phase at $t = 40 - 45$ and the flow width is ~ 4 jet diameters.

4.2.2 Spatial approach

The simulations using the spatial approach were performed on a cartesian domain defined by $0 \leq x \leq L_x$ and $-L_y \leq y \leq L_y$, with $L_x = 80$ and $L_y = 10$. Remember that the lengths are in units of jet diameters. The grid is uniform, with resolution 4096x1024 grid cells. To avoid reflection from the outflow boundaries, in the y direction and in the rightmost boundary of the x direction, an additional "boundary domain" was employed, consisting in a non-uniform grid. In this zone, the grid cell size increases with the distance from the boundary. In this way it is possible to cover long distances with few grid cells. The advantage is twofold. On one hand, any wave must travel a long way before reaching the outer boundary of the "boundary domain", and a long way back if it is partially reflected. On the other hand, non uniform grids are more diffusive than uniform ones, so the waves are effectively damped: if they are indeed reflected, their influence on the central part of the domain, where the jet flows, is minimal.

The inlet of the jet was perturbed with a small-amplitude random noise applied to the velocity component perpendicular to the initial flow. This perturbation was turned on for the whole simulation, which was run for 150 time units. The parameters used in this simulations are $M = 3$, $M_a = 7$ and $a = 0.2$. We performed a simulation with the antiparallel magnetic field, and one with a uniform field for reference. The two simulations presented basically the same behavior and they resemble one with each other strikingly. This basically tells us that the impact of an antiparallel magnetic field on a jet is not as strong as observed for single shear layers (see chapter 3). Despite this fact, we found very interesting results with our simulations, which we describe below.

Overview of the simulation

To describe the various stages of the simulation we employ first a series of snapshots of the density at various times, as shown in fig. 4.3 and fig. 4.4 The first image, taken at 10 time units, shows a series of low and high density regions, formed by the evolution of the oblique shocks visible in the jet just at the leftmost part of the domain. These structures are typical body modes of the varicose type. A temporal simulations with the same parameters and resolution was dominated in the initial stages by a sinuous mode instead (see fig. 4.5). The spacing between two successive high and low density regions corresponds to the wavelength of the instability. We can observe that this quantity is roughly four times the jet diameter. This result is somewhat surprising since the most unstable mode for jets should have a wavelength of the order of $2\pi R_j M$, so roughly 9 in our simulation (Ferrari 1998). The difference could be due to the fact that such expression is valid for top hat velocity profiles with null thickness. The perturbation is advected by the flow from left to right at approximately half of the speed of the jet. Note however, that ahead of the zone with strong density perturbations, there is a series of weaker structures. These structures are probably secondary instabilities, advected roughly at the velocity of the flow, in analogy to the discussion on the "convective generation" of instabilities for transonic flows in Viallet & Baty (2007) and references therein.

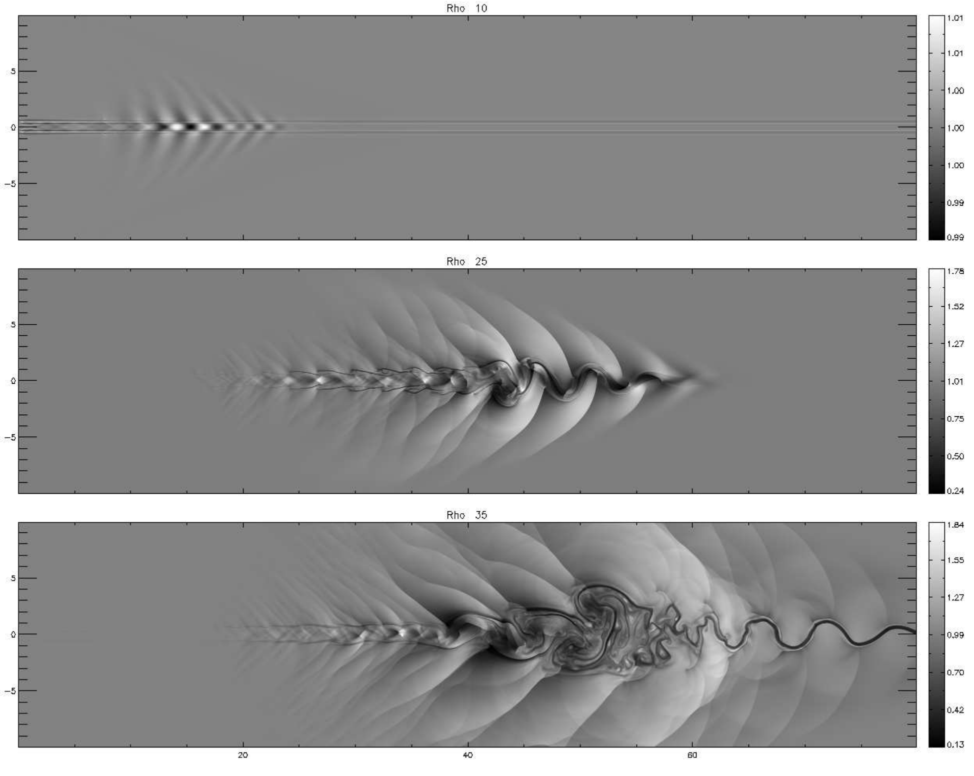

Figure 4.3. Grey scale density plots of the spatial simulation with antiparallel magnetic fields, at different times. From top to bottom: 10, 25, and 35 time units. Light tones correspond to higher densities.

The second snapshot of fig. 4.3 is taken at 25 time units. We can see that the perturbation has grown considerably and move to the centre of the domain. Note that no perturbation is visible at the inlet, because of the different color scale used. Indeed, they are just too small compared to the perturbation in the centre. Note how the behavior of the instability is different between the zone $x \lesssim 40$ and $x \gtrsim 40$. In the former the mode of the instability is basically varicose, while in the latter it is sinuous. The sinuous part reaches $x \sim 60$, indicating that this mode was advected at the flow speed as described before. This picture also shows that the instability affects heavily the external medium, with the formation of strong shock waves compressing the plasma. At the position $x \sim 42$, the onset of a major disruption of the flow can be observed.

The third picture, corresponding to $t = 35$ time units, shows the effects of the jet disruption. The beam is decelerated heavily and expands on the sides in a turbulent way. Because the deceleration, the jet in the zone $x \gtrsim 60$ is not supplied by new plasma from the inlet and

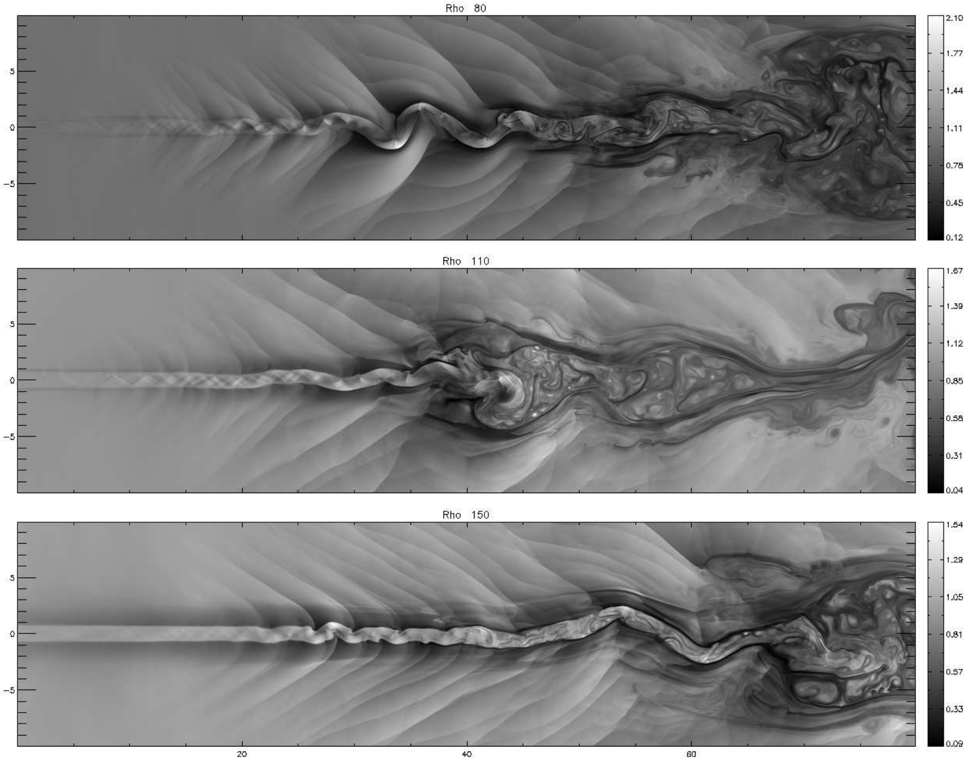

Figure 4.4. Grey scale density plots of the spatial simulation with antiparallel magnetic fields, at different times. From top to bottom: 80, 110 and 150 time units. Light tones correspond to higher densities.

appears as a low density stripe. Its sinusoidal pattern is the effect of the convective secondary instabilities. Note, in the zone $20 \lesssim x \lesssim 40$, the presence of several weak waves close to each other, both inside and outside the beam, as a consequence of the excitation of small wavelength modes of the instability.

The jet undergoes episodic disruption and revival. Indeed, the plasma upstream of the disruption area, is faster and can propagate through it. However, new instabilities arise, which can destroy the flow again. In the first snapshot of fig. 4.4 , we observe the presence of a strong sinuous mode at $x \sim 35$. This mode presents a wavelength longer than the ones observed previously. It is indeed characteristic of the KH instability to show an inverse cascade process towards longer wavelengths, realized by merging of modes with smaller wavelengths. This process was evident for the transonic single shear layers described in the previous chapter, and is reported to be present also in slab configurations (Baty & Keppens 2006).

In snapshot 2, we can observe again the effects of a big jet disruption. Note also the presence of a low density region around the jet in the zone $20 \lesssim x \lesssim 40$. This "envelope" region is characterized by a slow flow parallel to the jet velocity and by a low plasma beta. We will discuss this region in more details in what follows. In the last snapshot, we can see the end of the simulation. The density of the jet presents a coherent structure up to $x \sim 65$, which is

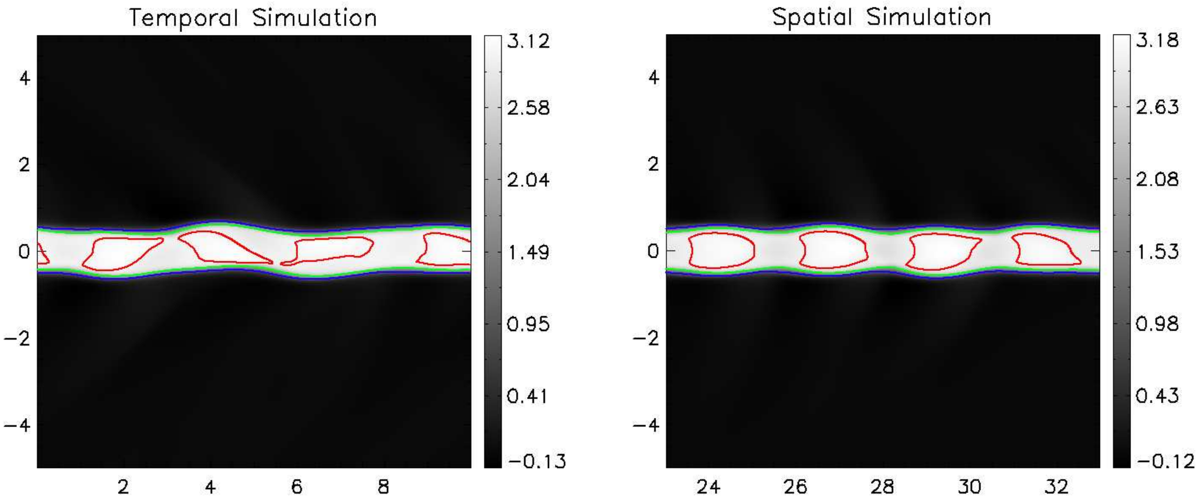

Figure 4.5. Gray scale images of the velocity parallel to the jet axis. The color contours represent the local Mach number. *Red*: $M = 3$, it green: $M = 2$, *blue*: $M = 1$. *Left panel*: Temporal simulation. *Right panel*: Spatial simulation. Note the different mode of the instability.

roughly two times the distance that the jet could cover before the first disruption. Note that the envelope is now more visible and extended further upstream.

The coherence of the beam is confirmed also by the contours of the Mach number in the upper panel of fig. 4.6 . Indeed, the jet can maintain a Mach number greater than 2 basically across the whole domain. This enhanced collimation is the outcome of a magnetic field amplification that takes place around the jet. The details are given below.

Magnetic field enhancement

In the paper by Viallet & Baty (2007), the stability of transonic jets is studied, using both spatial and temporal approach. The spatial approach showed very interesting results. Indeed, the authors of the latter paper identified a trail structure propagating upstream, related to an enhancement of the magnetic field strength, which tends to lower the local Alfvén Mach number to a value of order 2 for a wide range of initial magnetic field strengths. Such mechanism is caused, in transonic flows, by the build up of vortices of the KH instability . In the previous chapter we discussed how the magnetic field is expelled from the vortex centre and stretched and amplified around the vortex perimeter. In such a way, the magnetic perturbations, formed at the jet boundaries, are able to travel along the field lines in the form of Alfvén waves. This explains why the field amplification can travel upstream, forming an envelope around the jet. The previous authors performed also a simulation for the supersonic case, but did not observe magnetic field enhancements, because in supersonic regimes the KH instability does not produce vortices.

We argue, however, that a very similar scenario is still possible for supersonic jets. Indeed, we

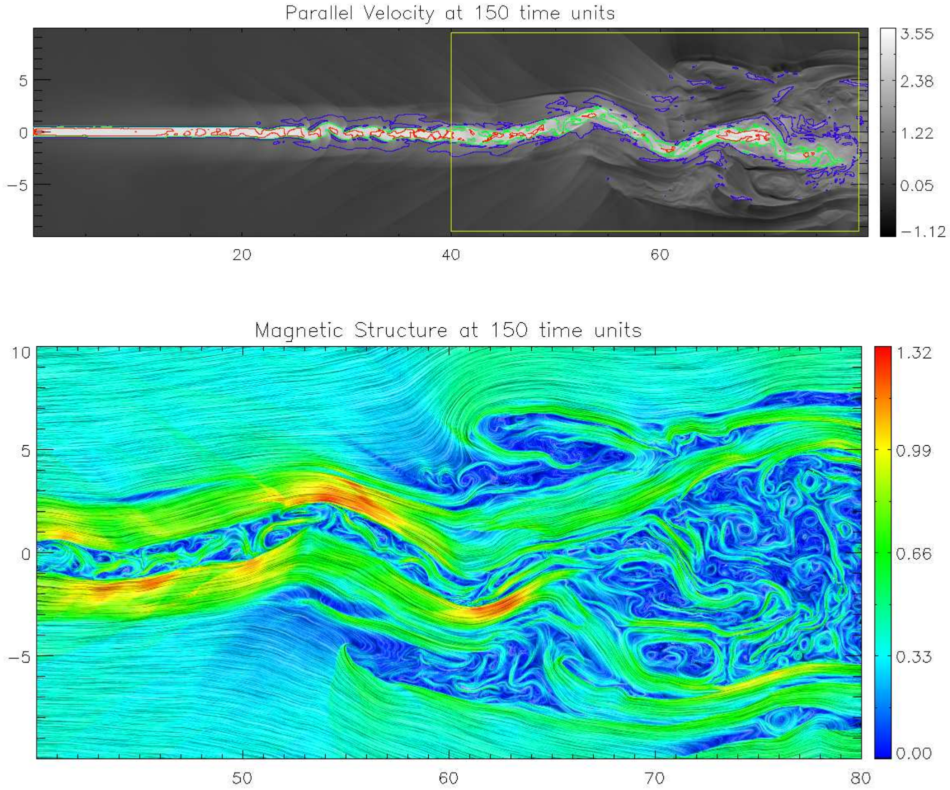

Figure 4.6. *Upper panel*: Gray scale images of the velocity parallel to the jet axis at the end of the simulation. The color contours represent the local Mach number. *Red*: $M = 3$, it green: $M = 2$, *blue*: $M = 1$. The region highlighted in yellow is magnified in the lower panel. *Lower panel*: Line integral convolution image of the magnetic fields. The colors indicate the strength of the magnetic field, while the brightness modulation shows the field lines.

observe a magnetic field amplification which propagates upstream. The amplification factor, at the end of the simulation is roughly 2, smaller than in Viallet & Baty (2007), but anyway enough to lower the local Alfvén Mach number to values of order $2 - 3$. A cut along the y direction at the position $x = 20$ is plotted in fig. 4.7 for the beginning and the end of the simulation, showing the magnetic amplification. The physical origin of the magnetic perturbations, responsible for the onset of the strengthening mechanism, is found in the sinuous mode of the instability. The particularly violent lateral displacements of the beam cause the magnetic field just outside the jet to be compressed and therfore enhanced. This process is clearly illustrated in the lower panel of fig. 4.6 The red colored regions, corresponding to a high magnetic field intensity, are located where the jet is strongly bended. From the vector field direction, we can see that the external magnetic field is deformed and bended to follow the shape of the jet. The magnetic field inside the beam, however, is chaotic. This situation is not completely surprising, because there is a difference of field strength across the boundary of the jet, and the stability properties of the

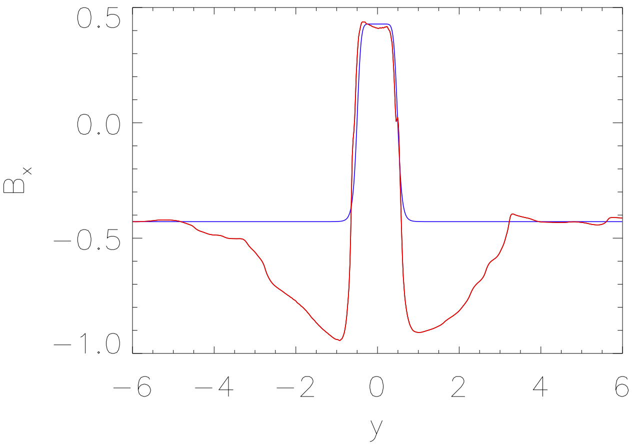

Figure 4.7. Vertical cut of the magnetic field along the y direction at the position $x = 20$. *Blue*: Initial configuration. *Red*: end of the simulation.

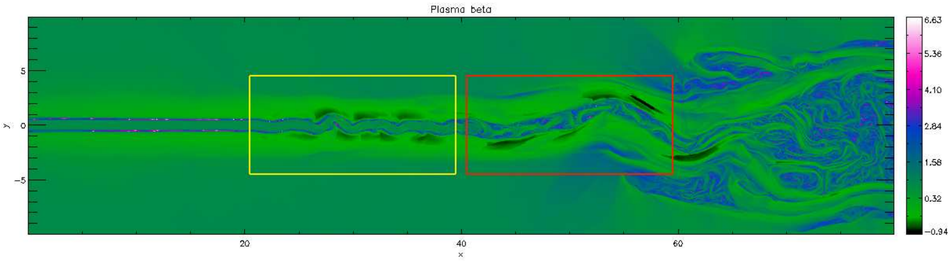

Figure 4.8. Plasma Beta of the antiparallel magnetic field simulation. The color scale is logarithmic. The yellow and red boxes are magnified in fig. 4.2.2.

regions inside and outside are different (see Jeong et al., 2000 for an example of non symmetric setup). Moreover, the last panel of fig. 4.4 shows that a transition from mainly laminar to mainly turbulent is achieved at the position $x \sim 40$. The same position marks the transition from a jet with Mach number $M \sim 3$ to a jet with $M \gtrsim 2$ (see upper panel of fig. 4.6).

At the end of the simulation, an envelope of high magnetic fields around the jet can be clearly seen from the plasma β parameter, as plotted in fig. 4.8 . Indeed, because the thermal pressure tends to decrease in the outer part of the jet, while the magnetic field increases, the plasma β is reaching a very low value in the envelope, around ~ 0.3. A cross-comparison with fig. 4.6 showed that the envelope is filled with gas flowing along with the inner jet core with a speed corresponding to $M \simeq 0.5$. Fig. 4.9 is a zoom in of the previous picture showing two different regions of the jet, highlighted in fig. 4.8 4.2.2 . It can be seen that the envelope is quite sharply defined, and extends up to approximately 2 jet diameters from the jet axis. We

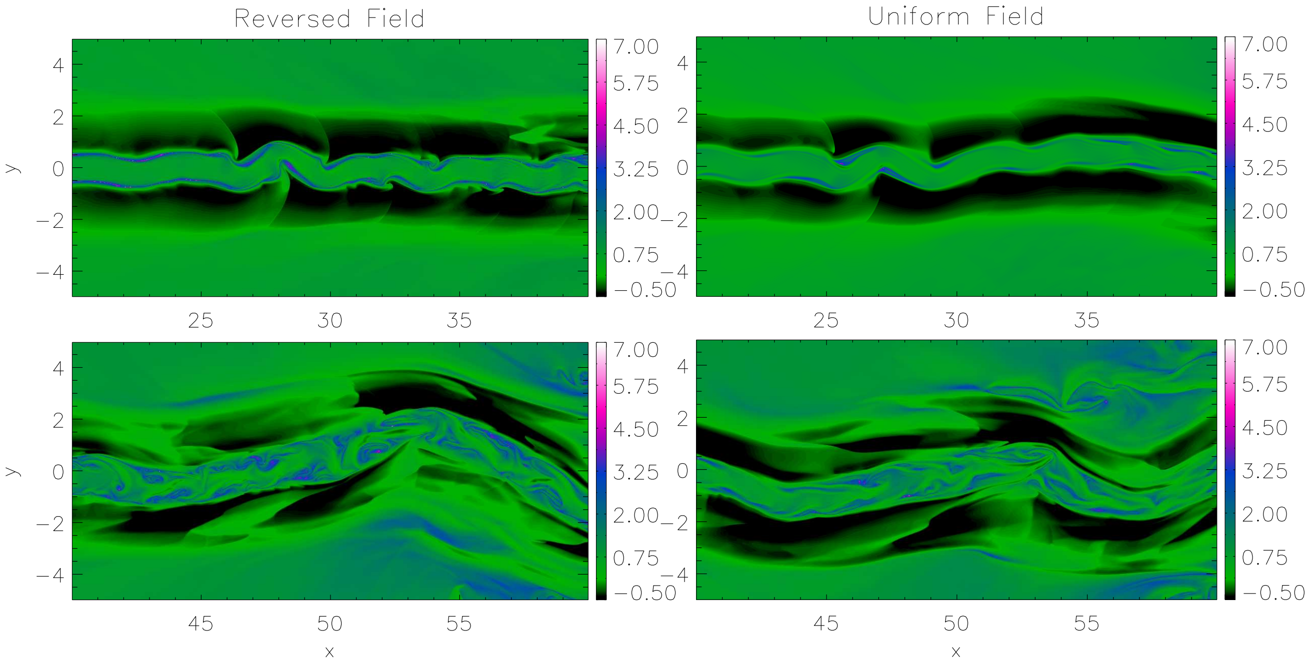

Figure 4.9. Plots of the plasma β in the domains defined by the boxes of fig. 4.2.2. *Upper panels*: yellow box. *Lower panels*: Red box. *Left Panels*: Reversed field simulation. *Right Panels*: Uniform field simulation. The color scale is logarithmic. The upper and lower values have been chosen to highlight structures and to allow direct comparison between the plots.

could not find a clear explanation for such sharp transition between the envelope and the outer medium. It is possible that the size of the envelope is influenced by the disruption of the jet at previous stages. Indeed, let two parts of the jet be A and B, with A flowing ahead of B. A will be disrupted before B, therefore B is flowing into a plasma configuration created by the disruption of A. The presence in the envelope of a velocity, comparable to the residual final velocity observed in the temporal simulations, supports this hypothesis.

Finally, fig. 4.9 is used to compare the simulations with antiparallel and uniform magnetic fields. The similarities are striking. As mentioned before, the general behavior of the jet in the two simulations is the same. In the upper panels of fig. 4.9 , we can see that the reversed field case presents a somewhat richer structure of the rim of the jet, while the uniform field case is more smooth. In addition, the boundary of the jet in the reversed case is defined by a higher value of the plasma β. This is the case because that is the position of the magnetic field reversal, where the field is actually zero. The only difference present in the lower panels, is a slightly lower level of turbulence inside the jet in the uniform field case.

4.3 3D Jet simulations

The simulations presented here are the three-dimensional extension of the slab jet simulations in sec. 4.2.2. As we discussed before, the spatial simulations are very computationally expensive. For reasons that will be clear during the discussion, going from 2D to 3D allows to reduce the

Table 4.1. Summary of the 3D simulations

Run	M	M_a	a	Domain L_xx$2L_y$x$2L_z$	Resolution
Pr1	3	7	0.2	80x11x11	800x110x110
Pr1	3	7	0.3	80x8x8	1280x128x128

domain size by a factor 2 in the y and z directions. However, 3D simulation with the same spatial resolution and domain length as a the slab 2D ones presented before, would require approximately 525000 CPU hours each (almost 60 years on one processor). With the best supercomputers available, this is possible. The main problem would be to analyze the data, since each file would be as big as 40 Gigabytes. In few words, the resolution had to be drastically reduced, in order to be able to perform the simulations in a reasonable time and with data sizes manageable by today's computers.

We performed two simulations with slightly different domains and resolutions, summarized in table 4.1. In the first simulation we run, dubbed Profile1, or Pr1, the domain is defined as before by $0 \leq x \leq L_x$, $-L_y \leq y \leq L_y$ and $-L_z \leq y \leq L_z$, with $L_X = 80$ and $L_y = L_z = 5.5$. The resolution is 800x110x110 grid cells. The parameters are $M = 3$, $M_a = 7$ and $a = 0.2$. We decided to run a second simulation with slightly better resolution and a different shear layer thickness. For this simulation, called Pr2 in what follows, $L_X = 80$ and $L_y = L_z = 4$, while the resolution is 1280x128x128. It follows that the simulation Pr1 has a thin shear layer, while Pr2 has a thicker shear layer.

4.3.1 Thin shear layer simulation

The Pr1 run has exactly the same parameters as the 2D spatial runs of sec. 4.2.2, and we used it to verify if the behavior and the magnetic field enhancement observed in 2D are still present in a three-dimensional configuration. We anticipate that, with some differences, the global behavior is the same.

In fig. 4.10 4.3.1 , we can see a sequence of 2D cuts of the density on the $(x,\, y)$ plane at different times. The similarities with fig. 4.10 and fig. 4.3 - 4.4 are evident. The perturbations at the inlet of the jet, visible in the first panel of fig. 4.10 , are indeed very similar to the high and low density regions of the first panel of fig. 4.3 . The growth of body modes in the beam gives rise to a sinusoidal pattern, visible in the second snapshot of fig. 4.10 . This structure appears as a helical deformation in three dimensions. Fig. 4.11 shows a volume rendering of the x component of the velocity in the region $50 < x < 65$, and highlight the three-dimensional structure. The beam is consequently disrupted, and form a low density turbulent region visible in the third and fourth panels. At 70 time units, the jet can propagate only to $x \sim 40$ before being disrupted. The last panel of fig. 4.10 , shows that the jet revives, and is able to propagate up to $x \sim 70$. The structure of the velocity at the end of the simulation presents a rough helical

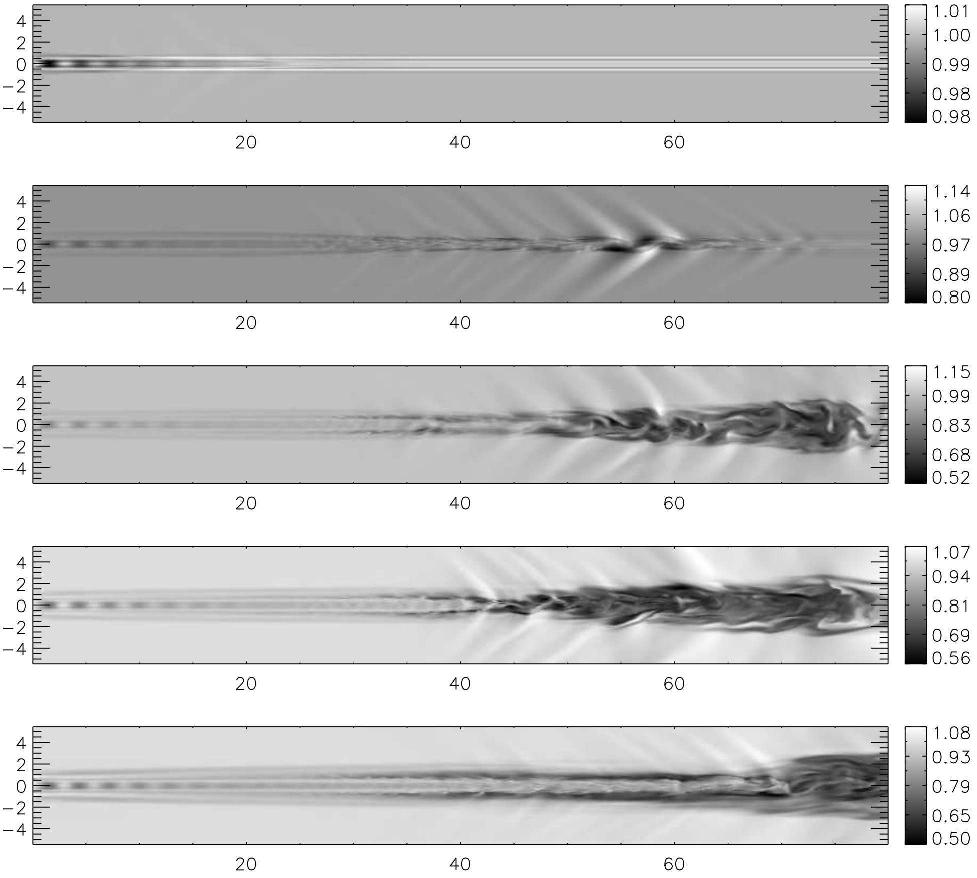

Figure 4.10. Two-dimensional cuts of the density in the $(x,\, y)$ plane of the Pr1 run at different times. From top to bottom: 10, 30, 50, 70, and 100 time units. Light tones correspond to higher densities.

shape, showed in fig. 4.12 .

The revival of the jet and its enhanced stability are related to the same mechanism observed in 2D, namely the magnetic field enhancement around the beam. Indeed, the parallel component of the magnetic field at $x = 40$, at the end of the simulation, is amplified by 50% over its initial value, as shown in fig. 4.13 . Around the jet, an envelope with high magnetic fields and low density is formed, in analogy to the one observed in 2D.

We observed several differences between the 2D and 3D simulations, which we describe below.

- The perturbation at the inlet of the jet creates a pattern of high and low density regions at the beginning of the simulation. As time goes on, these structures grow in intensity in the 3D simulation, but not in the 2D simulations. Instead, a series of weak waves, both inside and outside the beam can be observed.

- The disruption of the jet in 2D extends sideways up to more than 8 jet diameters. In

Figure 4.11. Volume rendering of the x component of the velocity in the region $50 < x < 65$, at $t = 30$. Light colors correspond to higher values. For a stereoscopic version of this image see Appendix C

the 3D runs the disruption is usually smaller than 3 jet diameters. The intrinsic three-dimensional structure of a kinking jet justifies this difference, since the beam is not forced to move on a plane, but can deform in space.

- The magnetic field enhancement is less effective in 3D than in 2D simulations, as shown by the comparison of fig. 4.12 and fig. 4.7 . It is important to note that the 3D simulations were stopped at 100 time units, while the 2D ones run up to 150 time units. Nevertheless, a comparison at 100 time units gives the same results. A possible reason for this difference is the three-dimensional nature of the kink deformation of the jet, which distributes the lateral compression over the whole jet circumference, and not just on a plane, like in the 2D simulations.

- The amount of structures visible in the 3D simulations is lower than in the 2D ones. This is not a surprise, since the resolution is lower for the 3D runs.

During the analysis of the data from this simulation, unfortunately we noted the presence of a possible numerical artifact, that we describe in the next section.

Figure 4.12. Volume rendering of the x component of the velocity in the region $40 < x < 80$, at $t = 100$. Light colors correspond to higher values. For a stereoscopic version of this image see Appendix C

4.3.2 Thick shear layer simulation

Fig. 4.14 shows a series of cross sections of the x component of the jet velocity, for the two 3D runs Pr1 and Pr2. In the first four cuts on the left in the upper panel (Pr1), we can observe four tiny, faint filamentary structures, aligned with the cartesian grid. The overall picture resemble a “star” and the filamentary structures are its “rays”. These “rays” are quite extended (about one jet diameter), and appear early in the simulation, already at $t = 10$. The jet deformation may be similar to a filamentation mode with $n = 4$, but the alignment with the axis makes them very suspicious. They are probably caused by the poor resolution employed to map a curved surface on a cartesian grid, together with the limited number of points used to resolve the velocity gradient in the shear layer.

To try to address this problem we run another simulation, Pr2, with a slightly higher spatial

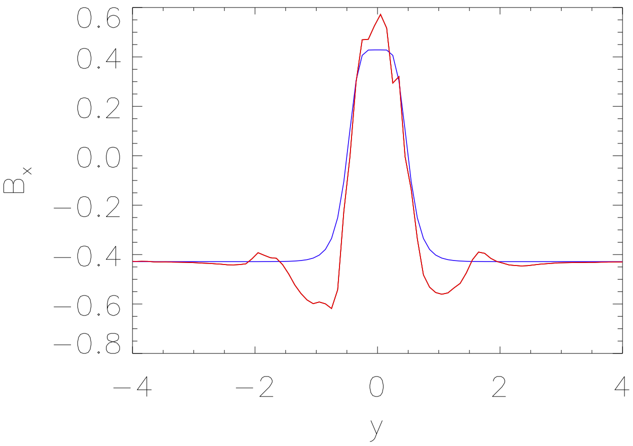

Figure 4.13. Cut in the y direction of the magnetic field at the position $x = 40$. *Blue*: Initial configuration. *Red*: end of the simulation.

resolution and a thicker shear layer, thus increasing the number of points used to resolve the velocity gradient. At the beginning the situation seemed better: the "rays" did not appear early in the simulation, but only after $t = 30$. Moreover, they seemed more diffused and therefore less prominent. However, because we changed the thickness a of the shear layer, the stability properties of the beam changed. Temporal studies in two dimensions have demonstrated this effect both for transonic and supersonic flows (Baty & Keppens 2006). The jet, in our case, did not show any body mode or internal relevant structure anymore. As a consequence, the "rays" could dominate the evolution of the jet. In the lower panel of fig. 4.3.2, we can clearly see how the numerical artifacts form near the inlet, and are transported by the flow while growing and ultimately destroying the beam.

The overall evolution of the Pr2 run shows a beam that is rapidly disrupted after $t = 40$ and is basically never able to propagate farther than $x = 50$. In fig. 4.15 , we show a volume rendering of a tracer of the jet material. Up to $x = 40$, the beam is flowing almost uninfluenced by the instabilities. In the region $40 < x < 60$ the beam undergoes a turbulent phase that mixes it with the ambient medium and gives it a clumpy appearance. Finally, in the region $60 < x < 80$, the jet material is completely mixed with the ambient medium and only some filament-like structures and small clumps are present.

We must stress the point that the jet never shows signs of revival after the initial disruption. The beam is not deformed following a helical pattern, and no compression of the external medium is exerted by the jet. As a consequence, no magnetic field enhancement is observed. Paradoxically, the jet does not maintain a coherent structure as far as the Pr1 run, because no body modes were able to grow. This simulation, actually, proves that the stabilizing effect due

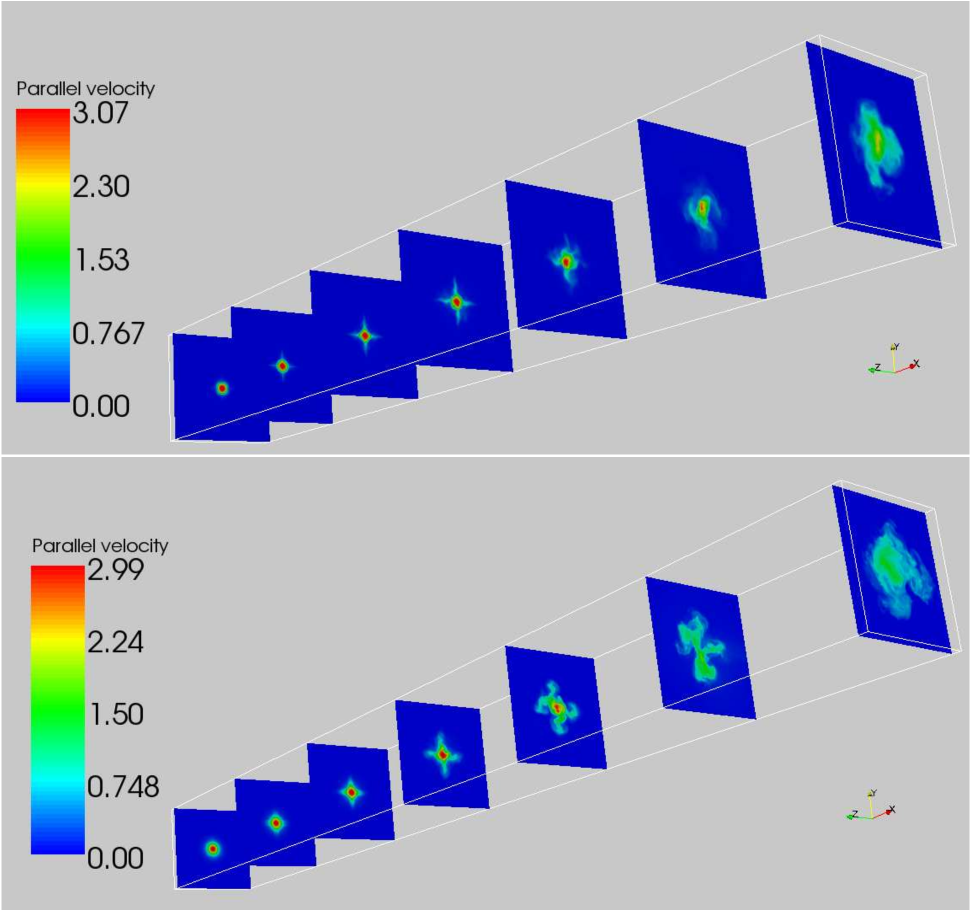

Figure 4.14. Cuts of the parallel component of the velocity at 100 time units. The different cuts are performed at x = 1, 14, 27, 40, 53, 66 and 79. *Upper panel*: Simulation Pr1. *Lower panel*: Simulation Pr2.

to the magnetic field enhancement requires the growth of internal unstable modes. Whether both kinking and pinching modes can excite a magnetic field amplification, remains an unsolved question, that would require more simulations to be addressed.

Figure 4.15. Volume rendering of a jet material tracer, at the end of the simulation Pr2. For a stereoscopic version of this image see Appendix C

Chapter 5

Conclusions

The central topic of this thesis was the stability of astrophysical jets. Indeed, astrophysical jets show a remarkable collimation and the ability to propagate through the external medium for distances up to hundreds of jet radii. The models of plasma beams predict a series of different instabilities, the effect of which is the violent disruption of the flow. In such a picture, jets would not be able to reach the observed lengths. These results, however, start from simplified models and assumptions, and there is still a lot of room for improvements. The ways in which jets survive MHD instabilities, are still not completely clear. Several stabilizing influences are discussed in literature (Hardee 2004): from steep gradients associated with jet acceleration or expansion, to big density contrasts between the jet and the ambient medium, to favorable radiative effects. The presence of opportunely ordered weak magnetic fields is also considered. This thesis was directed to investigate the role of a particular magnetic field topology, antiparallel fields, on the stability properties of astrophysical jets, with particular emphasis on the understanding of the Kelvin Helmholtz instability. The magnetic topology employed, indeed, is an outcome of several models of astrophysical jet formation.

5.1 Summary

Our results can be summarized as follows. We have investigated the stability of transonic and supersonic flows with the aid of direct MHD numerical simulation in two and three dimensions. Initially we have studied the KH instability of a single shear layer, with the aim to model the interface of a jet with the ambient medium. This was achieved performing MHD simulations of single modes of the instability, and of extended shear layers to observe the interaction of several modes. In addition we performed 3D simulations of single modes of the instability to address the generality of our 2D results. We followed this study with a series of simulations of plasma beams employing a 2D slab geometry and a full 3D realization of a cylindrical beam. We carried out the simulations both in a temporal and a spatial approach, in order to evaluate the differences in the results and to be able to understand the various aspects of the instability.

Single shear layer simulations

The simulations of a magnetized shear layer, considering one single mode of the instability presented interesting results starting from the linear phase of the evolution. Indeed, with the particular sheared profile of the magnetic field employed, the magnetic field strength is null exactly at the shear plane, and is gradually increasing with the distance from the plane. In such a way, the magnetic tension is zero, or very small, immediately near the shear layer. As a consequence the initial growth of the instability is not heavily influenced by the magnetic field strength. This reasoning was confirmed by our results from the simulations using the linear code LEDAFLOW. Indeed, we found growth rates always greater than in the uniform field case, especially in the regime $M_a < 5$ (strong magnetic fields). Moreover, we observed that the instability is characterized by a typical oscillation wavelength, close to the hydrodynamic case, in perfect agreement with our physical intuition.

The non-linear evolution of the KH instability, investigated with the aid of the MHD code PLUTO, presented significant differences as compared to a case with uniform magnetic field. First of all, a non-linear stabilization mechanism, identified in the uniform field case to operate in the regime $2 \lesssim M_a \lesssim 4$, is absent in the reversed field case, and the development of vortical motion is observed for $M_a > 2$. Moreover, the presence of tearing type magnetic islands around the perimeter of the KH vortex proved to be driven by the KH instability itself. This fact is relevant, because the islands use up magnetic energy to grow, at the expense of the magnetic field expelled from the centre of the vortex by the vortical motion. The consequences are lower magnetic saturation energies as compared to the uniform case, and a delay of the decrease of the plasma β (and therefore of the magnetic amplification proper of the KH instability).

The final state of our simulations is drastically different from the uniform case as well. Indeed, in the reversed field case, a big magnetic island is formed at the centre of the domain, a clear outcome of the initial antiparallel magnetic configuration. Such ordered structure reduces the disruption level of the flow due to the instability by a factor of $\sim 10\%$ for low magnetic fields ($M_a > 7$). The opposite is true for the strong magnetic regime, with greater disruption levels, caused by the development of vortical motions absent in the uniform case.

The simulations of the extended shear layer were aimed at the investigation of the interaction of several modes of the instability. Our results showed that the KH instability of a shear layer embedded in a reversed magnetic field presents the same inverse cascade process observable in the uniform field case, characterized by pairing/merging processes towards large scale structures. Indeed, the vortices develops accordingly to our linear study and start to merge to form bigger structures. The process is enriched by the presence of the magnetic island mentioned before, which gives the final state of the plasma a more turbulent character with respect to the uniform field counterparts. The final disruption level is much greater than what found for a single mode of the instability, because of the merging process. As a consequence, the effects of the KH instability on astrophysical flows cannot be underestimated. The final disruption level is, however, quite similar to the uniform field case. We must note that the regime of very strong fields, $2 \lesssim M_a \lesssim 2.5$ is characterized by the fast formation of magnetic island from the KH vortices. As a consequence, the nature of the subsequent evolution is completely different and is dominated by the interaction of magnetic islands.

We concluded our study of single shear layers with a number of 3D simulations. Our results showed that the evolution of the KH instability is mainly two-dimensional up to the saturation time. The perturbations applied to the shear layer evolved into a KH cylindrical roll, but any section perpendicular to its axis looks exactly the same. We could also observe the formation of magnetic islands around the roll in analogy to the driven islands seen in 2D. Growth rates and kinetic saturation levels are also very similar to the 2D case.

After the saturation time, however, three-dimensional effects start to dominate and eventually destroy the KH roll. Indeed, we observed elongated structure corrugating the perimeter of the vortex, possibly being “rib” vortices. These structures are the location of an additional magnetic field amplification process, observed in the uniform field case by Ryu et al. (2000). The presence of magnetic islands in our simulations, however, actively interfere with this process. The resulting magnetic field at the border of the vortex is then weaker than in the uniform case. This is important because a strong enough field can reorganize the system into a laminar flow. This is observed in the uniform case for $M_a \lesssim 50$. The lower effective magnetic field in the antiparallel case moves this threshold to $M_a \lesssim 20$. If theAlfvén Mach number is greater than this value, MHD turbulence sets in.

Jet Simulations

Regarding the jet simulations, initially we performed temporal simulations of slab jets embedded in an antiparallel magnetic field reversing at the jet boundary. This configuration is a natural extension of the one used for the single shear layer. We found that the reversed field did not alter drastically the known results for uniform magnetic fields from other authors (for example Baty & Keppens, 2006). Our supersonic jet configuration proved to be unstable to sinuous body modes, which evolved rapidly to completely destroy the flow. The various magnetic field strengths employed allowed us to evaluate the effects of the field on the instability. We found that the time of disruption of the flow increases with the field strength. Moreover, the width of the residual flow is smaller for strong magnetic fields.

Our results for the 2D spatial simulations showed initially a dominance of sausage body modes, in contrast to the temporal simulations. However, the modes later evolved to sinuous modes, partially thanks to secondary convective instabilities only observable in a spatial approach. The wavelength of the most unstable mode dominating the unstable behavior has a value of ~ 4 jet diameters, in partial agreement with other works (Ferrari, 1998, Baty & Keppens, 2006). The wavelength of the instability is observed to change to longer values during the course of the simulation.

The jet is episodically disrupted by the KH instability resulting in a large turbulent region, but is then revived and can propagate through the material left by the previous disruption, maintaining a certain collimation and coherence. This enhanced stability is due to a mechanism of enhancement of the magnetic field, previously believed to work only for sub- and trans-sonic flows (Viallet & Baty 2007). Indeed, the plasma is compressed just outside the jet as a consequence of the strong bending induced by the sinuous mode of the KH instability. The perturbations generated in such a way can propagate upstream by means of Alfvén waves, thus leading to a partial stabilization.

We also performed a simulation with a uniform magnetic field in order to compare the results. The two simulations are extremely similar, both in terms of unstable modes and non-linear behaviors such as the mentioned magnetic amplification. Our simulations, threfore, greatly lessen the importance of antiparallel magnetic fields in astrophysical jets.

The main result of the 3D simulations we performed, is that the behavior is quite similar to the 2D one. The sinuous modes transform in a 3D kink, the episodic disruption and revival of the beam is still present, as well as the magnetic field amplification. There are, however few differences related to the three-dimensional nature of the helical deformations: the side extension of the disruption is smaller than in the 2D case, and the magnetic field amplification is only $\sim 50\%$ against the $\sim 100\%$ of the 2D case.

To address some numerical problems we performed a 3D simulation of a jet with a thicker boundary layer. As a consequence the jet di not show any helical deformation and undergo rapid desruption. The simulation showed that a kinking deformation is required to enhance the magnetic field and thus the stability of the system.

5.2 Discussion

Role of the antiparallel magnetic field topology in astrophysical jets

We have proved that an antiparallel magnetic field has a significant effect on single transonic shear layers. Indeed, the final effect is a general enhanced instability, especially for high magnetic fields. One could argue that astrophysical jets are usually regarded as weakly magnetized, so the relevance of this result is small. On the other hand, magnetic fields are often invoked as a mean of stabilization against unwanted instabilities. In this view, the antiparallel magnetic field can no longer provide the same level of stabilization, especially because the non-linear stabilization process in the regime $2 \lesssim M_a \lesssim 4$ is lost, and the growth rates are not diminished as much as with a uniform field. One must also remember, though, that very strong fields ($M_a \ll 2$) would stabilize a single shear layer anyway.

The situation is not better in 3D, because weak antiparallel fields are not able to reorganize the flow as weak uniform fields can. Therefore antiparallel fields favor turbulence over ordered, laminar configurations.

The impact of the antiparallel topology on supersonic flows is however limited. Therefore we think it will not be possible to distinguish between uniform and reversed fields with observations of jets. The topology could have some effects on subsonic and transonic jets. Indeed, the magnetic amplification mechanism observed by Viallet & Baty (2007) is based on the vortices formed by the KH instability. Because the reversed field case presents a lower magnetic amplification for a single vortex, the amplification in a subsonic jet would be less efficient overall.

Role of the magnetic field amplification

The magnetic field amplification mechanism identified in our jet simulations is important for any magnetized jet. If this is indeed one of the processes that allows astrophysical jets to propagate for the very long observed distances, it would require all the jets to undergo helical deformations, although more study is necessary to determine if the mechanism is active also for pinching modes. Based on the (few) physical informations coming from the observations, this concept would allow, together with a model, to constrain some jet parameters typically involved in the stability behavior, such as Mach number, Alfvén Mach number, thickness of the shear and density ratio between jet and ambient medium. More realistically however, we suppose that this mechanism is not determinant for the stability of jets, but can, in some cases be important. One interesting idea is for example to use the magnetic field amplification at the jet boundary to produce enhanced synchrotron emission in extragalactic jets, thus explaining the observed lim-brightning.

Possible model improvements and future prospects

By far, the most important improvement that has to be considered is the inclusion of toroidal magnetic fields. As we discussed in the introduction, one of the most popular and succesfull mechanism of jet formation is the magnetocentrifugal acceleration, which naturally produces toroidal fields and collimates the outflow. The presence of toroidal fields would introduce current driven instabilities in the beam, complicating considerably the stability analysis. It would be anyway interesting to test the magnetic field amplification mechanism we described before against a CD unstable beam. The CD instability is generally characterized by kinking modes, so much that it is often called simply kink instability. Contrary to the KH instability, however, it is an absolute instability. This, together with the helical shape of the field lines, would probably transform the previous magnetic amplification process into a local enhancement only. Moreover, enhancing the field would enhance the currents, thus contributing to the destabilization of the flow.

The presence of helical magnetic fields opens the possibility of non-linear interaction with the CD and KH instability, as studied by Baty & Keppens (2002) for slightly supersonic flows. In this paper, the interaction was shown to be stabilizing for the flow. An extension of this work to fully supersonic regimes is therefore quite promising. It has to be noted, that the CD instability must be studied in three dimensions because of its natural predisposition to preoduce helical deformations. Moreover, the inclusion of moderately strong helical fields causes the presence either of pressure or magnetic gradients to satisfy the MHD equilibrium. A high resolution to properly resolve the gradients is therefore absolutely necessary, de facto making a spatial study almost impossible with today's computers.

Other improvements to the model could consist in the use of more realistic parameters and profiles for the variables. Astrophysical jets are generally supersonic, with Mach numbers higher than the value of 3 we employed in our calculations. A very high Mach number actually would reduce the importance of the KH instability, since the perturbations are advected with a fraction of the flow velocity. As a consequence they would propagate for very long distances before fully grow, thus not representing a threat for the jet survival. A density contrast with the ambient medium is also important, and its effects have been studied already by several authors (for example Bodo et al., 1994). It would also be interesting to improve the model of the ambient medium, to take into account the fact that the jet is actually propagating through a medium shocked by the bow shock or mixed with the backflow coming from the jet head.

In modelling jets from young stars, a key element is the energy lost by the system through radiation. The calculations for radiative cooling are quite complicated, because of the high number of coupled species involved, both atomic and molecular. Such calculations, however, allow for a direct comparison between simulations and observations. The main problem is the high computational cost related to the solution of such a problem, which increases the time needed for a numerical simulation by a factor ~ 10. In addition, the plasma is always considered optically thin. Attempts to introduce optically thick gas increase the computational costs even more.

Finally, an interesting study would be to introduce periodic or episodic ejections, instead of the steady outflow we considered. Several works have been published already, following this idea, trying to explain the knots visible in the observations of jets as shocks generated by the non-steady ejection (see for example Raga & Noriega-Crespo, 1992). The simultaneous presence of episodic flows and instabilities is somehow overlooked in the community, with only few published works (see for example Cerqueira & de Gouveia Dal Pino, 2001). This is, however, a promising idea that deserves furter study and attention.

Appendix A

Numerical Methods

A.1 Pluto

PLUTO (Mignone et al. 2007), is a finite volume, shock-capturing fluid dynamical code designed to integrate a system of conservation laws

$$\frac{\partial U}{\partial t} = -\nabla \cdot Y(U) + S(U), \tag{A.1}$$

where U represents a set of conservative quantities, $T(U)$ is the "flux" tensor and $S(U)$ define eventual source terms. An equivalent set of primitive variables V is more conveniently used for the initial and boundary conditions. The form of U, V, $T(U)$ and $S(U)$ depends on the physics module selected. The available modules are: hydrodynamics (HD), magnetohydrodynamic (MHD), special relativistic hydrodynamic (RHD) and special relativistic magnetohydrodynamic (RMHD).

The finite volume scheme is a method to represent and evaluate partial differential equations as algebraic equations. Value are computed at discrete places on a grid mapping a domain. Each point on the grid is surrounded by a small volume. In this method, volume integrals containing a divergence are transformed in surface integral, using the Gauss's theorem, and evaluated using fluxes at the surfaces of each volume element.

In the fluid dynamic codes of this type, the fluxes are computed starting from a interpolation or extrapolation of the physical variable on the cell edges. With these values, a Riemann problem is solved at each cell interface to obtain the fluxes, with which it is possible to advance the solution in time. For a one dimensional problem:

$$U^{n+1} = U^n - \frac{\Delta t}{\Delta x}(F_+ - F_-), \tag{A.2}$$

where F_+ and F_- are the fluxes, Δt is the time step, Δx is the grid spacing and U^n is the set of variables at the time n.

The reconstruction of the variables at the cell edges requires the use of slope limiters to avoid the introduction of spurious oscillations proper of high order spatial discretization schemes. In literature, there is a variety of different Riemann solvers and slope/flux limiters. Differences lies in the amount of simplifications introduced. Riemann solvers often cannot resolve one or more MHD waves for example. But to simplify, the choice of solver and limiters influences heavily the effective numerical diffusion introduced in the problem.

Solving the MHD equations with this method does not preserve the solenoidal constrain for the magnetic field, $\nabla \cdot \mathbf{B} = 0$, unless special discretization techniques are employed. The version of the PLUTO code we employed, allowed for two distinct methods. In the first one, called eight wave formulation, an additional source term is added to the MHD equations. The effect is that eventual monopoles are advected away with the flow. The second one, called Constrained Transport, is based on the direct integration of the induction equation using Stokes theorem and magnetic fields directly defined on the cells edges (staggered collocation).

A.2 Ledaflow

LEDAFLOW is a stability code, designed to integrate the linearized MHD equations in ideal or resistive form. This code is able to compute the characteristic waves and instabilities of a given 1D equilibrium, using a standard method with finite elements and inverse vector iteration technique (Nijboer et al. 1997). The equations are solved for perturbations having a classical normal mode expansion of the form $f(y)\exp(-i\omega t + k_x x)$. As a temporal approach is taken in the Ledaflow code, with a complex frequency $\omega = \omega_R + i\omega_I$ and a real longitudinal wavenumber k_x, the linear growth rate Γ of a mode specified by k_x is then obtained by taking the imaginary part of ω, $\Gamma = \omega_I$.

The MHD equations are linearized to be solved as an eigenvalue problem. The equations defining the eigenvalue problem are in the form

$$Lw = \lambda R w, \tag{A.3}$$

where w is he state vector and L and R contain equilibrium quantities and derivatives with respect to $u1$ only. The equations must be cast in a"weak" form. Following Finite Element Method, the equations are multiplied by a test function ν and then integrate over the domain [0,1].

The components of the vector w are all expanded in a finite number of basis functions, and the system of equations is reduced to a linear matrix eigenvalue problem.

Two possible methods to find the solutions are employed. The first follows a QR algorithm, which allows to obtain the whole spectrum of solutions of the initial problem. However, the number of grid points is limited. The second method, inverse vector iteration, calculates only one mode, but can be used together with a bigger grid.

Appendix B

Test on MHD Kelvin-Helmholtz Instability

B.1 References

The test was introduced as part of a study on Kelvin Helmholtz instabilities by Keppens et al. 1999 (J. Plasma Physics, vol.61, part 1, pp. 1-19). It is based on the results from Miura & Pritchett 1982 (J. Geophys. Res. 87, 7431). Further references are: Baty et al. 2003 (Phys. Plasmas, Vol. 10, No. 12), Malagoli et al. 1996 (Astrophys. J. 456, 708) and references within.

B.2 Test purpose

This test is designed to verify the general behavior of the Kelvin Helmholtz instability in a magnetised plasma, with different initial values of the magnetic field and to check if the numerical code can reproduce correctly the linear phase of the evolution of the instability. In particular the growth rates will be tested against linear theory predictions.

B.3 Test setup

We follow here almost precisely the Baty et al. initial conditions: ideal MHD equations, 2 dimensions, cartesian coordinates (x,y), grid of (x,y)= (200,600) points, periodic boundary conditions in the x direction, outflow boundary conditions in the y direction, problem domain: $0 \leq x \leq 1$, $-1.5 \leq y \leq 1.5$, $\gamma = 5/3$, $t_{stop}=100$. The initial conditions for the variables are the following:

$$\rho = 1 \qquad p = 1/\gamma$$

$$v_x = 0.5 \cdot M \cdot \tanh(y/a)$$

$$v_y = 0.01 \cdot \sin(2\pi x) \cdot exp\left(\frac{x}{4a}\right)^2$$

For the magnetic field:

$$B_x = B_0 \qquad B_y = 0$$

or, with the vector potential notation:

$$A_x = 0 \qquad A_y = 0 \qquad A_z = B_0 x$$

The problem has three parameters:

- a is the width of the shear and has to be small. In this test a will be fixed at: $a = 0.05$
- M is the sonic mach number and in this test will be constant: $M = 1$
- B_0 is the initial magnetic field strenght. Using the equations in cgs ($\mu_0 = 1$) and the normalization above ($\rho = 1$, sound velocity $c_s = 1$, $p = 1/\gamma$), one finds that $B_0 = \sqrt{4\pi} \cdot M/M_A$, with M_A being the alfvén mach number v/v_A. Note that in some codes the factor $\sqrt{4\pi}$ is included in the magnetic field and therefore is not needed.
  The test consists of four simulations with the following alfvén mach numbers: $M_A = 1$, $M_A = 3$, $M_A = 10$, $M_A = 40$.

As it will be clear from the next section, the test requires to plot some physical quantities as a function of time: therefore it is necessary to save the variables quite often. For the case $M_A = 10$, we prescribe to save all the physical quantities every 0.05 time units in the interval $0 \leq t \leq 10$, and every 1 time unit in the interval $10 \leq t \leq 100$. In this way a proper time resolution for further analysis is assured. For the other three cases, saving every 1 time unit is sufficient.

During the formulation of this test an issue emerged regarding the numerical methods used to keep $\nabla \cdot B = 0$.
Because the Kelvin Helmholtz instability is characterized by reconnection events in its evolution, it is strongly advised to use the best possible method to ensure a divergence-free magnetic field. For this reason the magnetic field is initialized using a vector potential and computed using $B = \nabla \times A$. $\nabla \cdot B = 0$ is then treated with the FluxCT procedure. Different methods, like eight wave formulations, can produce slightly different results at the end of the simulation: even if these differences are probably not affecting the linear evolution of the instability, they are indeed important in the long run and potentially lead to errors in jet simulations.

B.4 Test evaluation

The test consists of two main parts: a general behavior study of the instability as a function of the Alfvén mach number, and the comparison between the growth rates in the simulation and as expected from the linear analysis.

- Growth rates:

  Following Keppens et al. we determine the growth rate of the instability by monitoring the vertical kinetic energy $E_y = \int \int dxdy \frac{1}{2} \rho v_y^2$. Because the cells in the simulation have the same size, this integral is just the sum of the values over the whole domain. E_y is plotted versus time for the four cases.

  In the case $M_A = 10$, the first maximum of the energy, identified with the saturation level, is called E_{max} and corresponds to a value of time t_{max}. The curve $E_y(t)$ should then be fit with an exponential $exp(2\Gamma t)$ in the interval $t \in [0.25 t_{max}, 0.4 t_{max}]$. Here Γ is the wanted growth rate. To simplify the fit, it is possible to produce a semilogarithmic plot ($log(E_y)$ versus time) and perform a linear fit: the angular coefficient is twice the wanted growth rate.

  Following the notation in Miura and Pritchett, Γ has to be multiplied by $2a/M = 0.1$ to be able to compare the results: the expected value, extrapolated from a plot, is $\Gamma \frac{2a}{M} = 0.135$. To pass the test, the MHD code should provide a result $\in [0.125, 1.45]$.

- General Behavior:

  As described for example in Baty et al. , the evolution of the Kelvin Helmholtz instability is different for different strenghts of the magnetic field. The choice of M_A for the test simulations has been done in agreement with the four regimes described in Baty's paper.

  When $M_A \leq 2$ the problem is linearly stable: No vortex should be formed and the kinetic energy along the y direction should decrease in time.

  When $2 \leq M_A \leq 4$, the shear is linearly unstable, but the perturbation can enhance the magnetic tension thus providing stabilization. In this case the vertical kinetic energy is expected to grow exponentially in the first phase, and after a short time to decrease again rapidly. If the magnetic field is weaker, then the formation of a vortex and subsequently of a structure similar to the classical cat's eye is allowed and we still distinguish between two cases.

  When $4 \leq M_A \leq 20$ the cat's eye is rapidly disrupted, and for $M_A \geq 20$, the instability evolution is essentially hydrodinamic, with enhanced dissipation.

  In this section of the test, the numerical code should provide general results in agreement with literature. A series of results is provided in the next section.

A remark on the boundary conditions and the grid type should be done here: outflow boundary conditions are in most codes suitable for supersonic flows only. In this test the flow is trans-sonic and therefore waves can be reflected along the outflow boundary surface. This issue is not heavyly affecting the linear evolution of the instability, but may be important in the following turbulent phase. The number of grid points and the boundary values in the y direction were chosen so that this effect is not affecting too much the final result. Nevertheless, to obtain better results one can modify the domain of the simulation adding two patches of non-uniform grid with few points covering a big domain, so that the size of the cells gradually increase from the central to the outer part of the domain. With this setup, any wave produced must travel a long way to reach the boundary and, if reflected, to affect the central part of the simulation, thus reducing drastically the problem of the boundary. This particular setup is not required because is not the primary focus of the test, but if a code can provide support for advanced grid setups this will count as a positive mark in the results.

A final comment on the divergence of B: in the next section it will become clear that eight waves methods cannot provide results in complete agreement with literature. If a code can reproduce the correct growth rates but can not handle a very robust divergence cleaning algorithm, this fact will be remarked as a negative point in the results.

B.5 Results

The results provided in this section have been obtained with the PLUTO code from A.Mignone (http://plutocode.to.astro.it) using a Roe Riemann solver, and are presented as an example for the test.

In particular, figure 1 is the graphical representation of the method to get the growth rate and figures from 2 to 5 are a series of plots of the total kinetic energy along the y direction to show the different behavior of the instability as a function of the Alfvén Mach number.

Finally a short comparison of the results obtained using different methods to ensure $\nabla \cdot B = 0$ is presented in figures 7 and 8: when the eight waves method is used, at the end of the simulation one can notice clearly three zones with different velocities in the x direction, separated by regions of irregular variation. Note also that the central part is quite broad and substantially not moving. On the other hand, using the FluxCT method, the velocity is smoothly changing over the domain and only the small zone of the shear is at rest. Also the Evolution in time of the total kinetic energy in the y direction is different as it appears from figures 4 and 9: the energy does not go to zero if eight waves method is used and the second peak is higher.

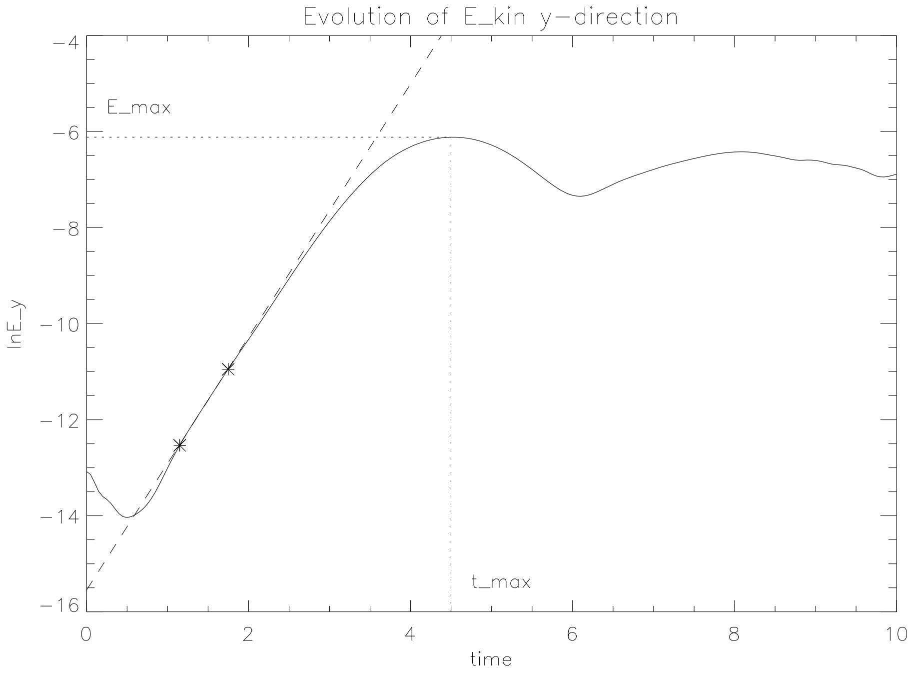

Figure B.1. Logarithmic plot of the total kinetic energy along the y direction. Also shown are the saturation level E Max and the corresponding time t Max. The growth rate of the instability is obtained from the linear fit in the interval [0.25t Max, 0.4t Max], represented by the dashed line.

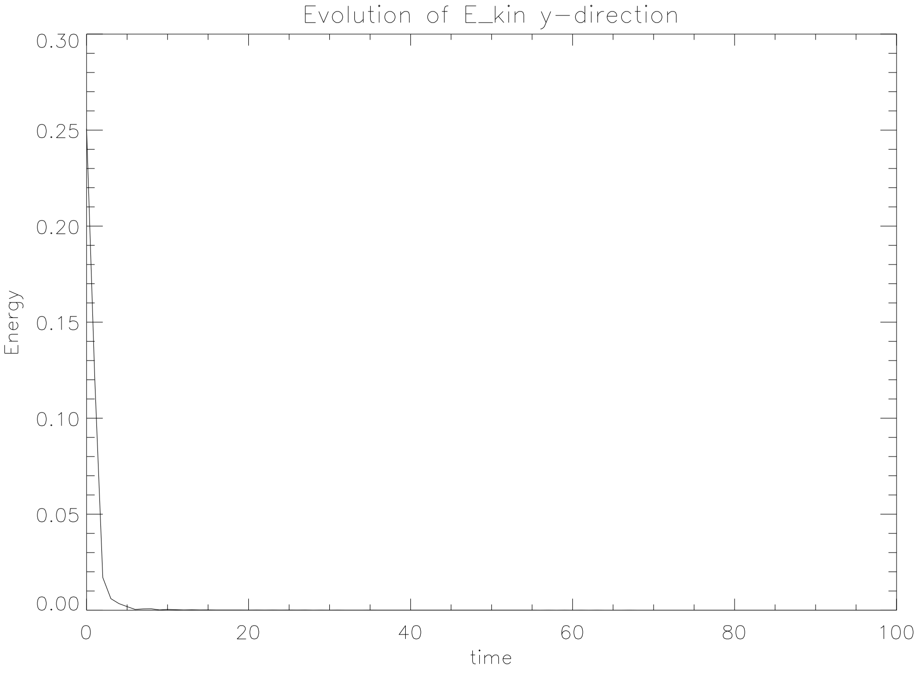

Figure B.2. Total energy evolution in the case of Alfvén Mach number = 1.

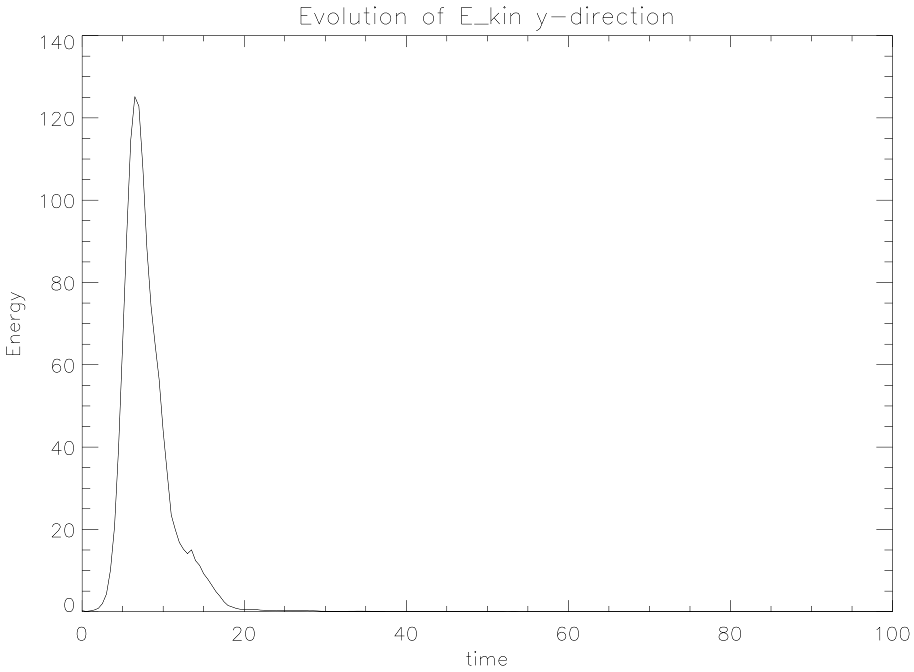

Figure B.3. Total energy evolution in the case of Alfvén Mach number = 3.

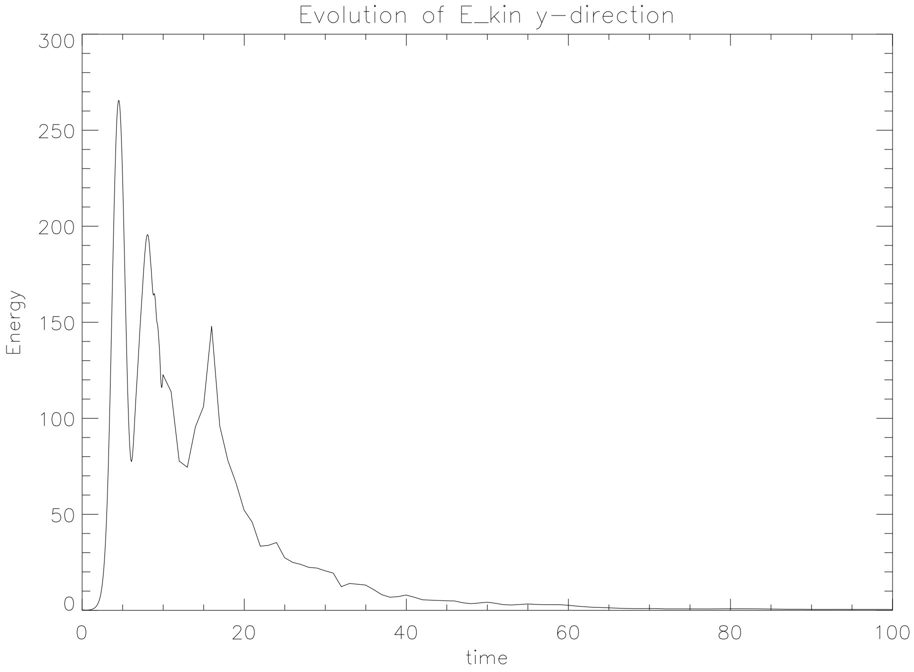

Figure B.4. Total energy evolution in the case of Alfvén Mach number = 10.

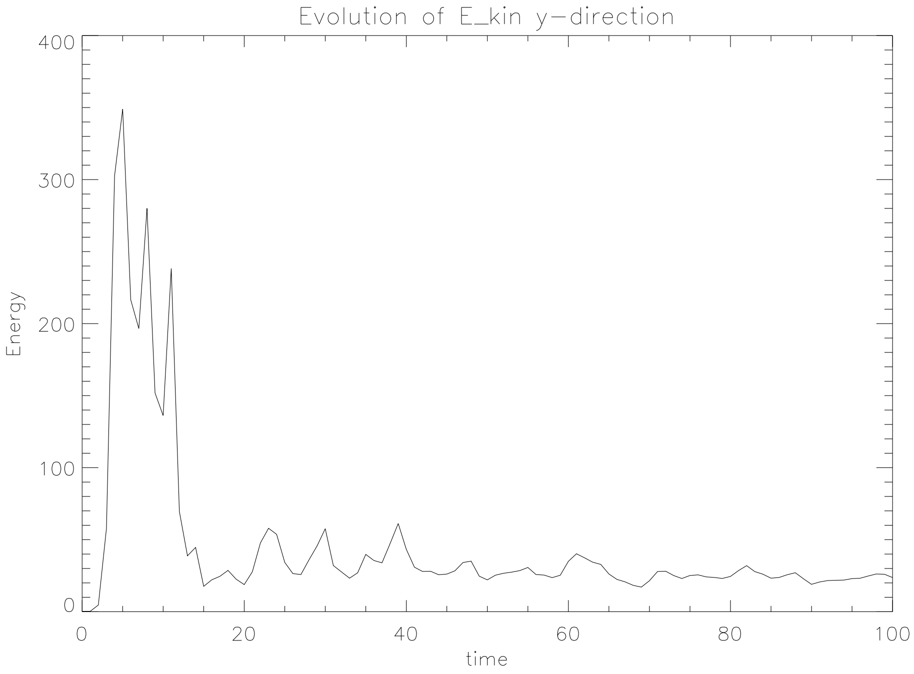

Figure B.5. Total energy evolution in the case of Alfvén Mach number = 40.

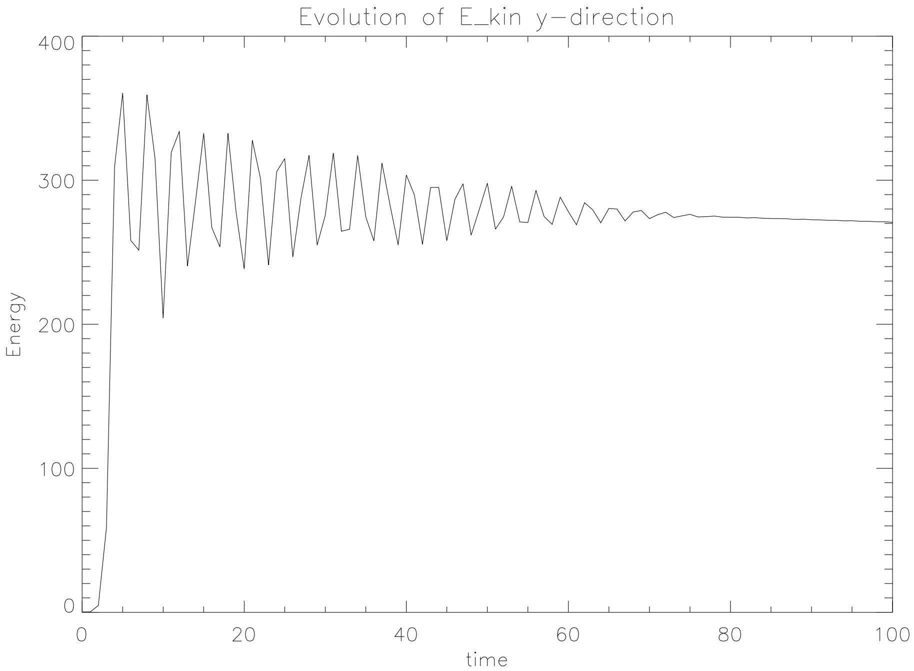

Figure B.6. Total energy evolution for a pure hydrodynamic case.

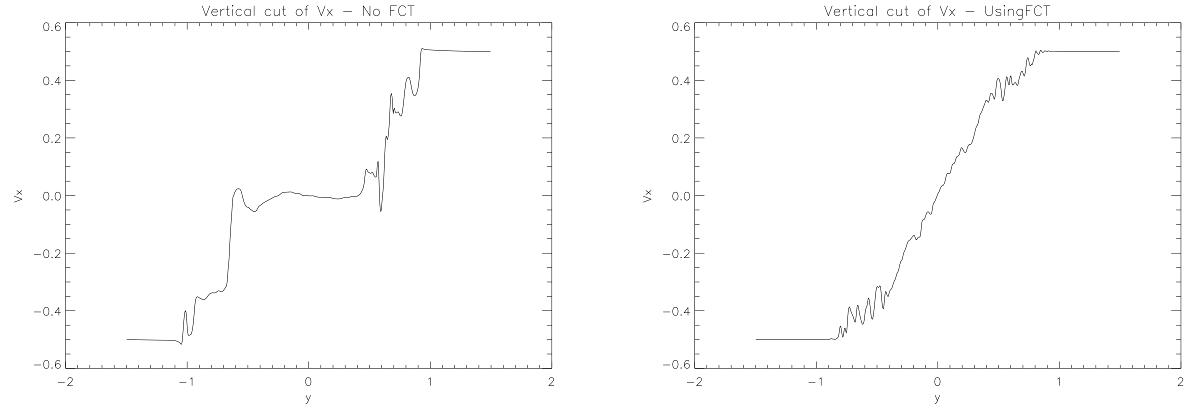

Figure B.7. *Left.* Velocity along x direction in the case of Alfvén Mach number = 10, at the end of the simulation: cut along a vertical line x=0.5. Eight waves method was used to treat divergence of B. *Right.* Same as the Left image, but using FluxCT method.

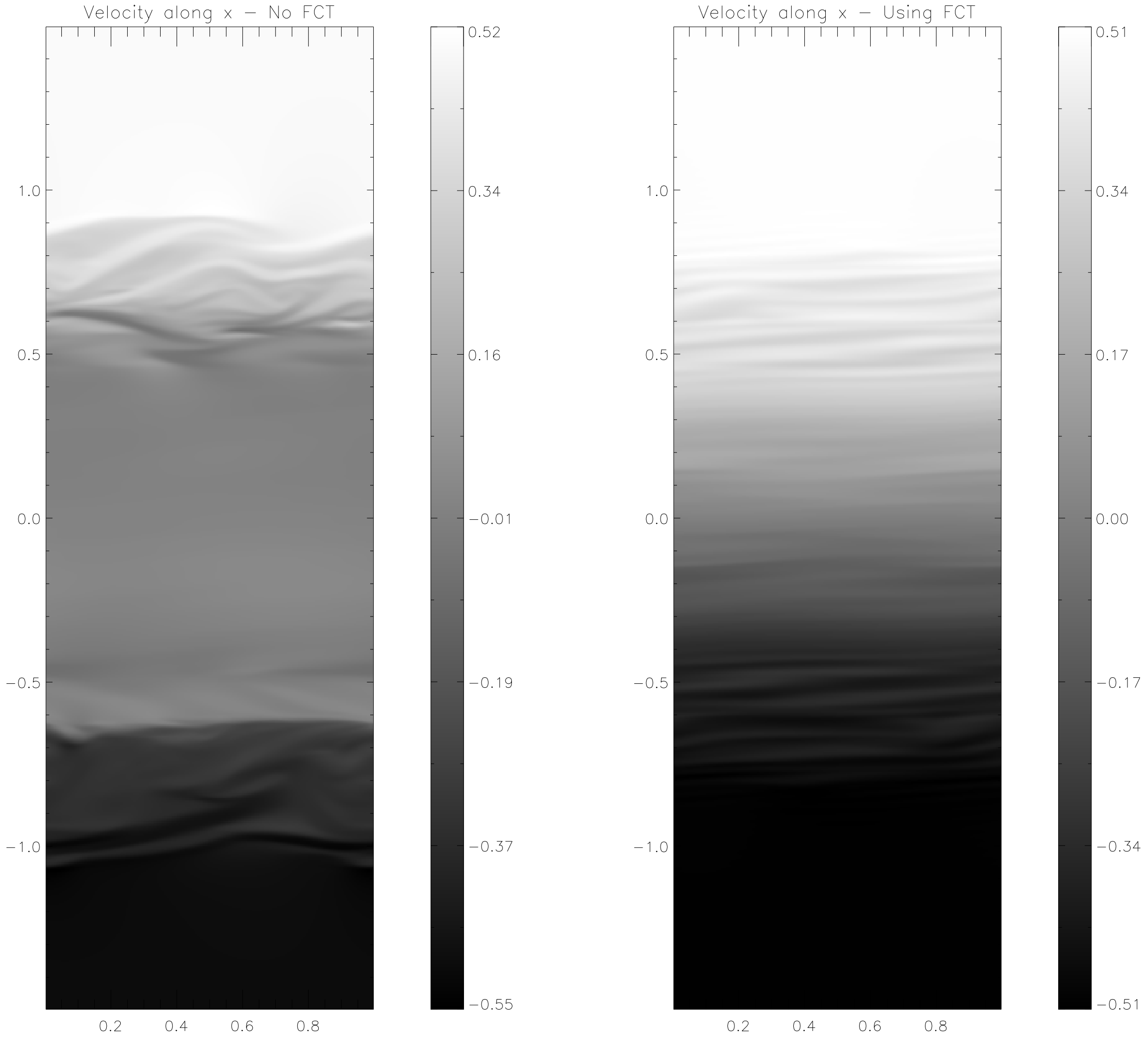

Figure B.8. *Left.* Velocity along x direction in the case of Alfvén Mach number = 10, at the end of the simulation. Eight waves method was used to treat divergence of B. *Right.* Same as the Left image, but using FluxCT method.

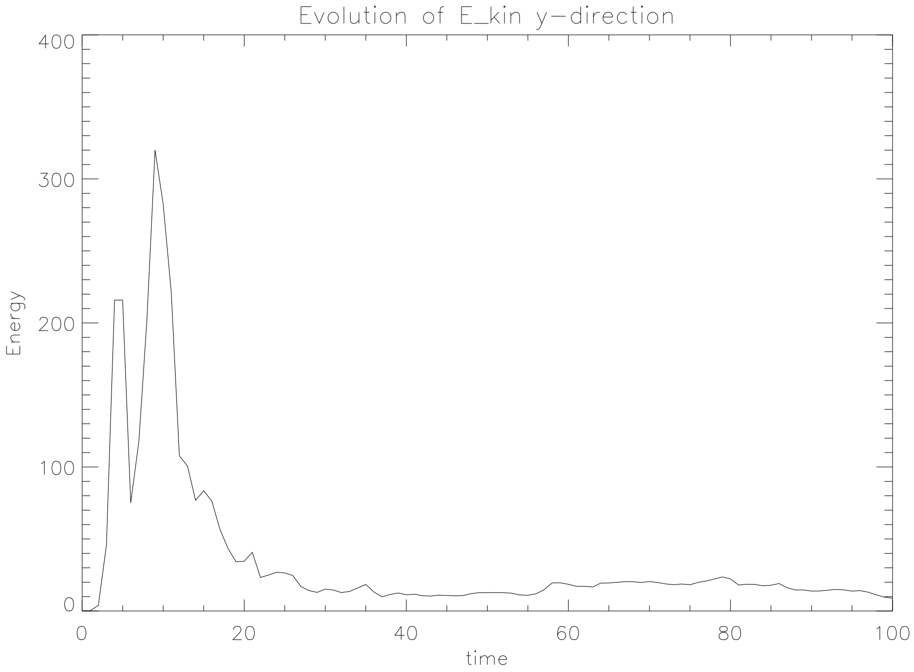

Figure B.9. Total energy evolution in the case of Alfvén Mach number = 10, using the eight waves method for the divergence of B.

Appendix C

Stereoscopic images

In this appendix we collected some 3D pictures, which can be viewed in a special way, to give a sensation of three dimensionality.

How to view the images

1. Look at one couple of images at a time: one image on the right, one on the left.
2. Cross your eyes, like you are looking at the tip of your nose. You will see not 2, but 4 images.
3. Change the ammount by which your eyes are crossed, so to see only 3 images (two images out of four are now superposed in the centre of your view)
4. Keeping the position of the eyes fixed, try to focus on the central image

warnings

- It may be impossible to see a three dimensional effect for people affected by astigmatism.
- longed viewing sessions may cause head-ache and are very tiring for the eyes.

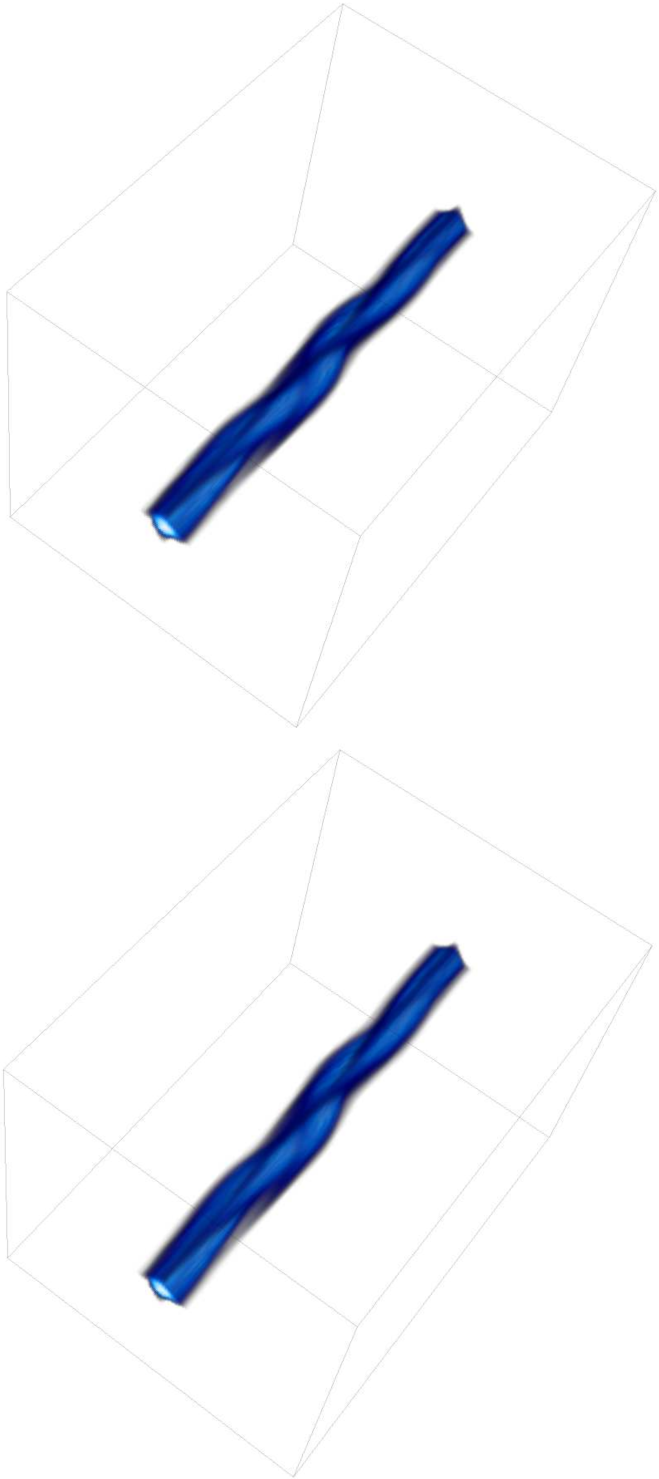

Figure C.1

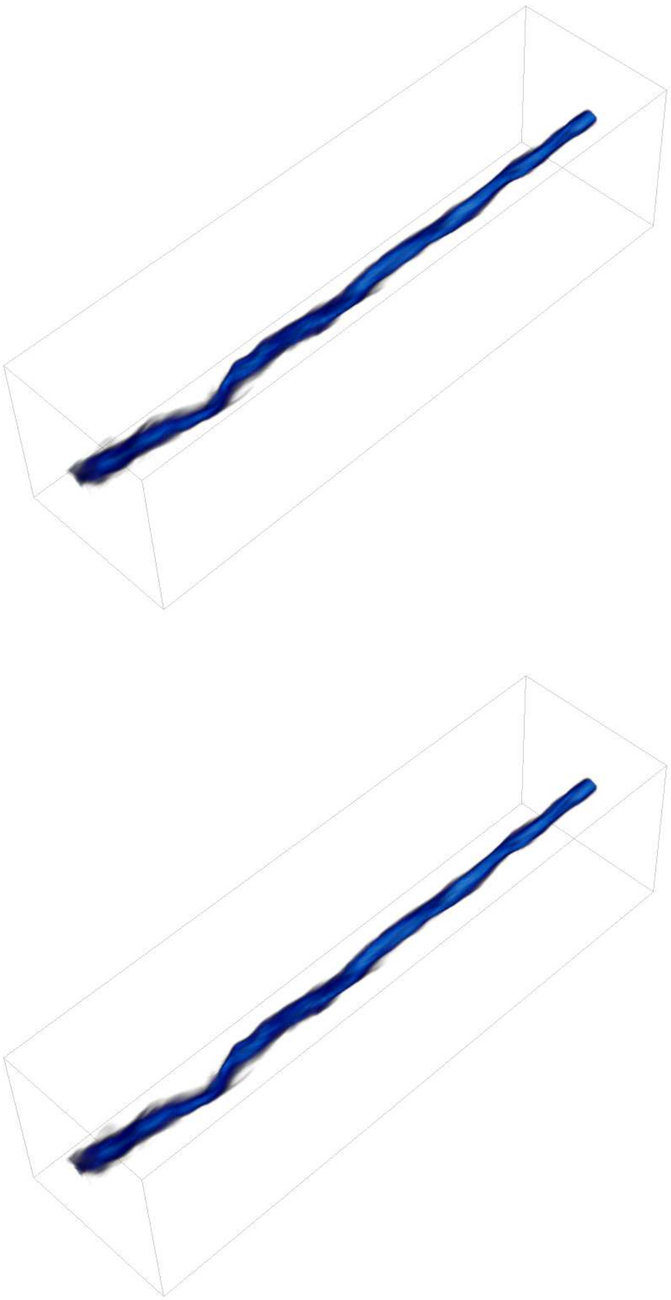

Figure C.2

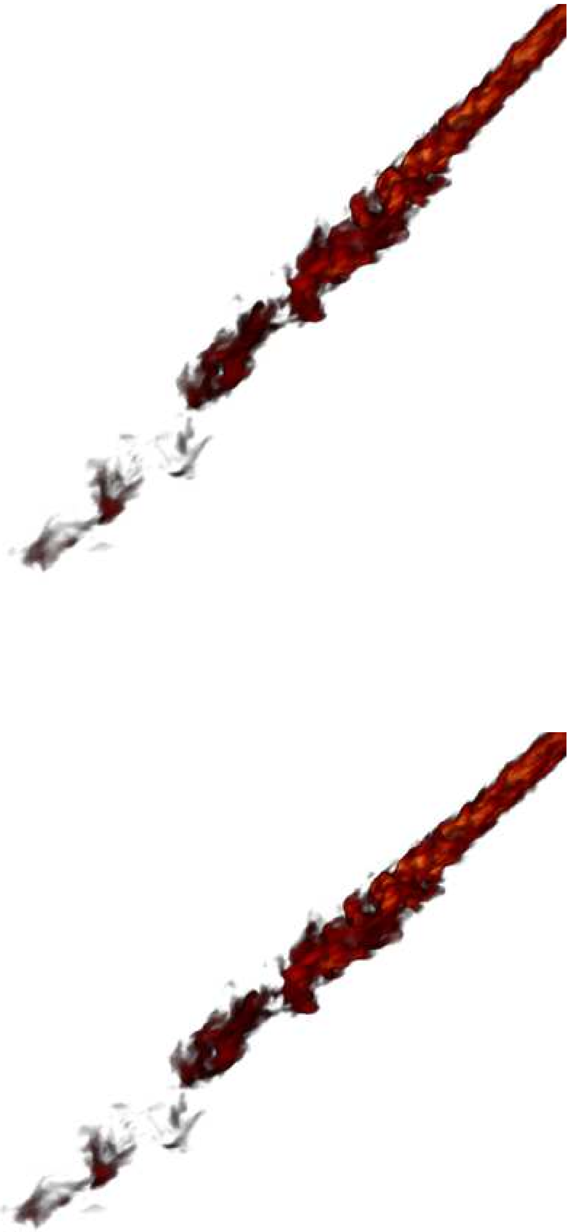

Figure C.3

Bibliography

Appl, S. & Camenzind, M. 1992, A& A, 256, 354

Baade, W. 1956, ApJ, 123, 550

Bacciotti, F., Chiuderi, C., & Oliva, E. 1995, A&A, 296, 185

Balbus, S. A. & Hawley, J. F. 1991, ApJ, 376, 214

Bally, J. & Devine, D. 1994, ApJ, 428, L65

Bally, J., Devine, D., & Reipurth, B. 1996, ApJ, 473, L49+

Baty, H. & Keppens, R. 2002, ApJ, 580, 800

Baty, H. & Keppens, R. 2006, A&A, 447, 9

Baty, H., Keppens, R., & Comte, P. 2003, Physics of Plasmas, 10, 4661

Beckwith, K., Hawley, J. F., & Krolik, J. H. 2008, ApJ, 678, 1180

Begelman, M. C. & Cioffi, D. F. 1989, ApJ, 345, L21

Bessolaz, N., Zanni, C., Ferreira, J., Keppens, R., & Bouvier, J. 2008, A&A, 478, 155

Birkinshaw, M. 1991a, The stability of jets (Beams and Jets in Astrophysics, P. A. Huges, Cambridge Astrophysics Series), 278–+

Birkinshaw, M. 1991b, The stability of jets (Beams and Jets in Astrophysics), 278–+

Biskamp, D. 1997, Nonlinear Magnetohydrodynamics (Nonlinear Magnetohydrodynamics, by Dieter Biskamp, pp. 392. ISBN 0521599180. Cambridge, UK: Cambridge University Press, August 1997.)

Blandford, R. D. & Payne, D. G. 1982, MNRAS, 199, 883

Bodo, G., Massaglia, S., Ferrari, A., & Trussoni, E. 1994, A&A, 283, 655

Bodo, G., Rosner, R., Ferrari, A., & Knobloch, E. 1989, ApJ, 341, 631

Bohm, K. H. 1983, Revista Mexicana de Astronomia y Astrofisica, vol. 7, 7, 55

Bolton, J. G., Stanley, G. J., & Slee, O. B. 1949, Nature, 164, 101

Braginskii, S. I. 1965, Transport processes in a plasma (Reviews of plasma physics, ed. M. A. Leontovich (Colsuntant Bureau, New York), Vol 1, pp. 205-311)

Cabrit, S. & Raga, A. 2000, A&A, 354, 667

Cabrit, S., Raga, A., & Gueth, F. 1997, in IAU Symposium, Vol. 182, Herbig-Haro Flows and the Birth of Stars, ed. B. Reipurth & C. Bertout, 163–180

Cantó, J., Raga, A. C., & Binette, L. 1989, Revista Mexicana de Astronomia y Astrofisica, 17, 65

Cerqueira, A. H. & de Gouveia Dal Pino, E. M. 2001, ApJ, 560, 779

Codella, C., Bachiller, R., & Reipurth, B. 1999, A&A, 343, 585

Curtis, H. D. 1918, PASP, 30, 65

Devine, D., Reipurth, B., Bally, J., & Balonek, T. J. 1999, AJ, 117, 2931

Dopita, M. A., Evans, I., & Schwartz, R. D. 1982, ApJ, 263, L73

Draine, B. T. 1980, ApJ, 241, 1021

Falle, S. A. E. G., Innes, D. E., & Wilson, M. J. 1987, MNRAS, 225, 741

Fanaroff, B. L. & Riley, J. M. 1974, MNRAS, 167, 31P

Felten, J. E. 1968, ApJ, 151, 861

Ferrari, A. 1998, ARA&A, 36, 539

Ferrari, A., Trussoni, E., & Zaninetti, L. 1981, MNRAS, 196, 1051

Ferreira, J., Dougados, C., & Cabrit, S. 2006, A&A, 453, 785

Frank, A., Jones, T. W., Ryu, D., & Gaalaas, J. B. 1996, ApJ, 460, 777

Freidberg, J. T. 1987, Ideal Magnetohydrodynamics (ISBN 0306425122. New York, USA: Plenum Press, 1987.)

Hardee, P. E. 2004, Ap&SS, 293, 117

Haro, G. 1952, ApJ, 115, 572

Haro, G. 1953, ApJ, 117, 73

Hartigan, P. 1989, ApJ, 339, 987

Hartigan, P., Morse, J. A., & Raymond, J. 1994, ApJ, 436, 125

Hartigan, P., Raymond, J., & Hartmann, L. 1987, ApJ, 316, 323

Hartmann, L. 2000, Accretion processes in star formation (Cambridge Astrophysics Series 32, Cambridge, UK)

Hayashi, C. 1966, ARA&A, 4, 171

Herbig, G. H. 1950, ApJ, 111, 11

Herbig, G. H. 1951, ApJ, 113, 697

Hussain, A. K. M. F. 1986, J. Fluid Mech., 173, 303

Jeong, H., Ryu, D., Jones, T. W., & Frank, A. 2000, ApJ, 529, 536

Jones, T. W., Gaalaas, J. B., Ryu, D., & Frank, A. 1997, ApJ, 482, 230

Keppens, R., Tóth, G., Westermann, R. H. J., & Goedbloed, J. P. 1999, Journal of Plasma Physics, 61, 1

Kerswell, R. R. 2002, Annu. Rev. Fluid Mech., 34, 83

Loken, C., Burns, J. O., Clarke, D. A., & Norman, M. L. 1992, ApJ, 392, 54

Massaglia, S., Bodo, G., & Ferrari, A. 1996, A&A, 307, 997

Matthews, T. A. & Sandage, A. 1962, PASP, 74, 406

Mignone, A., Bodo, G., Massaglia, S., et al. 2007, ApJS, 170, 228

Miura, A. 1984, J. Geophys. Res., 89, 801

Miura, A. & Pritchett, P. L. 1982, J. Geophys. Res., 87, 7431

Molinari, S., Ceccarelli, C., White, G., et al. 1999, ArXiv Astrophysics e-prints

Morse, J. A., Hartigan, P., Cecil, G., Raymond, J. C., & Heathcote, S. 1992, ApJ, 399, 231

Morse, J. A., Heathcote, S., Cecil, G., Hartigan, P., & Raymond, J. C. 1993, ApJ, 410, 764

Mouri, H. & Taniguchi, Y. 2000, ApJ, 534, L63

Mundt, R., Brugel, E. W., & Buehrke, T. 1987, ApJ, 319, 275

Mundt, R. & Fried, J. W. 1983, ApJ, 274, L83

Nijboer, R. J., van der Holst, B., Poedts, S., & Goedbloed, J. P. 1997, Computer Physics Communications, 106, 39

Norman, M. L., Winkler, K.-H. A., Smarr, L., & Smith, M. D. 1982, A&A, 113, 285

Ostriker, J. P. & McKee, C. F. 1988, Reviews of Modern Physics, 60, 1

Priest, E. & Forbes, T. 2000, Magnetic Reconnection (Magnetic Reconnection, by Eric Priest and Terry Forbes, pp. 612. ISBN 0521481791. Cambridge, UK: Cambridge University Press, June 2000.)

Raga, A. C., Binette, L., Canto, J., & Calvet, N. 1990, ApJ, 364, 601

Raga, A. C., Böhm, K.-H., & Cantó, J. 1996, Revista Mexicana de Astronomia y Astrofisica, 32, 161

Raga, A. C. & Noriega-Crespo, A. 1992, Revista Mexicana de Astronomia y Astrofisica, 24, 9

Reipurth, B. & Bally, J. 2001, ARA&A, 39, 403

Reipurth, B., Yu, K. C., Heathcote, S., Bally, J., & Rodríguez, L. F. 2000, AJ, 120, 1449

Romanova, M. M., Kulkarni, A. K., & Lovelace, R. V. E. 2008, ApJ, 673, L171

Ryu, D., Jones, T. W., & Frank, A. 2000, ApJ, 545, 475

Schulz, N. S. 2005, From dust to stars: Study of the formation and early evolution of stars (Springer)

Shu, F., Najita, J., Ostriker, E., et al. 1994, ApJ, 429, 781

Shu, F. H. 1977, ApJ, 214, 488

Shu, F. H., Lizano, S., Ruden, S. P., & Najita, J. 1988, ApJ, 328, L19

Solf, J. 1987, A&A, 184, 322

Viallet, M. & Baty, H. 2007, A&A, 473, 1

Thanks

First I want to thank my supervisors, Max Camenzind and Hubert Baty. Both helped me a lot and guided me for these three years. Thank you!

A big thanks to Imprs, and especially to Christain Fendt. We discussed, he helped me a lot, he was always supportive and positive!

Thanks a lot to the european community, and especially to the people who approved the Jetset training network, I visited so many nice places, and I could meet a lot of people!

Un grande grazie alla mia famiglia, a Mamma e a Papà. Non vi faccio leggere in inglese, non vi preoccupate! Mi avete sempre sostenuto, mi avete fatto sentire amato. Non posso davvero chiedere di piú! Vi voglio bene!

Back in english, for the people in Heidelberg! Three years and more ... a long time... And I'm happy to report that I met wonderful people here!

The girls: Giu, Vivi, Cla, Giovi, Isabel ... How many nights at Destille+Sonderbar+Cave?? And the movie nights? The dinners, the parties? Ah, we had a lot of fun! Warmer Erpel forever! You also surprised me, and made these years in Heidelberg unforgettaable. You also helped me and supported me so much when I made a move on my little Olga. I won't forget it! Thank you! :) Ah, do you remember the gothic night? and the "lesbian night by mistake" at villa nacht tanz? and the dinner + 10 episodes of sex and the city in a row? (ok maybe they were less... but maybe more??) and the schwarze pulver?? and the world cup? We are CAMPIONI DEL MONDO together! A big thanks also to Ale, even if you left long ago ... Shitboy vs. Culopode... the challenge continues!

The guys: well, not really defined as a group as the girls... Nevertheless there are some people here that helped me greatly for the thesis, for my work, for my soul. People from the office: Jamie, Steffen and Volker. Actually I think I couldnt be in better company! Volker, thanks for all the times you answered me about computers, and for the quotation (Johann Wolfgang von

Goethe in ”Götz von Berlichingen”, 1773)! Steffen, thanks for all the discussions, for translating my abstract in german, and for playing guitar! Thanks also for letting me play in the tree-house of your children! Jamie, thank you for all your corrections to my english (although I'm not exactly a fast lerner, am I?), thanks for teaching me snowboarding, thanks for the discussions on everything and your advices!

A special thanks to Steve. Not only you are the best representative ever, you also like Kenshiro! I think I dont need to add anything else :)

Thanks to Bagmeet: now I can make curry paste from curry powder! (it takes ages without a mixer, but still...) Thanks also because you're always positive and smiling.

I want also to thank the people who managed to put a positive indelible mark on my life here. Vivi', Andrew, Pak Hin, Massimo, Giovanni, Brian, Marik, Dusan, Steffy.

A big thanks to my friends in Italy, in particular to Fabio and Maddy, for their support from the mother land. Forever friends!

In the end, if you're reading this lines you deserve my thanks as well!

Last, but not least, Olga. Thank you! You made me grow up, you motivate me, you care about me, you always told me the right words to go on even when I had almost no hope left when writing ... and you know, you changed my life forever. I'm so happy for that!

As you may imagine, I cannot really report the quotation from Goethe here ... :)

I dint destroy any computer in these three years, but I really harmed them with buggy code all the time!

This thesis was written in about one month. In the last 2 weeks I reduced sleep. In the last 2 days I gave it up completely. I stopped writing when I was making so many mistakes that the spell checker couldnt understand what the %$#! I was typing. (note that %$#! is not really a bad word. It does not begin with f for instance. It is a synonim of Inferno, but apparently it may offend some people ... :P)

I suddenly fell asleep once, and woke up half an hour later with my leg completely dead... I managed anyway to go and check if I had the marks of the keyboard on my forehead...

I officially hate latex. If somebody can find the mistake in chapter 4, that didnt allow me to use the automatic references for the figures, he/she gets 10 euros! (to be payed in beers or alcoholics of course)

During this thesis I destroyed the world twice. Well, actually I could have had. One night I couldnt go on and found a flash animation on internet, of a red button asking me not to press it. “dont press me!” I did. “Hey! really! dont press me” I did it again. “you did it again! Dont do it!” etc etc... At a certain point if I had pressed the button the world would have been destroyed. Well, I knew it couldnt possibly have been the case... but what if it WAS true? I’m sure out there there is a very dangerous red button... so be careful!

Ok, I guess this is really the end, and in any case, I have to do some corrections before printing, at the very last minute, as usual! Thanks everybody! I owe you one! (or more, probably!)